LONG-TERM RESPONSE OF SOILS SUBJECTED TO REPETITIVE GEOENVIRONMENTAL LOADS

A Thesis
Presented to
The Academic Faculty

by

Yuanjie Shen

In Partial Fulfillment
of the Requirements for the Degree
Doctor of Philosophy in the
School of Civil and Environmental Engineering

Georgia Institute of Technology
December 2018

LONG-TERM RESPONSE OF SOILS SUBJECTED TO REPETITIVE GEOENVIRONMENTAL LOADS

Approved by:

Dr. J. Carlos Santamarina, Advisor
School of Civil and Environmental Engineering (Adjunct Professor)
Georgia Institute of Technology

Dr. J. David Frost
School of Civil and Environmental Engineering
Georgia Institute of Technology

Dr. Susan E. Burns
School of Civil and Environmental Engineering
Georgia Institute of Technology

Dr. Sheng Dai
School of Civil and Environmental Engineering
Georgia Institute of Technology

Dr. Guillermo Goldsztein
School of Mathematics
Georgia Institute of Technology

Date Approved: September 17th, 2018

Hard work betrays none, but dreams betray many.

ACKNOWLEDGEMENTS

Firstly, I would like to express my sincere gratitude to my advisor, Professor J. Carlos Santamarina for the continuous support of my research. His immense knowledge, dedication, and motivation always inspire and guides me throughout my Ph.D. study. He is not only a great advisor but also a great mentor for my life.

Besides my advisor, I would like to thank the rest of my thesis committee; Dr. J. David Frost, Dr. Susan E. Burns, Dr. Sheng Dai, and Dr. Guillermo H. Goldsztein, for their insightful comments and encouragements, but also for the valuable questions which incent me to widen my research with new perspectives.

My sincere thanks also go to the members of the Particulate Media Research Laboratory PMRL and Energy Geo-Engineering Laboratory EGEL for the stimulating discussions and fun. Special thanks to Dr. Budi Zhao and Dr. Xunchang Fei, for the opportunity to work together and their contribution to advance my research.

Finally, I would like to thank my family for always being with me, supporting my personal life and my study spiritually with endless love.

TABLE OF CONTENTS

LIST OF TABLES

LIST OF FIGURES

SUMMARY

Repetitive loading cycles originate from a variety of natural and industrial processes, affect soil properties and the long-term performance of geotechnical systems. This thesis provides unprecedented experimental data and physical analyses of repetitive environmental loading cycles on geomaterials. Research tools adopted in this study include long-term experiments in multi-physics cells, microfluidics, seismic and NMR monitoring, and analytical solutions. The void ratio evolves towards the terminal void ratio as the number of wet-dry cycles increases. Shear wave velocity data indicate that the soil fabric becomes less sensitive to stress changes after repetitive wet-dry cycles. Changes in the soil-water characteristic curve demonstrate that fine-grained soil fabric evolves towards a new stable fabric as the number of wet-dry cycles increases. Precipitation within dual-porosity microfluidic chips provides new insight into salt crystallization phenomena in geomaterials, such as fractured rocks. Pore network topology and surface wetting characteristics govern crystal growth patterns. Pore fluid chemistry cycles in fine-grained soils alter particle level electrical forces and particle-particle associations. The soil fabric evolves with cycles of pore fluid chemistry and leads to chemical-mechanical coupled response. Atmospheric pressure cycles accelerate water transport in unsaturated soils and promote moisture homogenization. The amount of water loss due to pressure cycles is inversely proportional to the number of cycles, and efficiency is frequency dependent. This study highlights the behavior of sands and fines subjected to repetitive geoenvironmental loads under various boundary conditions. The physics-inspired and data-driven approaches applied in this research can be used to enhance the existing design guidelines of geo-structures for long-term performance, serviceability, and safety.

CHAPTER 1. INTRODUCTION

1.1 Motivation

Long-term repetitive loading cycles originate from a variety of natural and mechanical phenomena and include mechanical cycles (Long and Vanneste 1994; Peng et al. 2006; Andersen 2009; Wichtmann et al. 2010), chemical cyclic changes in pore fluid (Musso et al. 2003), thermal cycles (Pasten and Santamarina 2014; Di Donna and Laloui 2015), drying and wetting sequences (Albrecht and Benson 2001), freeze-thaw cycles (Chamberlain et al. 1990; Viklander 1998; Qi et al. 2008), and repetitive changes in pore water pressure (Orense et al. 2004; Nakata et al. 2013; Huang 2016).

The long-term performance of geotechnical systems depends on the soil response to this wide variety of repetitive loads. These loading cycles are highly coupled and play an important role in both the micro and macro response of soils. Numerous reports and evaluations have assessed engineering failures under cyclic conditions. These failures have resulted in severe human life and economic loss. This thesis focuses on the long-term response of geomaterials under repetitive environmental loadings. It provides unprecedented data and in-depth analyses of suction cycles, mineral precipitation induced by wet-dry cycles, pore fluid chemistry cycles, and atmospheric pressure cycles.

1.2 Thesis Organization

The Thesis is organized into four central chapters that describe the design and construction of new experimental tools used to evaluate repetitive environmental loadings on geomaterials and to enhance engineering design parameters.

Chapter 2 explores the quasi-static mechanical responses of fine-grained soil subjected to repetitive suction changes under zero lateral strain boundary conditions. Suction cycles lead to irreversible volumetric strains which often result in plastic deformation and desiccation cracks. It also causes changes in the matric suction, void ratios, stiffness, and electromagnetic properties. Data gathered in the experimental program suggests cyclic trends in soil water characteristics and volumetric strain accumulations. The analysis of void ratio evolution and terminal density determines model parameters. Fitting functions can predict soil behavior trends subjected to repetitive loading cycles.

Chapter 3 investigates mineral precipitation induced by wet-dry cycles in both droplet-scale and pore-scale experiments. The interactions between particle and pore fluid exchanges and wet-dry induced precipitation alter the hydraulic conductivity, void ratio, and other engineering properties. Microscopic images record the initiation and development of salt precipitation on substrates with different surface characteristics. The discussion focused on contact angle measurements further support precipitation conditions observed both in droplets and in microfluidic chips.

Chapter 4 addresses the phenomena of fine-grained soils subjected to repetitive pore fluid chemistry changes under zero lateral strain boundary conditions. Data analyses examine the cyclic behavior of fine-grained soils due to particle-fluid interactions. Hydraulic conductivity predications and electrical conductivity data advance the understanding of fabric changes in fine-grained soils.

Chapter 5 explores the geoidal drying process of unsaturated coarse-grained soils under natural atmospheric pressure changes. Atmospheric pressure cycles induce pressure

oscillations from seasonal changes on near-surface geomaterials which not only promote gas phase interactions but also shorten the time to reach the equilibrium state. Time-lapse saturation profiles illustrate measurements of accelerated water transport in sand specimens due to fluid pressure oscillations. Analyses and discussions evaluate the experimental results in comparison to a robust mathematical model.

Chapter 6 summarizes salient conclusions from previous chapters. Future work recommendations provide suggestions to further on understanding of cyclic soil behavior subjected to repetitive geo-environmental loads.

CHAPTER 2. WET-DRY CYCLES – k_0 CONDITION

2.1 Introduction

Soils experience periodic wet-dry cycles due to natural environmental fluctuations during rainy and arid periods. Similarly, clay liners that serve as buffer materials in solid waste landfills and toxic waste sites also undergo wet-dry oscillations. Wet-dry cycles lead to volumetric expansion and contraction of soils and changes in soil properties which cause substantial damage in geosystems (Allam and Sridharan 1981). Engineering failures include foundation movements, desiccation cracks, and structural fatigue.

Unsaturated soil slopes subjected to cyclic climate changes experience hysteresis in both the soil-water characteristic curve and in soil hydraulic conductivity (Topp and Miller 1966; Mualem 1976; Hillel 1998; Lin and Benson 2000; Alonso et al. 2005). Landslides may result from this hysteresis, aggregated by heavy rains (Lumb 1962; Brand 1984; Fukuoka 1980; Wolle and Hachich 1989; Fourie 1996; Lim et al. 1996; Ng and Shi 1998). Rainwater infiltration rises the groundwater table and increases the pore water pressure, the soil shear strength decreases, and failure occurs.

This study explores fine-grained soil behavior under long-term cyclic suction changes. A comprehensive review of hydro-mechanical coupling cycles in unsaturated soils is followed by experimental studies with suction controlled under zero lateral strains in oedometer cells. The discussion and analyses address inter-particle and intra-particle interactions, hysteresis in soil water retention characteristics, plastic strain accumulation, and terminal densities.

2.2 Soil Response to Repetitive Moisture Loadings: Terms and Processes

The analysis and discussion of the long-term response of soils subjected to repetitive moisture loadings requires terms and concepts that are not part of the standard geotechnical vocabulary. The following sections present these concepts.

2.2.1 Soil-Water Characteristic Curve

The soil-water characteristic curve SWCC relates suction to capillary pressure (Rahardjo and Leong 1997; Barbour 1998). The SWCC and saturated soil properties are used to predict the engineering properties of an unsaturated soil (Brooks and Corey 1966; van Genuchten 1980; Fredlund et al. 1994; Vanapalli et al. 1999; Fredlund 1998; Barbour 1998). The soil-water characteristic curve of a natural specimen has a slightly lower air-entry value (AEV) and a higher rate of desorption (Ng and Pang 2000). Hysteresis in SWCC relates to the morphology and pore size distribution of the porous medium and to pore interconnections. There is a distinct difference in both desorption (drying) and adsorption (wetting) characteristics during wet-dry cycles: the rates of desorption and adsorption are substantially higher in earlier cycles because of changes in the soil structure.

2.2.2 Image Analysis – Fabric Change

Image analysis can be used to examine the evolving microstructure of the fine-grained soils under wet-dry cycles. Key features observed in the first wetting cycle include the formation of stretched pores and the deformation in micro-aggregates. These changes lead to permanent pore structure changes.

Macroscopic consolidation directly relates to SEM observations and changes in pore size distribution determined with the use of the mercury intrusion technique. The progressive collapse of the larger pores in saturated soils subjected to increased compressive stress indicates a rise in the air entry value AEV (Delage & Lefebvre 1984; Griffiths & Josi 1989; Lapierre et al. 1990). Mercury intrusion experiments also explain the smaller AEV in soils compacted wet-of-optimum.

2.2.3 Suction-Controlled Techniques

(1) Axis-Translation. The axis translation technique is the most common technique for suction control. This method has a number of limitations: (i) it is not representative of field conditions where the air pressure is under atmospheric conditions; (ii) the air pressurization process that affects the water pressure is questionable; and (iii) there is absence of a continuous gaseous phase in nearly saturated specimens (Escario & Saez 1986; Escario 1980; Lloret and Alonso 1980).

(2) Osmotic Technique. The main advantage of the osmotic technique is the high suction range that can be reached. By contrast to the axis translation technique, it applies direct water potential to the liquid water; therefore it is particularly well suited to high water content samples. The main disadvantage is the weakness of the membrane and its sensitivity to microbial attack. Prevention of bacterial growth requires the addition of penicillin drops to the solution before use (Kassiff and Ben Shalom 1971; Delage et al. 1992; Cui and Delage 1995).

(3) Vapor Equilibrium. The vapor equilibrium technique controls the relative humidity of the atmosphere that surrounds the soil specimens (using saturated salts or

sulfuric acid at various concentrations; see Oteo-Mazo et al. 1995). This technique controls the total suction and water transfer in the vapor phase. The time required to reach equilibrium is long due to low vapor exchange rates between the saline solution and the specimen. This technique enables experimental studies in engineering applications which require large suctions such as nuclear waste storage (Al Mukhtar et al. 1993; Bernier et al. 1997).

2.2.4 Wet-Dry Cycles

Successive wet-dry cycles induce irreversible strain accumulation and significant changes in the soil fabrics of unsaturated fine-grained soils (Osipov et al. 1987; Dif and Bluemel 1991; Day 1994; Al-Homoud et al. 1995; Basma et al. 1996; Alonso et al. 1995; Sharma 1997). The soil response during virgin loading at constant suction conditions depends on the suction history (Sharma 1997). In addition, the interfacial slippage between soil particles produces an irreversible mechanical response (Gallipoli et al. 2003). The stabilization effect of the normal force exerted at inter-particle contacts by the water meniscus partially reduces the potential of this slippage in unsaturated soils (Wheeler and Karube 1996).

2.2.5 Volumetric Strain: Terminal State

A soil subjected to repetitive loading will reach a stable asymptotic terminal state (D'Appolonia and D'appolonia 1967; Narsilio and Santamarina 2008). The convergence rate towards the terminal state depends on the initial dry density and water content, soil structure, history of dry-wet cycles, and the stress state. Volumetric strains converge towards an equilibrium elastic stage at the end of the suction cycles (Nowamooz and

Masrouri 2008). Experimental results show that the first cycle causes the highest reduction in swelling rebound; as the number of cycles increases, volumetric contraction continues until the equilibrium state (Chen 1965; Chu and Mou 1973; Chen and Ma 1987; Subba Rao and Satydas 1987, Dif and Bluemel 1991; Al-Homoud et al. 1995).

2.2.6 Shakedown or Ratcheting?

There are two distinct asymptotic trends shear strain under repetitive cycles (Sharp and Booker 1984; Collins et al. 1993; Alonso-Marroquın and Herrmann 2004; Werkmeister et al. 2005). Shakedown refers to the finite shear strain accumulation. On the other hand, ratcheting refers to continued plastic strain accumulation in every cycle.

2.3 Experimental Study: Devices and Test Procedure

This experimental program explores the evolution of the void ratio and the small strain stiffness of Georgia Kaolinite SA-1 subjected to repetitive moisture cycles under zero-lateral strain conditions. The repetitive suction loading system consists of an instrumented floating-ring oedometer cell under constant mechanical load within an automatic environmental-controlled chamber (Figure 2.1). The short floating ring oedometer (*ID* = 80mm, 5mm wall thickness, and 24mm high) reduces the equilibrium time during repetitive suction loading. The loading system consists of a rigid reaction frame, pneumatic cylinders, and peripheral control electronics. The experimental study involves 4 specimens during the 150 day long tests.

2.3.1 Environmental-Controlled Repetitive Loading System

We perform long-term wet-dry cycle experiments inside the environmental chamber (Cincinnati Sub-Zero ZP-32-3.5-SCT/AC). This chamber provides a controlled environment for dry-wet cycles with a constant temperature T = 22°C and alternates between two relative humidity boundaries for wet-dry cycles (RH = 40% for dry cycles and RH = 100% for wet cycles). Wires for sensors extend towards the outside of the chamber where peripheral electronics are located.

2.3.2 Deformation Monitoring

The LVDT (TransTek DC 0243) mounted on the rigid reaction frame connects with the piston of the pneumatic cylinders and tracks the vertical deformation of the specimen. The data logger (Keysight 34970A, Figure 2.1) saves the LVDT measurements.

2.3.3 Shear Waves: Bender Elements

The oedometer ring includes bender elements mounted inside removable nylon screws. We use grounded parallel-type bender elements for both source and receiver to minimize crosstalk (Lee and Santamarina 2005). The bender elements are 12.7mm × 8mm × 0.7mm in size and are mounted with a 5mm cantilevered length (7.7mm anchored length). The function generator sends a 10V step signal every 50ms (Keysight 33210A). Received signals pass through a filter-amplifier (Krohn-Hite 3364 – 500 Hz high-pass and 200 kHz low-pass window) before being averaged in the oscilloscope and stored (Keysight DSOX 2014A – 1024 stacked signals. See implications of signal stacking in Santamarina and Fratta 2005).

2.3.4 Electrical Conductivity: Electrodes

We measure eletrical conductivity using single wire copper cables as electrodes. The oedometer ring includes electrodes glued on the same mid-plane perpendicular to the bender elements. The HV and LV electrodes connect with a known resistor in series to measure current. The function generator sends a 1V, 10 kHz signal (Keysight 33210A). A data logger records the voltage drop across the specimen which is proportional to the resistance in the geomaterial. Electrical resistivity is a function of the measured resistance R; electrical conductivity σ is the inversion of its resistivity ρ.

Electrical Resistivity $$\rho = \beta R\left[\Omega \cdot m\right] \tag{2.1}$$

Electrical Conductivity $$\sigma = \frac{1}{\rho}\ \left[S/m\right] \tag{2.2}$$

where β is a shape factor coeffeicient, β = 0.0044.

2.3.5 Specimen Preparation

This experimental study uses Georgia Kaolinite SA-1 (median grain size D_{50} = 1.1μm; liquid limit LL = 49%; specific gravity G_s = 2.6; specific surface S_a = 13.0m^2/g). Table 2.1 summarizes the physical and engineering properties of the Georgia Kaolinite SA-1.

2.3.6 Test Procedure

The test starts with the specimen saturated and at the liquid limit. The loading procedure for all specimens consists of three stages: (1) static step loading to σ_0, (2)

repetitive wet-dry cycles, N = 50 cycles, and (3) unloading. Wet-dry cycles go from saturation (suction ψ = 0kPa) to relative humidity RH = 40% (suction ψ = 500kPa). Electrical conductivity is continuously recorded through the repetitive loading cycles. Shear wave measurements during the repetitive loading stage take place at the end of wet and dry cycles. Each wet-dry cycle lasts about 5000 minutes (4-to-5 days). Figure 2.2 summarizes all test conditions. The total four specimens are divided into two pairs. In each pair of study, two specimens are subjected to same loading stress. One specimen experiences wet-dry cycles (N = 30), and the other specimen continues (N = 50). Both the specimens illustrate good repeatability from the first 30 cycles of experimental results.

2.4 Experimental Results

This section presents detailed experimental results for kaolinite specimens subjected to suction cycles under (1) low confining stress (σ_0 = 50kPa), and (2) high confining stress (σ_0 = 100kPa). Then, the following section contains a complete analysis of the full dataset.

2.4.1 Effective Stress σ'_v vs. Void Ratio e

Figure 2.3 shows the evolution of the void ratio during the static-repetitive loading history followed by the static unloading stage. The void ratio for the saturated kaolinite specimen decreases monotonically during the initial static loading stage. Repetitive wet-dry cycles cause identical expansion and contraction due to the wet-dry cycles in both experiments. We use Bishop's effective stress equation to estimate the equivalent effective stress in soils subjected to suction changes (Bishop 1959).

$$\sigma_{eff} = (\sigma - u_a) + \chi(u_a - u_w) \tag{2.3}$$

A first-order estimate of the effective stress parameter χ is $\chi = S_w$. Despite the differences in the confining stress during the static loading stage, the suction induced stress ($u_a - u_w \approx 500$kPa) governs compaction and the influence of the initial effective stress greatly reduces.

2.4.2 Void ratio vs. Number of Cycles, N

Figures 2.4a and 2.4b illustrate the void ratio evolution with the number of cycles for the two test conditions (N = 30 cycles; σ_0 = 50kPa and N = 30 cycles; σ_0 = 100kPa). Most changes in the void ratio take place in earlier cycles and are more significant in the specimen subjected to lower stress conditions.

2.4.3 Electrical Conductivity

Figure 2.5 presents the evolution of electrical conductivity during repetitive wet-dry loading. The electrical conductivity is a function of the water content, void ratio, and soil fabrics. Soil response of kaolinite during initial wet-dry cycles lead to significant variations. Clay has an electrical conductivity range between 10 ms/m to 1000 ms/m (Grisso et al. 2009). Degree of saturation in pores determines the difference in electrical conductivity response between the end of wet cycles and dry cycles. There is a consistent change in the electrical conductivity response between the wet and dry stages and throughout the cycles. Trends stabilize as the soil evolves towards a constant fabric condition during wet-dry cycles.

2.4.4 Shear Wave Signals

Figure 2.6 shows the evolution of shear wave signals recorded during the initial loading and at the end of wetting cycles. While signals are complex, coda analysis shows that travel time decreases during the quasi-static loading stage and the first drying cycle. Therefore, changes in the first arrival times during repetitive wet-dry cycles are less pronounced. The time-stretched cross-correlation method in CODA wave analysis assesses these minor changes in travel time (Sneider 2006; Dai et al. 2013). Then, the stretching factor θ allows the calculation of minute changes in the shear wave velocity during repetitive loading cycles.

2.5 Analyses and Discussion – Complete Dataset

This section contains an analysis of the complete dataset produced with the experiments in this study.

2.5.1 Evolution of Void Ratio vs. Number of Cycles, N

Figure 2.7 presents the trends in void ratio changes between two consecutive wet-dry cycles during the repetitive loading stage:

$$\Delta e_i = \left(e_i^{dry} - e_i^{wet}\right) - \left(e_{i+1}^{dry} - e_{i+1}^{wet}\right) \tag{2.4}$$

The trend shows the rate of convergence towards an elastic soil behavior response during repetitive wet-dry loading. Results show that the void ratio difference is highest during the first wet-dry cycle. The difference trend converges exponentially to zero primarily within the first 10 cycles. A modified hyperbolic model is fitted to the void ratio versus number

of cycles data shown in Figure 2.4 (inspired by Paute et al. 1993; Werkmeister et al. 2005; modified from Chong and Santamarina 2016):

$$e_i = e_T + (e_1 - e_T)\left[1 + \left(\frac{i-1}{N^*}\right)^m\right]^{-1} \quad \text{for i} \geq 1 \text{ and m} > 0 \tag{2.5}$$

where m is a fitting parameter, and i is the number of loading cycles. Measurements of the void ratio e_i occur after the i^{th} cycle. The initial void ratio e_1 corresponds with i = 1, and the terminal void ratio e_T is the asymptotic void ratio as $i \rightarrow \infty$. Results show adequate predictability. Most importantly, trends allow us to estimate the terminal void ratio at $N = \infty$ based on the data for the first N = 30 cycles.

Earlier repetitive loading cycles indicate both the recoverable and irrecoverable volumetric strains. The plastic strain accumulation becomes negligible as the number of cycles increases and the hysteresis vanishes, i.e., an elastic shakedown. The model parameter N^* is the number of cycles required for a given soil to compact to half of the asymptotic contraction, that is, $(e_1 - e_T) / 2$. Figure 2.8 presents the fitting error for both wetting and drying curves in the two experiments as a function of characteristic number of cycles, N^*. The least fitting error occurs for N^* = 7-to-9.

2.5.2 Void Ratio and Electrical Conductivity Comparisons

Figure 2.10 compares the void ratio evolution for the low and high confining stress specimens (σ_0 = 50kPa and σ_0 = 100kPa) tests during the repetitive loading stage. The two specimens evolve very similar. However, they retain memory of the initial mechanically

applied effective stress and trends do not converge even though the cyclic suction induced stress $u_a - u_w \approx 500$kPa is significantly higher than the applied load.

Figure 2.11 presents the electrical conductivity evolution versus a void ratio for two tests (σ_0 = 50kPa and σ_0 = 100kPa). Kaolinite specimens behave identically in the subsequent repetitive loading stages with the exception of the initial static loading stage due to different confining stresses. These data confirm a well suction-controlled experimental environment.

2.5.3 Shear Wave Velocity

The shear wave velocity is a power function of the vertical σ'_z and horizontal σ'_x effective stresses (Roesler 1979; Yu and Richard 1984; Santamarina et al. 2001):

$$V_s = \alpha \left(\frac{\sigma_z^{'} + \sigma_x^{'}}{2\,kPa} \right)^{\beta} = \alpha \left(\frac{\sigma_z^{'}}{1kPa} \right)^{\beta} \left(\frac{1+K_0}{2} \right)^{\beta} \tag{2.6}$$

where the where the α-factor is the shear wave velocity at effective stress σ'_{mean} = 1kPa, and the β-exponent represents the stress sensitivity of the shear wave velocity. The shear wave velocity-stress relation captures both the contact behavior and fabric changes (Cha et al. 2014).

Figure 2.12 summarizes the evolution of the shear wave velocity during the static and cyclic loading (at the end of wetting cycles) for the specimens subjected to low and high confining stress (σ_0 = 50kPa and σ_0 = 100kPa). Figure 2.13 presents the α-factors and β-exponent computed by fitting Equation 2.6 to the static load stages before and after

repetitive loading for all tests. The data trend is consistent with the α and β relationship reported in the literature (Cha et al. 2014). Overall, the kaolinite becomes stiffer (lower C_c) and as the α-factor increases, the β-exponent decreases, and the soil fabric becomes less sensitive to stress changes after repetitive dry-wet loading.

The shear wave velocity at the end of wetting increases as the number of repetitive dry-wet cycles progresses (Figure 2.12). Shear wave velocity increments during repetitive loading stages are relatively minor, and comparable for the two tests. The rate of increase in small-strain stiffness during repetitive loading is more pronounced in kaolinite during the earlier than later cycles. As data refers to the end-of-wetting, the minor changes in stiffness highlights the governing effect of effective stress rather than fabric on shear wave velocity.

2.5.4 Cyclic Soil-Water Characteristic Curve

Figure 2.14 presents the evolution of the soil water characteristic curve SWCC with an increasing number of cycles (N = 1, 5, 10, and 30). We use a dew point hydrometer device to determine the SWCC for all kaolinite specimens (WP4C PotentiaMeter; Campbell et al., 2007). Gravimetric moisture and suction data are gathered during drying process. Water potential readings start in wet specimens at a water content slightly lower than the liquid limit. For wet samples with suction values < 0.1MPa, the short drying time allows us to obtain several measurements on the desorption curve. Thereafter, samples are air dried for ~ 1h and equilibrated for > 24h before every reading. A point near the AEV is obtained for all tests. Results in Figure 2.14 show that the rates of desorption and adsorption are substantially higher during the first drying than after subsequent wet-dry cycles. The

hysteresis gap between the adsorption and desorption curve gradually closes out with an increase in the number of cycles (N = 1, 5, 10, and 30). Eventually, adsorption and desorption curves overlap with sufficient numbers of wet-dry cycles (N = 50).

2.6 Conclusions

The void ratio, electrical conductivity, and the small strain stiffness of fine grained sediments evolve during repetitive wet-dry cycles under zero-lateral strain conditions lead to the following notable conclusions.

- The void ratio evolves towards the terminal void ratio e_T as the number of wet-dry cycles $i \rightarrow \infty$. The terminal void ratio e_T is a function of the initial void ratio e_0. In other words, the soil retains memory of its initial fabric.

- The characteristic number of cycles N^* required to reach half of the asymptotic volume contraction $\Delta e = (e_1 - e_T) / 2$ is small compared with the number of cycles required to reach terminal state.

- The evolution in electrical conductivity captures the hysteresis in soil water characteristics and converging fabric evolution.

- The shear wave velocity-stress $V_s = \alpha \, (\sigma'_{mean}/\text{kPa})^{\beta}$ captures both contact behavior and fabric changes. Data show that kaolinite becomes stiffer (lower C_c), the α-factor increases, the β-exponent decreases and the soil fabric becomes less sensitive to stress changes after repetitive wet-dry cycles.

- The increase in shear wave velocity suggest a gradual increase in horizontal stress during repetitive loading under zero lateral strains. However, shear wave remains effective stress controlled at the end of wetting period.

- Changes in the soil-water characteristic curve indicate the kaolinite fabric evolves towards a new stable fabric as the number of cycle increases.

Table 2.1. Kaolinite SA-1 soil properties.

Kaolinite Properties SA – 1	
Specific Gravity	2.6
GE Brightness, % Average	79.5
pH (28% solids), Average	5.4
Median particle diameter [µm]	1.2
oil absorption, [g/100g] clay	32
minimum dispersed viscosity, 62% solids	400 cps
raw color	cream
specific surface, S_a [m^2/g]	13
d_{50} [µm]	1.1
thickness, nm	70
liquid limit, %	49

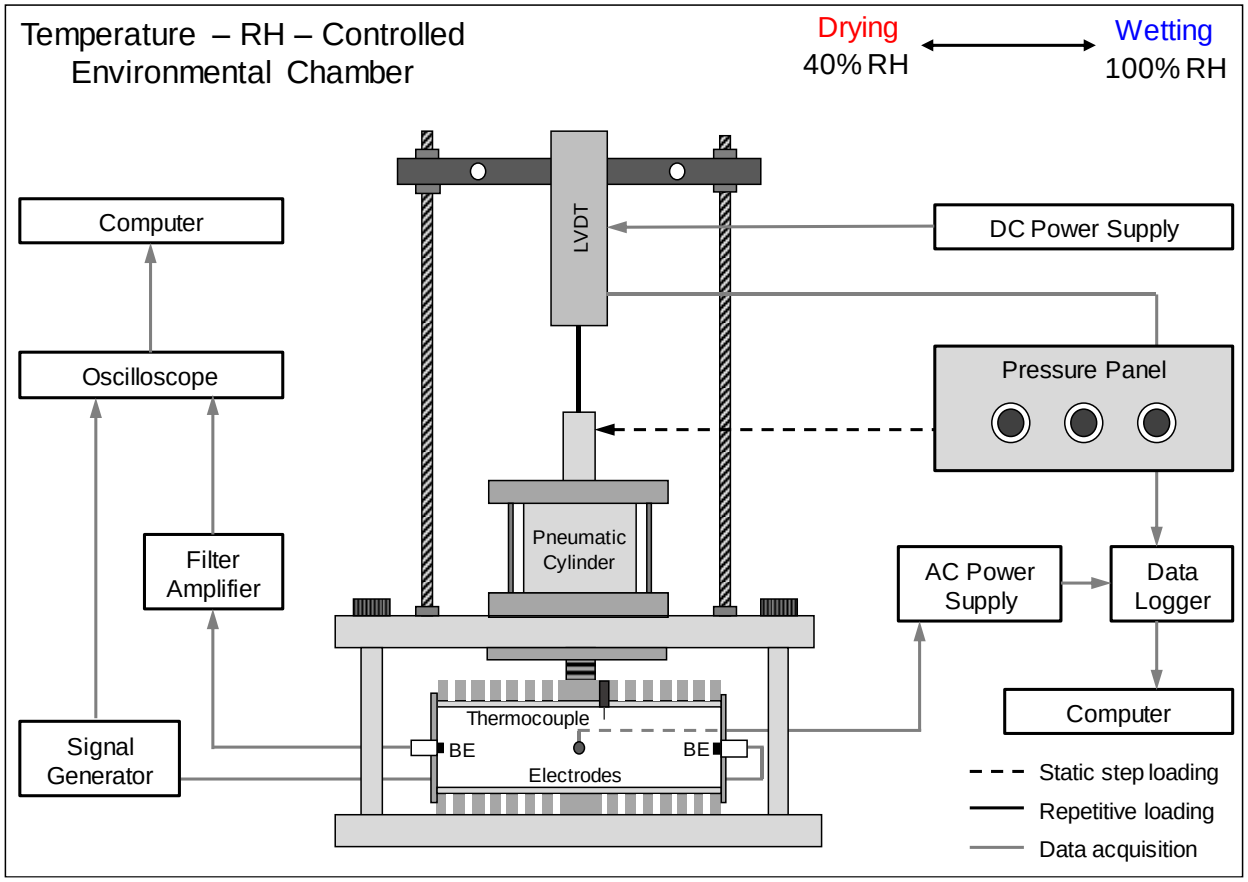

Figure 2.1. Device. Schematic diagram of the pneumatic system used for static and repetitive loading. The loadings system conducts the experiment inside an environmental chamber which maintains at a constant temperature and alternate the relative humidity *RH* between 40% and 100%. The peripheral electronics are used to measure deformation, electrical conductivity, and shear waves. The oedometer cell consists of a floating ring with bender elements and electrodes and top and bottom caps with a thermocouple. Top and bottom cap dimensions: 80mm diameter and 10mm height. Floating ring dimensions: *ID* = 80.5mm, *OD* = 90.5mm, and 30mm height.

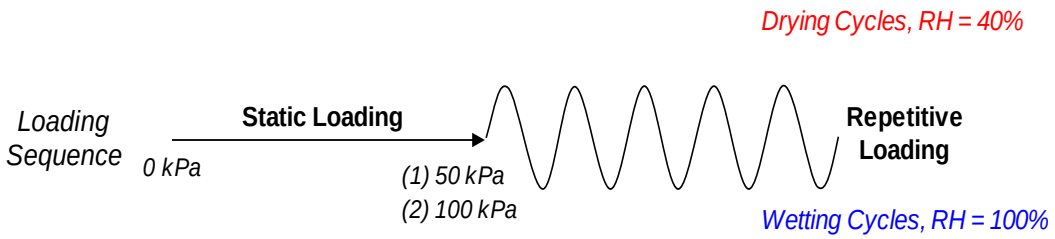

Figure 2.2. Static-Repetitive loading test conditions.

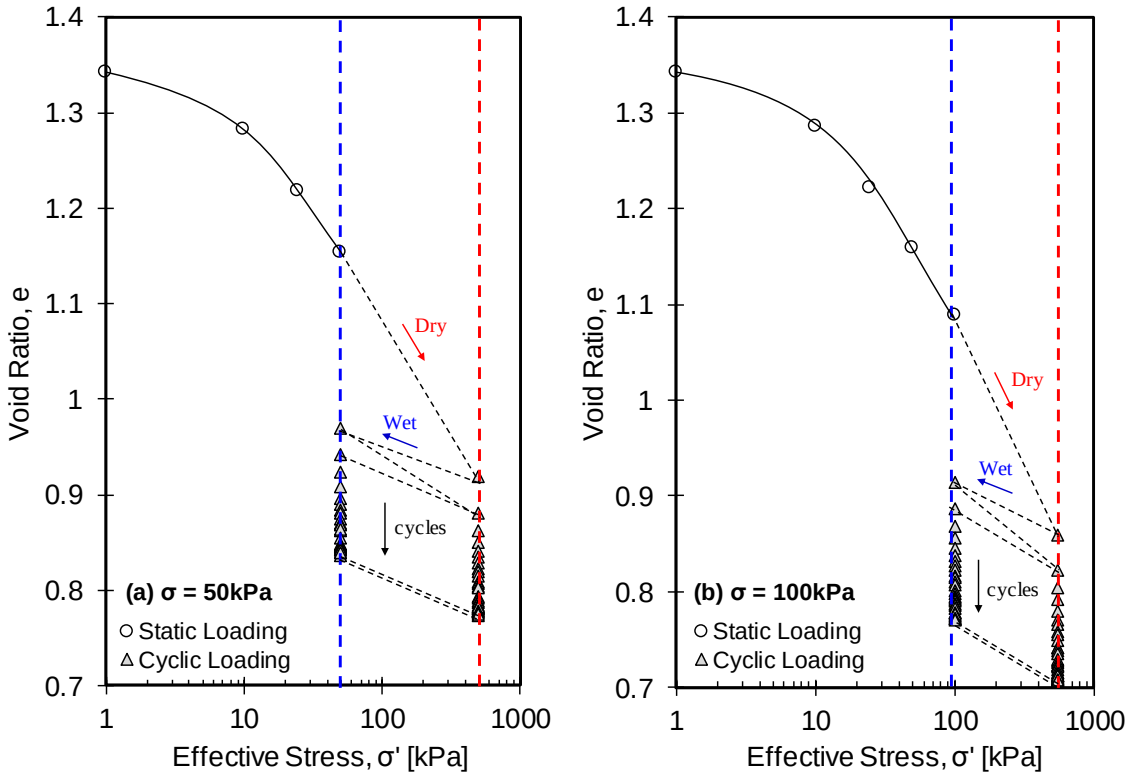

Figure 2.3. The change in void ratio during the static-repetitive loading history. Test conditions: (a) σ_0 = 50kPa (b) σ_0 = 100kPa. Equivalent effective stress condition at dry cycles adapt the Bishop's effective stress equation.

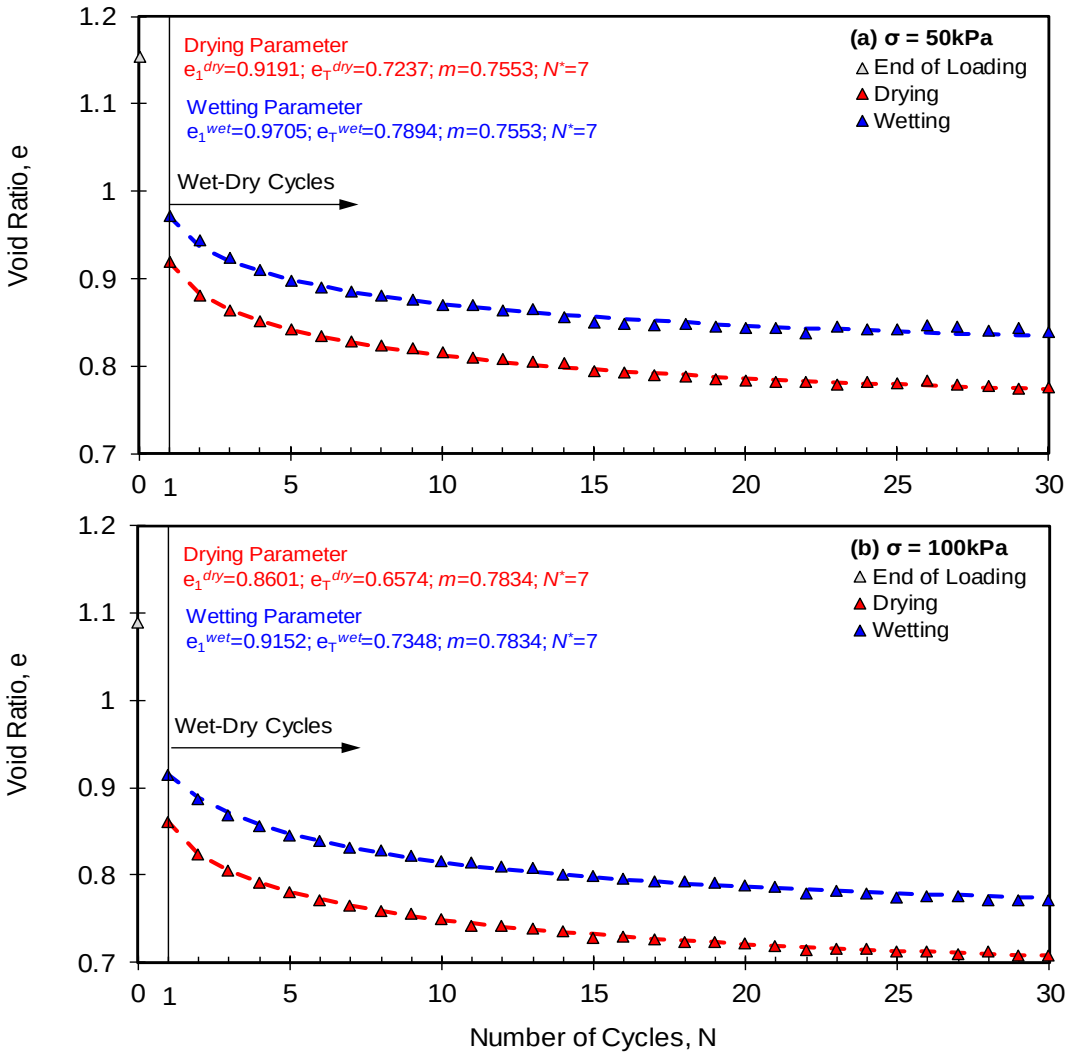

Figure 2.4. Void ratio evolution with number of cycles during repetitive loading history. Test conditions: (a) σ_0 = 50kPa. (b) σ_0 = 100kPa.

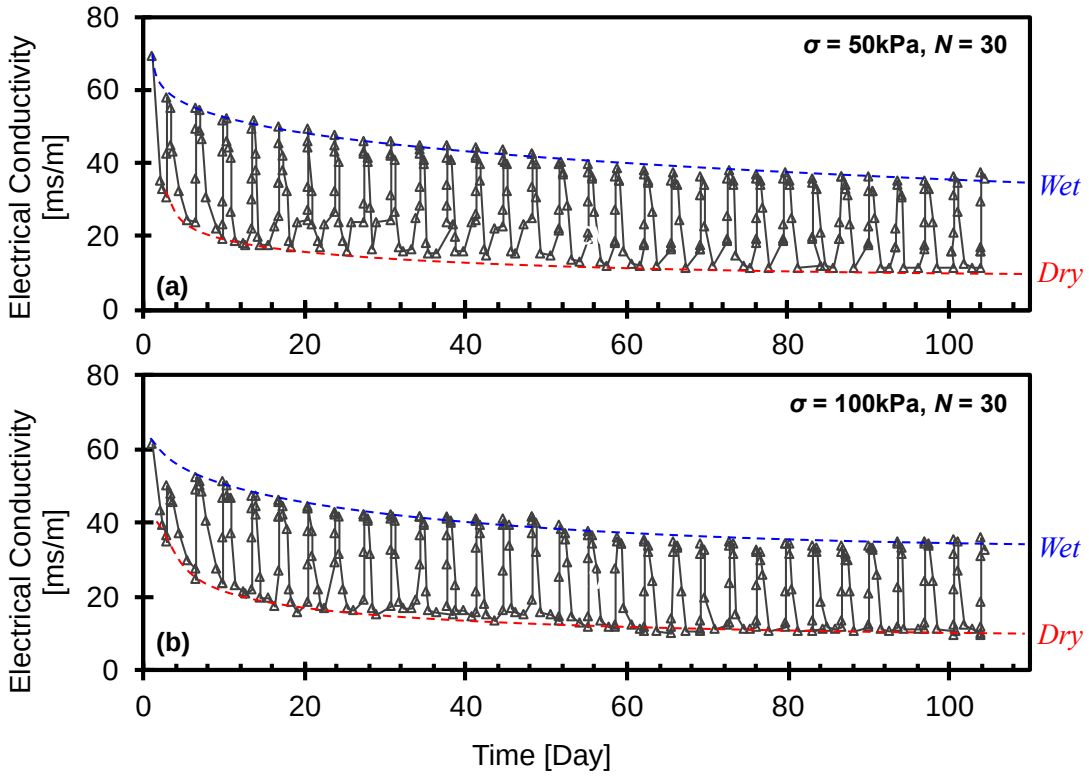

Figure 2.5. The change in electrical conductivity during the repetitive loading history. Test conditions: (a) σ_0 = 50kPa. (b) σ_0 = 100kPa.

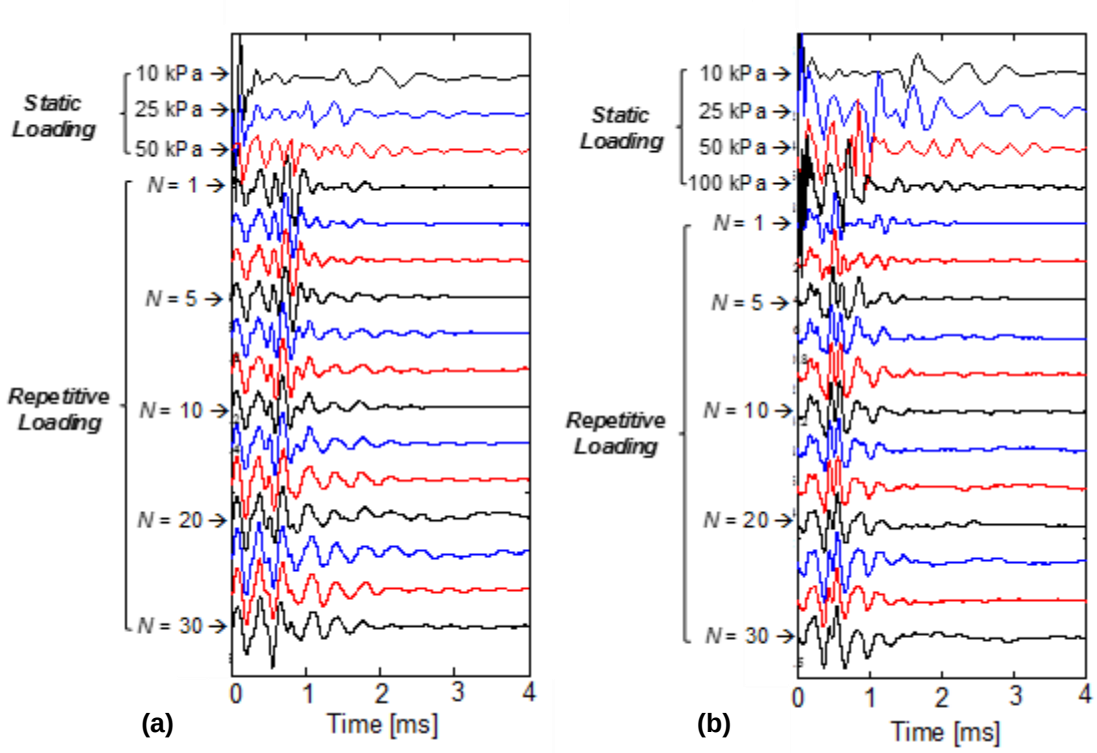

Figure 2.6. Cascades of shear wave signals captured during the static-repetitive (end of wet cycles) loading history. Test conditions: (a) σ_0 = 50kPa. (b) σ_0 = 100kPa.

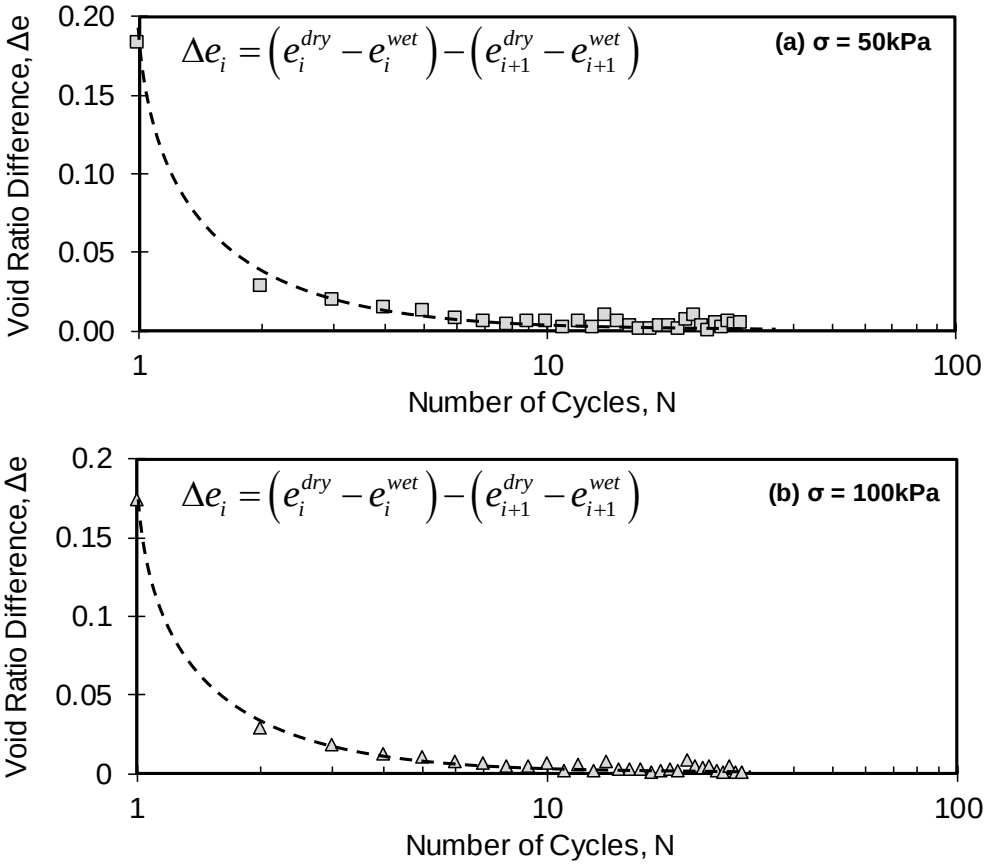

Figure 2.7. The void ratio difference between the residual void ratios of two consecutive wet-dry cycles. Test conditions: (a) σ_0 = 50kPa. (b) σ_0 = 100kPa.

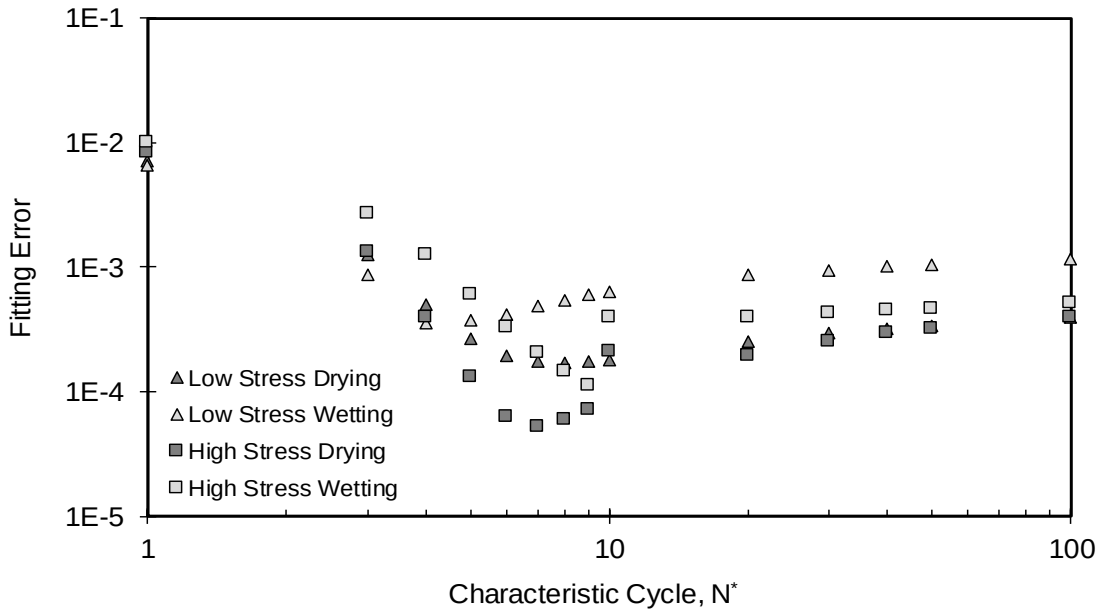

Figure 2.8. Model fitting error with characteristic number of cycles, N^*.

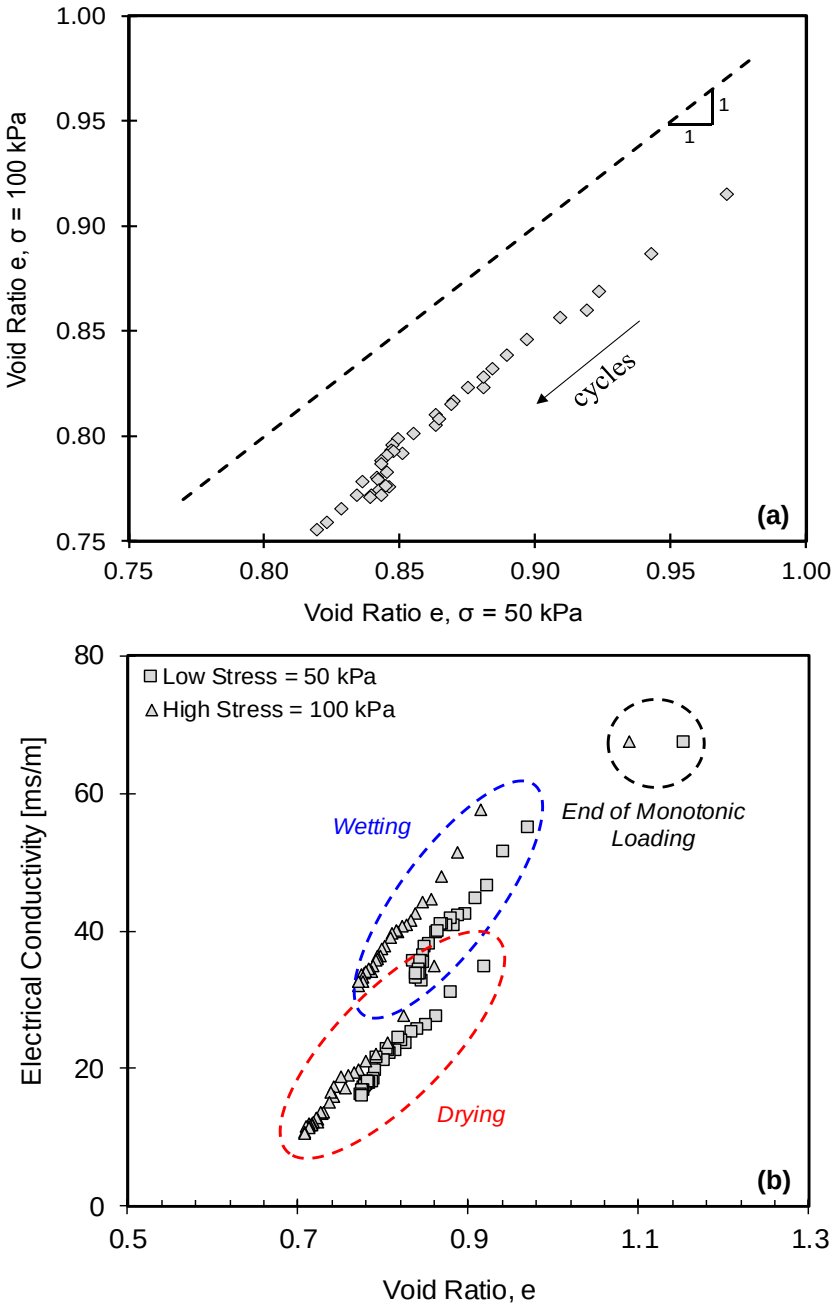

Figure 2.9. a) Void ratio evolution σ_0 = 100kPa versus void ratio evolution σ_0 = 50kPa during repetitive loading history. b) Evolution of electrical conductivity versus changes in void ratio during repetitive loading history.

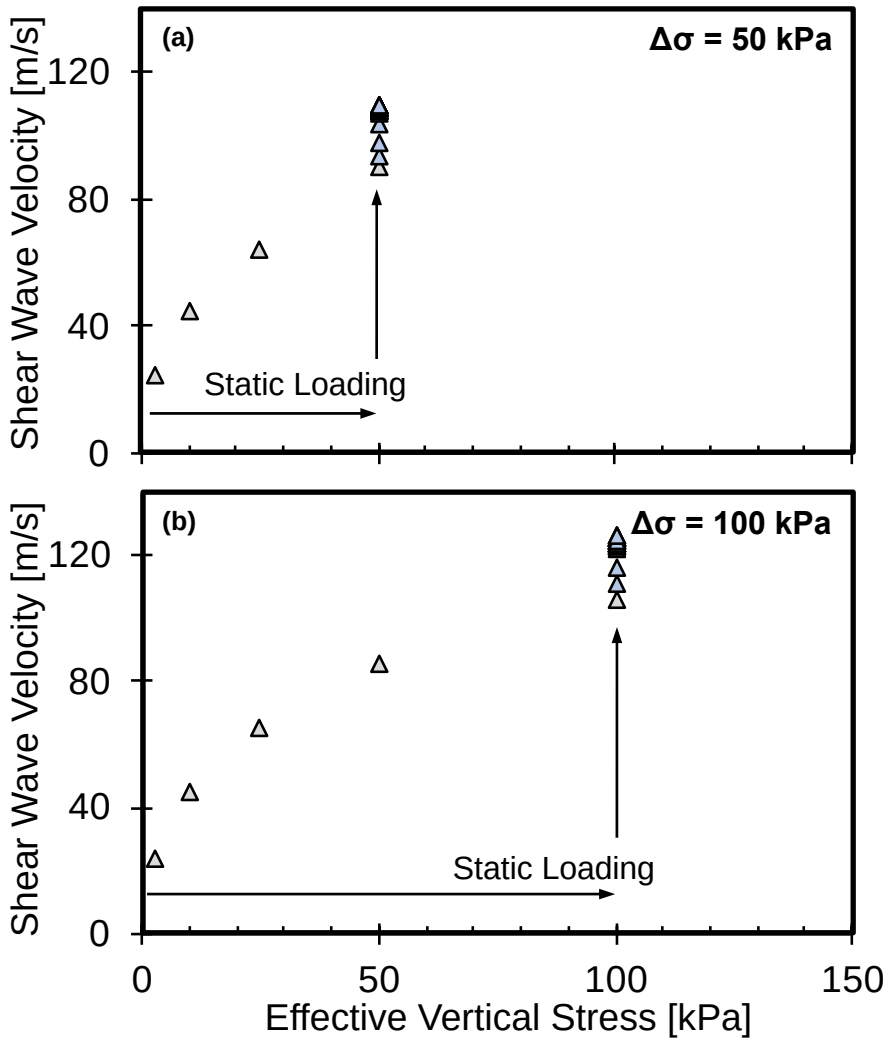

Figure 2.10. The evolution of shear wave velocity during static and repetitive loading stages - Particle contact and fabric change. Shear wave velocity versus stress in test conditions: (a) σ_0 = 50kPa. (b) σ_0 = 100kPa.

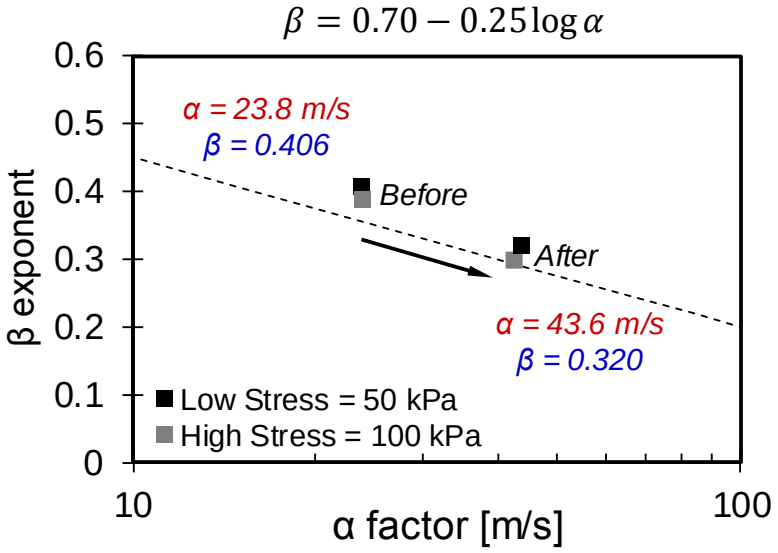

Figure 2.11. The α-factor and β-exponent before and after repetitive wet-dry cycles. Test conditions: (a) σ_0 = 50kPa. (b) σ_0 = 100kPa.

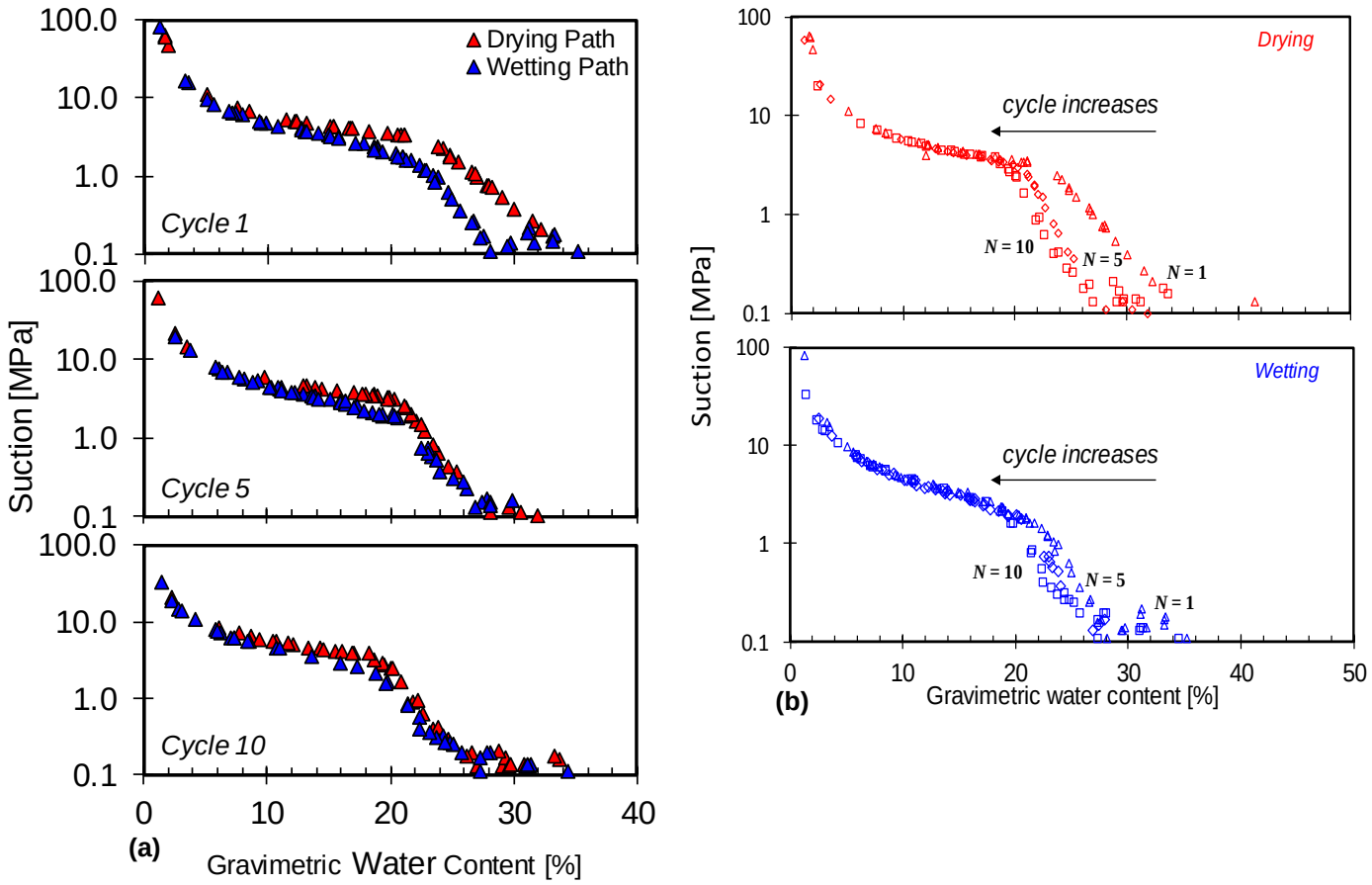

Figure 2.12. a) Scanning adsorption and desorption soil water characteristic curves. b) Evolution in soil water characteristic curves in wetting and drying paths. Test conditions: i) Cycle, $N = 1$; ii) Cycle, $N = 5$; iii) Cycle, $N = 10$.

CHAPTER 3. MINERAL PRECIPITATION CYCLES

3.1 Introduction

Mineral precipitation in geomaterials plugs pores and generates crystallization pressure. This phenomenon damages many geosystems exposed to salt water invasion (Benavente et al. 2007; Cardell et al. 2003; Chatterji and Jensen 1989; Mokni et al; 2010; Sayward 1984; Scherer 2004; Scherer et al. 2001; Alonso and Olivella 2008; Netterberg and Loudon 1980; Obika et al. 1989). Seasonal climate changes can result in salt precipitation accumulation, worsen the impact from these cycles (Goudie and Viles 1997).

The earth continents contain one billion hectares (~7%) affected by salt Ghassemi et al. 1995). Repetitive precipitation of salts degrades soil productivity, threatens ecosystems (Cook and Smally 1968; Gardner and Fireman 1958; Sharma and Prihar 1973), and deers arable farmlands (Abrol et al. 1988; Rengasamy 2002).

The presence of salt crystals in soils greatly affects their properties. Salt precipitation can disintegrate construction materials commonly used in civil engineering (Everett 1961; Goudie and Viles 1997; Scherer 2004; Steiger 2005). Sincerely, the crystallization pressure generated from the growth of salt crystals bursts the soil fabric (Lewin 1982; Evans 1969). In addition, the decrease in the hydraulic conductivty of deep soil layers and rocks due to precipitation cycles reduces oil well productivity and CO_2 injectability (Muller et al. 2009; Peysson 2012). Precipitated salt blocks pores near the injection wellhead and hinders the entire downstream sequestration process by decreasing the porosity and hydraulic

conductivity (Pruess and Garcia 2002; Fuller et al. 2006; Giorgis et al. 2007; Andre et al. 2007; Kim et al. 2012).

Precipitation studies advance the understanding of coupled processes involved in solute transport and chemical interactions in porous media. Hydrophobic surface treatments hinder salt precipitation and bonding in porous media (Cardiano et al. 2005). Conversely, a few important applications engineer precipitation process, such as include inkjet printing, surface coating and the manufacture of novel electronic and optical materials (van Hameren et al. 2012). The pharmaceutical industry requires crystals with controlled size, shape, purity, and polymorphism (Norbert et al. 2012).

This study explores mineral precipitation induced by wet-dry cycles at two different scales. (1) Droplet scale: a set of droplet tests investigate the effects of the substrate surface on NaCl salt precipitation. (2) Pore-scale: dry air flows into NaCl solution saturated microfluidic chips to trigger salt precipitation. Image analyses provide detailed information on the dynamic behavior involved in precipitation.

3.2 Salt Precipitation induced by Wet-Dry Cycles

Salt precipitation in soils due to wet-dry cycles requires an understanding of terms and concepts that are not part of standard geotechnical engineering practices. These are included next.

3.2.1 Primary and Secondary Precipitation

Climatic variations in temperature, relative humidity, and rain followed by drying lead to salt precipitation in the form of efflorescence or subflorescence (reference).

Subsequently, precipitated salts can redissolve by both dissolution and contact with water vapor. The resulting salt solution is mobilized in the porous network and becomes recrystallized when dried again due to relative humidity variations. The recrystallization that results from precipitation cycles is different to the initial crystallization. Phase transitions in the initial precipitation results in rapid crystallization rates and impurities in precipitated solids (Sunagawa 1999). Primary and secondary precipitation lead to different growth rates and crystallization patterns (Aquilano et al. 2009; De Yoreo and Vekilov 2003). The evaporation of homogeneous salt solutions in confined systems can reach high supersaturations in primary precipitation (Naillon et al. 2015). By contrast, secondary precipitation takes place at saturated concentrations (Sunagawa 1999). Cyclic precipitation dynamics in a porous medium depend on both thermodynamic and transport processes. These will also have a direct impact on the evaporation rate of the solvent from the porous network (Mullin 2001; Doherty et al. 1997; Oxtoby 1998; Desarnaud and Shahidzadeh-Bonn 2011).

3.2.2 Surface Properties on Precipitation Behavior

Wettability is an important property that describes how a liquid interacts with a solid surface. Wettability in air relates the three interacting phases: solid, liquid and gas. Young's equation relates their mutual interfacial tensions through the contact angle θ (Young 1805),

$$\gamma_{sv} = \gamma_{sl} + \gamma_{lv}cos\theta \tag{3.1}$$

where γ_{sv}, γ_{sl}, and γ_{lv} represent the interfacial energies of the solid-gas, solid-liquid and liquid-gas interfaces.

Hydrophilic and hydrophobic surfaces effect mineral precipitation phenomena on solid substrates (Deegan et al. 1997; Deegan et al. 2000). The evaporation is fastest near the edge on hydrophilic surfaces. Consequently, the contact line pins at the surface and solvent lost by evaporation near the edge is replenished. This phenomena causes a flow mechanism that transports the solute from the center to the edge. The resulting precipitation forms ring-like crystals at the edge. By contrast, the evaporation rate on hydrophobic surfaces is spatially uniform and the contact line does not pin at the surface. The air-liquid interface evolves from the edge towards the center of the droplet and forms large crystals in the middle (Shahidzadeh-Bonn et al. 2008; Takhistove and Chang 2002; Linnow et al. 2013).

Furthermore, Marangoni flows arise due to surface gradients along the interface because of the non-uniform evaporation, which unevenly draws energy from the drop and creates a temperature gradient. The resulting thermal conductivity of the substrate can change the direction of the Marangoni flow and alter the precipitation pattern (Ristenpart et al. 2007; Subra 2006).

3.2.3 Precipitation in Heterogeneous Porosity

Changes of capillary force and flow properties in a heterogeneous porosity system influences the salt precipitation distribution in natural soils (Nachshon et al. 2011; Lehmann and Or 2009; Pillai et al. 2009). Capillary pressure gradient from the difference in pore size distributions dries from the coarse pores domain as a support of drying in the fine pores domain. Consequently, the fine pores remains saturated long after the drying front propagates through the coarse region.

Despite the dominance of evaporation flux from the fine pores region, low concentration saturated system preferentially precipitate over the coarse regions of the surface due to the lower air entry pressure that reduces the number of remaining evaporating pores. Local evaporation rate increases from these spatially distributed pores. Salt precipitation distributions in heterogeneous system depends on pore size distributions and hydraulic properties of the porous media (Bergstad et al., 2017).

3.2.4 Geometric Scales on Precipitation Phenomena

(1) Pore Scale. In the absence of advection, capillary and osmotic-driven processes govern both the flow and solute transport in soil pores. Capillary pressure gradients induce macroscopic solute transport, which determines the salt precipitation distribution patterns at the macro-scale (Giorgis et al., 2007; Ott et al., 2011). Solute transport determines salt precipitation distribution at the micro-scale and defines reductions in the hydraulic conductivity (Ott et al., 2011, 2013; Roels et al., 2014; Shokri, 2014). Heterogeneity in the soil texture controls the water evaporation rate and the distribution of precipitation (Lehmann and Or 2009; Nachshon et al. 2011; Ott et al. 2013). Capillary induced flow from the macroporous to the microporous network compensates the evaporation from the microporous network in dual-porosity systems (Shokri et al. 2010). In water-wet systems, the capillary pressure contrast leads to an effectively higher drying rate of the macroporous system (Lehmann and Or, 2009; Nachshon et al., 2011). Consequently, salt precipitates preferentially in fine-textured regions while coarse-textured regions sustain a high gas conductivity (Nachshon et al. 2011).

(2) Matrix Scale. Salt precipitation and its effects on saline water evaporation in both homogeneous and heterogeneous systems consist of these two major stages (Shimojimaa et al. 1966; Nassar and Horton 1999; Fujimaki et al. 2006; Nachshon et al. 2011; Fisher 1923; Coussot 2000; Lehmann et al. 2008; Nachshon et al. 2011). First, there is a high and constant evaporation rate; the process is capillary-driven and continues as long as hydraulic connectivity exists between the receding drying front and air-water interface to sustain the high evaporation rate. Second, hydraulic conduction pathways start to disconnect, and vapor diffusion restricts the evaporation rate in the porous medium. Third, the evaporation rate falls subsequently as a result of the salt precipitation and salt crust formation on the top of the porous medium. Once the salt crust detaches from the bulk solution, the saturated solution limits the ongoing dissolution crystallization cycle and results in lower precipitation rates and crusts with larger crystallites.

3.2.5 Crystallization Pressure

Precipitation in soils generates crystallization pressure from the chemical potentials at both the crystal surface in contact with the pore walls and the crystal surface not in contact. Supersaturation promotes the crystallization pressure which is a disjoining pressure between the growing crystal and the confining surface. Repulsion between the crystal and the confining surface will retain a liquid film which pushes against the driving force to generate growth. The crystallization pressure depends on the curvature of the crystal when the thin film solution and the surrounding crystals reach equilibrium. However, the trapped solution between the surfaces of the crystal and pore wall disrupts the liquid film during drying and enhances supersaturation. The thin film solution between the confined crystal and the pore wall transports the dissolved ions. Analyses relate the

crystallization pressure to the crystal geometry and the crystal-liquid interfacial energy. The crystallization pressure increases with crystal size under a constant solution molality with the same crystal geometry. The degree of supersaturation is the ratio of chemical activities and chemical activity products (Buil 1983; Chatterji and Thaulow 1997; Flatt 2002). The crystallization pressure ΔP equation assumes that confined crystals are under anisotropic stresses (Steiger 2005),

$$\Delta P = \frac{RT}{V_m} \ln \frac{a}{a_0} \tag{3.2}$$

Where $\Delta P = P_c - P_l$ is the crystallization pressure with P_l the ambient pressure and P_c the pressure on the loaded face of the growing crystal, R is the gas constant, T is the absolute temperature and V_m is the molar volume of the solid phase. The supersaturation of the solution in contact with the growing crystal is a ratio, where a and a_0 are the solute concentrations in the saturated and the supersaturated solutions, respectively (Correns and Steinborn, 1939; Buil 1983; Chatterji and Thaulow 1997).

3.2.6 Microfluidic Techniques

Studies of transport in porous media often adapt microfluidic techniques (Harrison et al. 1993; Kopp et al. 1998; Khandurina et al. 2000; Ross and Locasio 2002) for a wide range of applications (Berejnov et al. 2008; Wu et al. 2010). Microfluidic chips range from simple micro-channel structures and networks to provide insight into the underlying mechanisms, to complex networks of interconnected channels with pore size distributions which match native porous media. In both cases, the capillary C_a and the viscosity ratio μ_v

characterize the immiscible displacement patterns in porous media (Lenormand 1990; Lenormand et al. 1988).

3.2.7 Representative Elementary Volume (REV) Method

Representative elementary volume method finds a minimum representative volume of soil (Miyazaki 2005; Razavi et al. 2007; Bear and Cheng 2010) in which the given soil parameter measures becomes independent on sample size (Bartoli et al. 2005; Li et al. 2009; Borges and Pires 2012; Ferreira and Pires 2016). In a two dimensional thin section (i.e. microfluidic chip study), the representative elementary area REA well represents the REV in an isotropic medium (Bear and Bachmat) and it widely applies into spatial heterogeneity and scale analysis. Although the inadequacy of REV method in determination of soil porosity cannot provide correct results in local void ratio and particle distribution (Al Raoush and Papadopoulos 2010; Mikunoki et al. 2016), it is a robust technique to introduce into quantitative analysis of precipitation results in microfluidic chip studies.

3.3 Experimental Study: Devices and Test Procedures

This experimental program explores the precipitation behavior of dried droplets on both hydrophobic and hydrophilic substrates, and crystallization cycles in microfluidics pore networks.

3.3.1 Fabrication of Microfluidic Chip

We use soft lithography techniques to fabricate the dual-porosity microfluidic chip with rectangular symmetry (Qin et al. 2010). The process includes: (i) mask design with computer-aided design software, (ii) mask printing of designed patterns, (iii) fabrication of

the silicon wafer master with negative photoresist (SU-8 2050), (iv) polymerization of polydimethylsiloxane PDMS using the master as a mold, and (v) bonding of the PDMS slab to a glass substrate through oxygen plasma (See Mazutis et al. 2013 for a detailed protocol). Figure 3.1-a illustrates the chip design. The microfluidic chip consists of nineteen by nineteen rectangular matrices separated by d_c = 100μm wide pore constrictions; all pore channels are 50μm high. Each rectangular matrix contains d_c = 10μm to form a dual-porosity in the microfluidic networks. The empty space above the porous-network pattern ensures a uniform flow field.

3.3.2 PDMS Surface Treatment (for hydrophilic response)

PDMS is hydrophobic. We create hydrophilic chips by treating the PDMS surface with a possibly valuable auto PVA solution: add PVA to Milli-Q water with 1% wt and stir at room temperature for 40 minutes; gradually increase the temperature to 100°C and stir for 40 minutes; reduce the temperature to 65°C and stir solution overnight; add water to compensate for evaporation loss. We inject the PVA solution immediately after plasma bonding and let the chip saturate for 10 minutes. Finally, we heat the chip in an oven with temperature of 110°C and use pressurized nitrogen to remove the residual PVA solution inside the channels (Trantidou et al. 2017).

3.3.3 Experimental Assembly

The experimental system consists of dual-porosity microfluidic chips, salt solution reservoirs, peristaltic pumps, and a high-resolution microscope (Figure 3.1-b). A computer controlled peristaltic pump connects with an inlet (d = 1/16”) and flows the salt solution into the microfluidic chip. A reservoir collects the residual salt solution that passes through

the chip from an outlet (d = 1/16”). After the microfluidic chip reaches saturation, the peristaltic pump pushes dry air (through a column filled with desiccants, RH = 0%) into the channel network and initiates salt precipitation. A high-resolution microscope captures the saturation, desaturation, and precipitation processes.

3.3.4 Microfluidic Chip Saturation and Desaturation

The saturation of untreated PDMS chip is time-consuming and incomplete due to hydrophobicity, consequently, part of the microfluidics chip remains unsaturated. By contrast, saturation of the treated-PDMS chip is fast and effortless because of the hydrophilic surface and high gas conductivity of PDMS. Salt solution saturates both large channels and the small-pore matrices in the pore network.

Dry air invades into the PDMS chip at a much faster rate than the treated-PDMS water-wet chip. In both cases, dry air invades the large channels first. Precipitation initiates as small-pore matrices start to desaturate by water evaporation.

3.3.5 Péclet Number

Péclet number describes the competition between conduction and diffusion. Both the mechanism are involved when air invades and desaturates the dual-porosity microfluidic chip in the experimental study.

$$P_e = \frac{advective\,transport\,rate}{diffusive\,transport\,rate} \tag{3.3}$$

$$P_e = \frac{Lu}{D} \tag{3.4}$$

where L is the travel length from inlet to outlet (L = 20mm), D is the molecular diffusion rate ($D_{air} = 2 \times 10^{-5} cm^2/s$) and u is the flow velocity induced by peristaltic pump ($u \sim$ 50mm/s). As a result, the Péclet number in the dual-porosity microfluidic chip experiment program is close to 5×10^5 which indicates that convection dominates in the system.

3.4 Experimental Results

The experimental study includes a series of precipitation cycles in microfluidics chips with two concentration NaCl solutions (C = 1M and C = 6M). This section presents detailed results for cyclic precipitation phenomena observed in both hydrophobic untreated chips and hydrophilic treated chips (several treatments of the PDMS surface and a set of precipitation tests in microfluidic chips confirm the repeatability of this experimental study). Preliminary tests at the droplet-scale follow.

3.4.1 Droplet Test and Contact Angle Measurements

We run a complementary set of droplet tests on hydrophobic (PDMS chip) and hydrophilic surfaces (PDMS-treated chip) to study the contact angle and precipitation patterns for different surface characteristics. Although there is a set of droplet tests conducted in this study, Figure 3.2 illustrates the two representative results.

Figure 3.2 shows the droplet (V = 10μL; C = 6M NaCl solution) and ensuing precipitation patterns captured on both the hydrophilic (treated-PDMS) substrate and a hydrophobic (untreated-PDMS) surface. The droplet that curls on the hydrophobic surface but spreads out on the hydrophilic surface during evaporation. Droplets of the same volume evaporate slower on the hydrophobic surface and leave behind larger salt crystals than

droplets on hydrophilic surface. The initial crystallization starts at the edge in both cases. As water evaporates, the receding droplet on the hydrophobic surface draws the crystals towards the center, and the crystal continues growing. Conversely, the first few crystals tend to adhere at the pinned contact line on the hydrophilic surface; solution replenishment towards the edge crystallization.

The ring pattern formation of the droplet depends on the competition between non-zero velocity and the evaporation rate. The volume change at the edge of the droplet becomes increasingly small as the contact line approaches, flow of fluid within the droplet compensates the vapor loss. The ring grows initially as a power law in time and further rapidly increases and diverges. When the change of droplet height is different from the evaporation profile (non-zero velocity within the droplet quickly rearrange the mass in the droplet), a ring forms. If the profiles are similar, a uniform droplet occurs.

3.4.2 Deformable Porous Medium

PDMS is a soft material (Young's modulus = 1.32MPa at 25°C; Johnson et al. 2014), and it deforms during crystallization, similar to soils and rocks.

Figure 3.3 presents the deformed matrices observed during the precipitation experiment in the microfluidic chip. Figure 3.3 (a) illustrates the capillary force pulls back the aligned individual PDMS pillars and forms "desiccation crack" like channels when dry air invades into the matrix. This phenomenon enlarges the pore space inside the matrix and creates preferential paths that allows air invasion. Figure 3.3 (b) presents key deformation features in the microfluidic chips due to the crystallization pressure. Despite the small size of the salt crystal (proportional to the contact area with the pore channel walls), the high

crystallization often damages the PDMS pore structure during precipitation: (1) distorted individual PDMS pillars; (2) deformed matrix channels; (3) swelling against PDMS plates and separation.

3.4.3 Air Invasion and Salt Precipitation: Hydrophilic (treated-PDMS)

Figure 3.4 presents the chronological sequence of air invasion and salt precipitation process in the hydrophilic (PDMS-treated) microfluidic chip saturated with 1M NaCl solution. Dry air invades the large channels first. Air invasion into the matrices includes "desiccation crack" like channels and layered penetration from the edges. The air-filled channels continue to grow and eventually connect with each other.

Salt precipitation takes place inside the matrices at the menisci formed around individual PDMS pillars. Crystal nucleation favors at the air liquid interfaces in the hydrophilic chip. There is minimal crystal precipitated in the large channels. Crystals precipitate in a scattered pattern when the initial saturating solution was 1M NaCl solution, whereas crystals form a patchy precipitation pattern when the 6M of NaCl solution filled the matrix.

3.4.4 Air Invasion and Salt Precipitation: Hydrophilic (untreated-PDMS)

Figure 3.5 presents the initiation and development of salt precipitation in the PDMS microfluidic chip saturated with 6M NaCl solution. The solute reaches the supersaturated state and nucleation initiates salt precipitation as soon as dry air begins invading the chip. Salt crystals develop within small channels in both directions throughout the matrix. This growth further branches out and forms crossed salt precipitates. Salt crystals also develop

in the large channels that separate the matrices, in fact, crystals grow in the large channels takes place at the expense of the crystals in the matrices. Crystal bridges across large channels and connect adjacent matrices. The evolution of the salt precipitation indicates that crystal morphology prevails: the tilted angle between the rectangular shaped salt crystal and the pore channel remains throughout the entire precipitation process. Overall, precipitation takes place in both matrices and in the large channels in hydrophobic chips.

3.5 Analysis and Discussion

Experimental studies in microfluidic chips disclose distinct precipitation features during both nucleation and crystal growth. This section analyzes these precipitation patterns informed by the complementary set of droplet tests on hydrophobic (untreated-PDMS) and hydrophilic surfaces (treated-PDMS) documented in Figure 3.2.

3.5.1 Precipitation Patterns in Hydrophilic and Hydrophobic Matrix

Figure 3.6 presents the precipitation patterns with detailed crystal morphologies inside the microfluidic chip matrices for (a) hydrophilic (treated-PDMS) medium (C = 1M); (b) hydrophilic (treated-PDMS) medium (C = 6M); and (c) hydrophobic (untreated-PDMS) medium (C = 6M).

Capillarity works against air invasion into the hydrophilic chip. The lower concentration NaCl solution results in scattered salt precipitates at the interface between air and liquid inside the matrices in hydrophilic chip. By contrast, the high concentration solution leads to patchy salt precipitation with clear air and liquid interfaces.

On the contrary, dry air invades the hydrophobic chip. Large contact angles favor flat crystal at the interfaces between air and liquid. Large precipitates form long bridge-like crystals across channels and facilitate salt growth in adjacent matrices.

3.5.2 Precipitation Patterns in Hydrophilic and Hydrophobic Fractures

Figure 3.7 presents the precipitation patterns and detailed crystal morphologies inside the microfluidic chip channels, i.e. “fractures”, for hydrophilic and hydrophobic chips. Interfacial properties form curved air-liquid interfaces in hydrophilic fractures. Salt crystals nucleate at air-water interfaces and continue growing supported by fluid transport, typically along the corners of the non-circular channels. Figures 3.7 (i) and (ii) capture interfacial precipitates and crystal growth preferentially near corners in hydrophilic fractures.

By contrast, salt precipitation in hydrophobic fractures displays different features. Individual crystals nucleate away from air-water interfaces (Figure 3.7 iii and iv). Then, crystal growth continues at the initial nucleation site and expands to form blocky crystals. The crystal orientation is set at nucleation and crystal morphology defines the development of precipitation.

3.5.3 Re-precipitation patterns during wet-dry cycles

Dissolution-precipitation tests are performed on the same hydrophilic (treated-PDMS) and hydrophobic (untreated-PDMS) chips following the initial drying cycle. We used 6M NaCl solution to re-saturate both chips. Salt crystals from the initial precipitation dissolve after hours of re-saturation process. Both the chips reach 100% of saturation. Then,

we impose the second drying cycle by permeating dry air once again. The high-resolution microscope images allow us to compare the precipitation features against the initial precipitation results.

Figure 3.8 presents the re-precipitation patterns after the second wet-dry cycle in both the hydrophilic (treated-PDMS) chip and hydrophobic (untreated-PDMS) chip. Images (i) and (ii) illustrate the same patchy salt precipitates in hydrophilic chip from the initial precipitation experiment and re-precipitation test. The star shaped salt crystal patch expands during re-precipitation. Images (iii) and (iv) show the channel crystals in the hydrophobic chip before and after re-precipitation. Crystal growth favors the initial precipitated site and extends into individual matrices. Some crystals in the fractures grow at the expense of crystals in matrices, i.e. Ostwald ripening. Molecules on the surface of the precipitated crystals are less stable than the ones in the interior. Consequently, thermodynamic-driven process occurs where small crystals (in matrix) dissolve and redeposit onto large crystals (in fractures) because large particles are more energetically favorable.

Crystal forces further deform the soft PDMS material and pushes the PDMS plate away from the other. Layering crystal patterns disappear after re-precipitation due to the swelling in the microfluidic structure. This phenomenon also takes place in re-precipitation tests within the hydrophobic chip.

3.6 Conclusion

- Solution droplets curl on hydrophobic surfaces but spread out on hydrophilic surfaces during evaporation. Crystals nucleate at edges. They migrate and

grow on hydrophobic surfaces but remain anchored and scattered on hydrophilic surfaces.

- NaCl precipitation and re-precipitation experiments in microfluidic chips provide unique insight of potential salt precipitation phenomena in geomaterials. Hydrophilic (treated-PDMS) and hydrophobic (untreated-PDMS) microfluidic chips exhibit distinct crystal formation patterns.

- Deformation in PDMS microfluidic chip originates from both the capillary forces and crystal forces. Capillary driven air invasion forms “desiccation crack” like channels inside the matrix; crystallization pressure distorts the individual pores and induces swelling between the PDMS plates.

- Air invasion and salt precipitation processes observed in both the hydrophilic and hydrophobic chips exhibit completely different pore invasion and salt precipitation phenomena. Crystal nucleation and growth in hydrophilic chips takes place at air-liquid interfaces both in channels and inside the matrix. By contrast, salt crystals nucleate inside the hydrophobic matrix due to local supersaturation, then, it forms bridging crystals across channels that develop into new precipitation in the adjacent matrix.

- The salt precipitation patterns in the hydrophilic matrix is scattered for low salt concentration but form salt patches for high salinity brine. The salt precipitation patterns in hydrophobic chips is characterized by crystal bridges across large channels as well as adjacent matrices

- The precipitation patterns in hydrophilic fractures benefit from fluid flow along corners. In hydrophobic chips, crystal deposits at the initiated nucleation site and continue to grow; geometric limitation controls the crystal formation and crystal morphology prevails.

- Re-precipitation captures the salt crystal development due to wet-dry cycles. Formation of new crystals prefers to precipitate at the initial precipitated sites. Precipitation in fractures develops at the expense of the crystals inside the matrices.

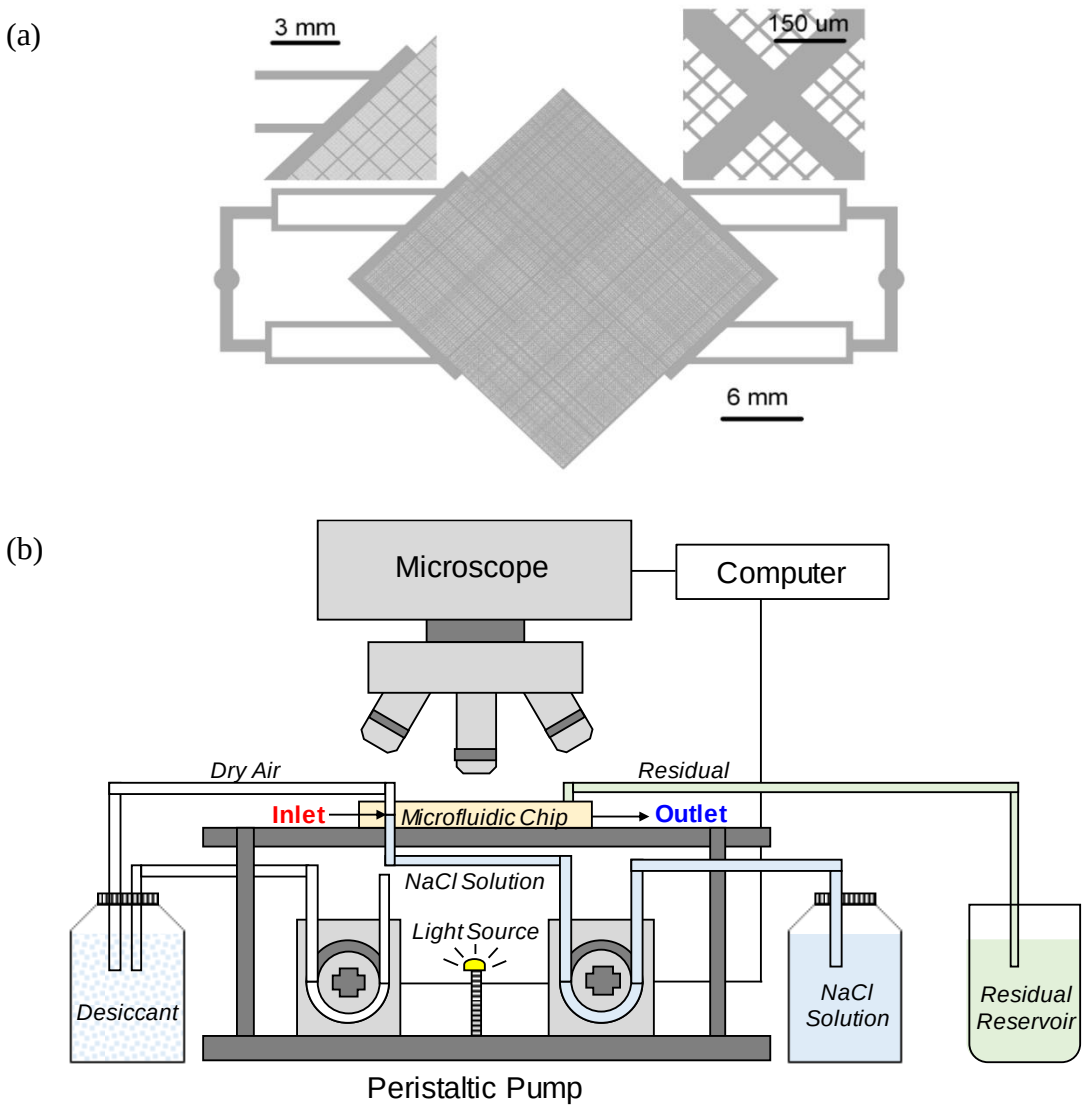

Figure 3.1. Device. Schematic drawing of the microfluidic chip system used for salt precipitation experiment. The microfluidic chip system includes a high-resolution microscope, an anti-vibration table, peristaltic pumps, and reservoir containers. Computer-controlled peristaltic pumps circulate NaCl solution (saturation phase) and dry air (drying phase) to perform precipitation inside the microfluidic chip. NaCl solution and dry air flow in from inlet (d = 1/16") and residual is collected from outlet (d = 1/16"). Microscope records time-lapse images. The dual-porosity microfluidic chip properties: total area = 498 mm^2, volume = 49.8 mm^2, total porosity = 41%, matrix porosity = 29%, hydrophilic (PDMS-treated) and hydrophobic (untreated-PDMS) surface.

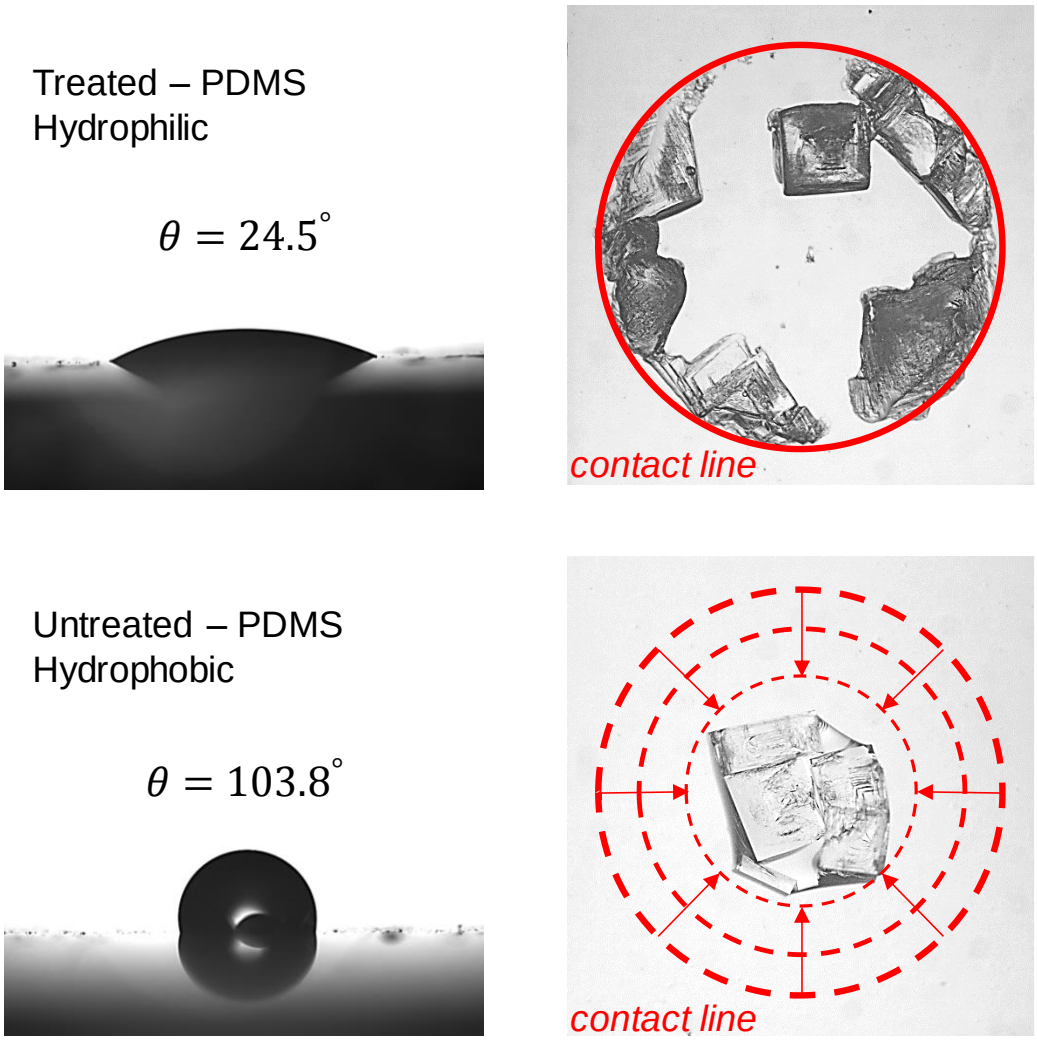

Figure 3.2. Droplet test and contact angle measurements. Droplet: V = 10μL; C = 6M NaCl solution. Hydrophilic (treated-PDMS) surface: pinned contact line, θ = 24.5°; hydrophobic (untreated-PDMS) surface: not-pinned contact line, θ = 103.8°.

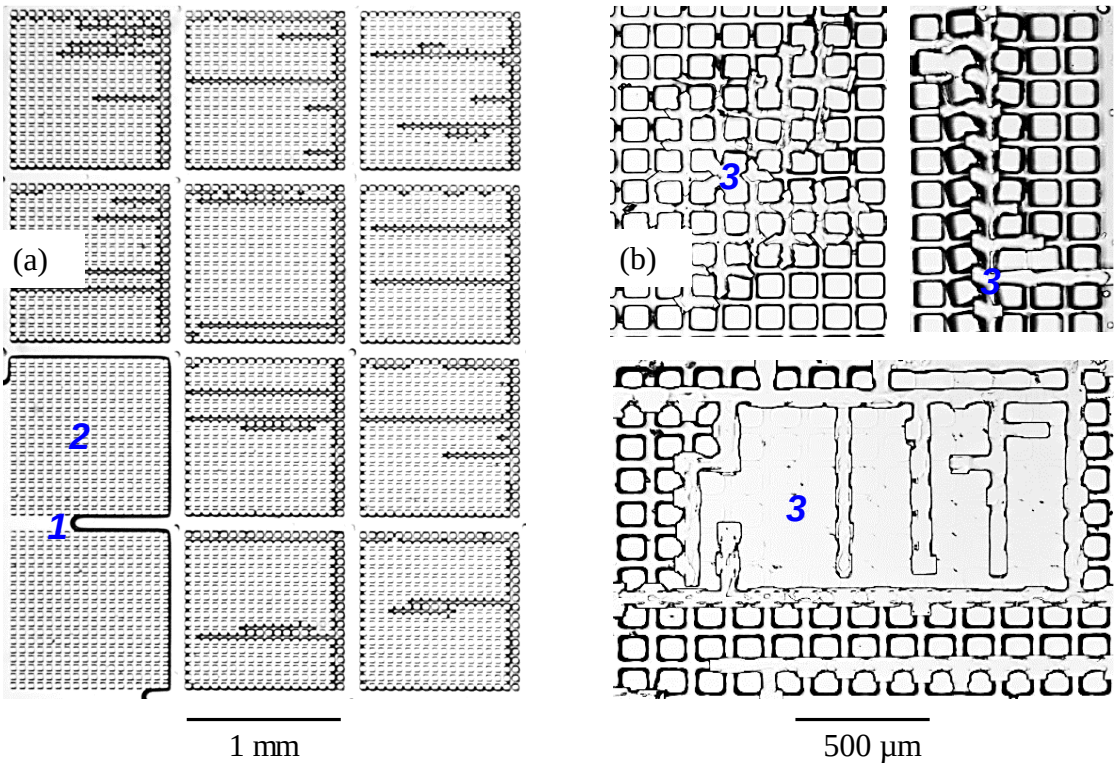

Figure 3.3. Deformable porous medium. (a) capillary forces: “desiccation cracks”; (b) crystal forces: “swelling”. Number: 1 = air; 2 = NaCl solution saturated matrix; 3 = NaCl salt precipitates.

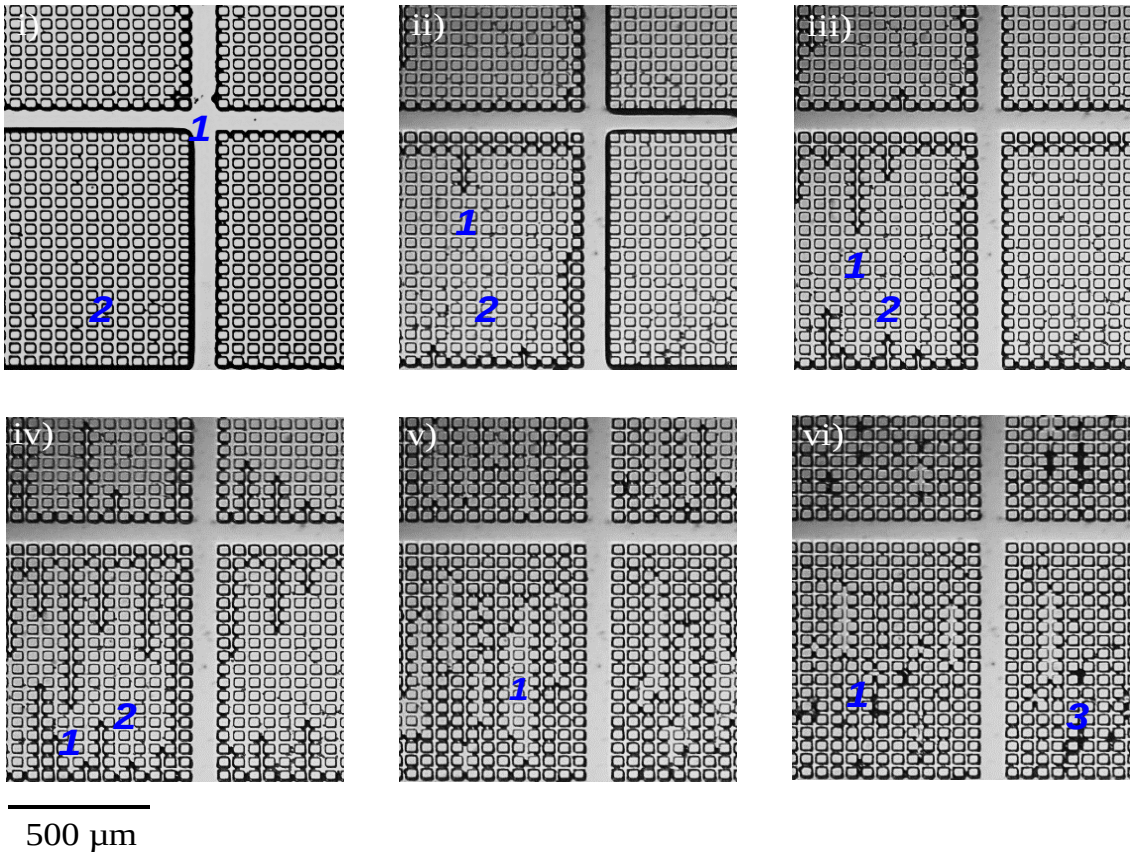

Figure 3.4. Air invasion and salt precipitation in hydrophilic (treated-PDMS) microfluidic chip. i) 1M NaCl solution saturated matrix; ii) capillary force driven air invasion; iii) individual "desiccation crack" channels form; iv) multiple channels continue to grow and develop; v) connected air invaded channels; vi) NaCl crystal precipitate inside the matrix. Number: 1 = air; 2 = NaCl solution saturated matrix; 3 = NaCl salt precipitates.

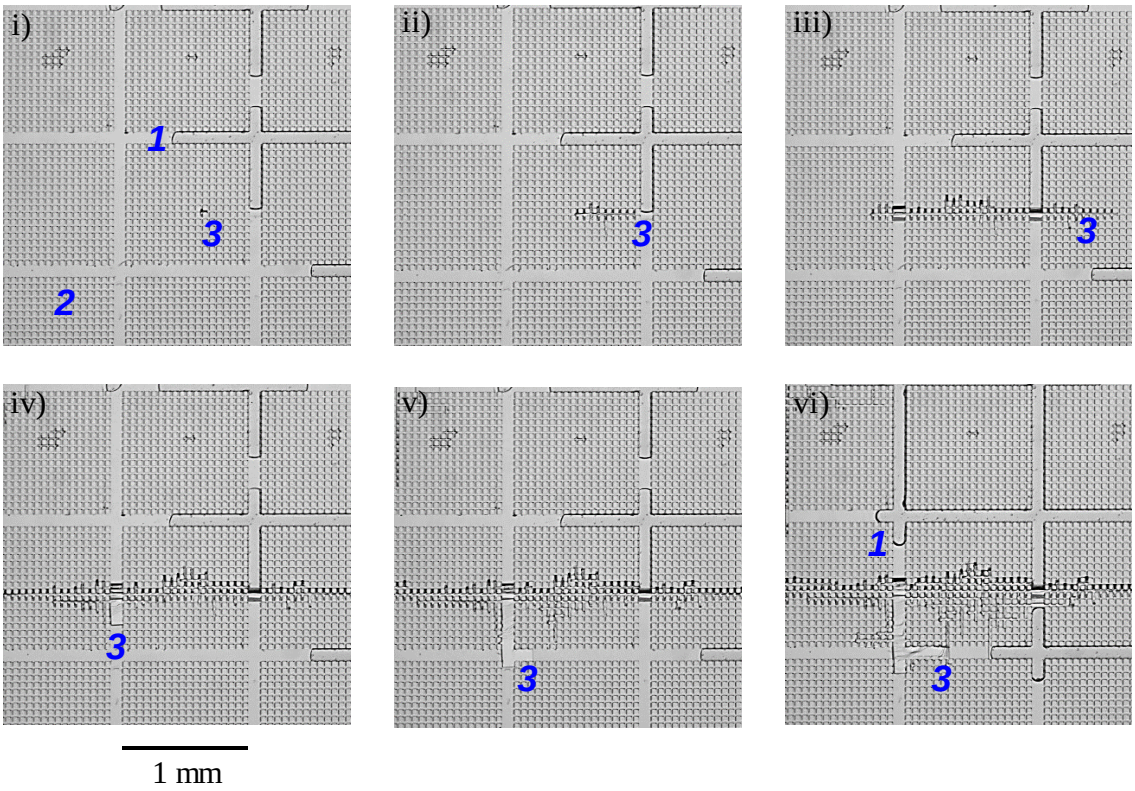

Figure 3.5. Air invasion and salt precipitation in hydrophobic (untreated-PDMS) microfluidic chip. i) 6M NaCl solution saturated matrix; ii) Nucleated site initiates salt precipitation; iii) Salt crystals grow horizontally from one matrix to its adjacent matrix; iv) Salt crystals continue to develop in vertical direction and extend precipitation in fractures; v) Morphology prevails the crystal growth in fractures; vi) NaCl precipitation develop in both the matrices and fractures. Number: 1 = air; 2 = NaCl solution saturated matrix; 3 = NaCl salt precipitates.

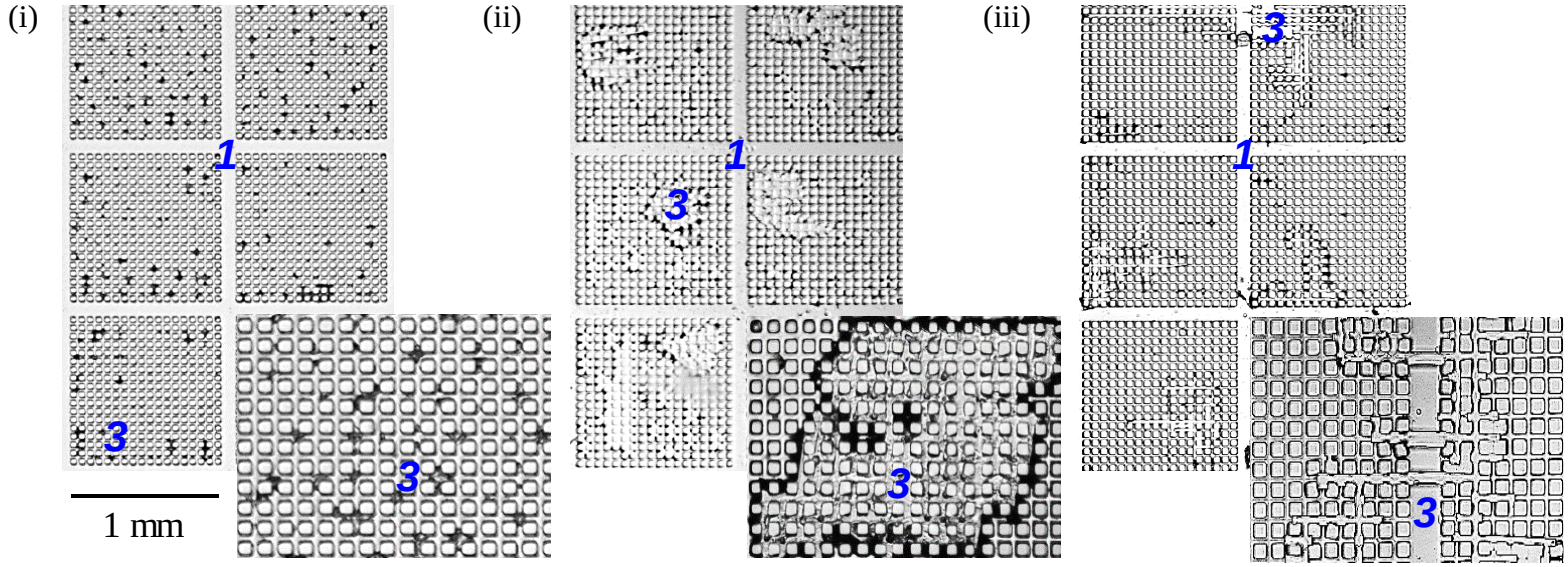

Figure 3.6. Air invasion and salt precipitation in hydrophobic (untreated-PDMS) microfluidic chip. i) 6M NaCl solution saturated matrix; ii) Nucleated site initiates salt precipitation; iii) Salt crystals grow horizontally from one matrix to its adjacent matrix; iv) Salt crystals continue to develop in vertical direction and extend precipitation in fractures; v) Morphology prevails the crystal growth in fractures; vi) NaCl precipitation develop in both the matrices and fractures. Number: 1 = air; 2 = NaCl solution saturated matrix; 3 = NaCl salt precipitates.

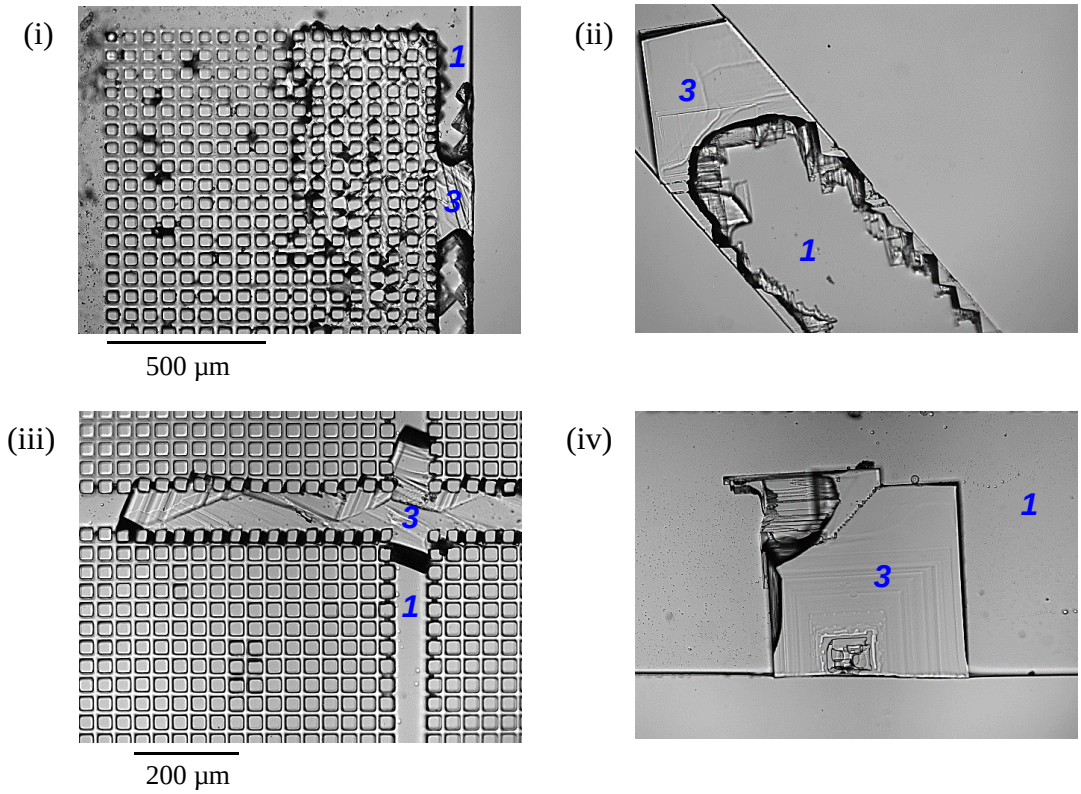

Figure 3.7. Precipitation patterns (NaCl solution; *C* = 6M) in hydrophilic (treated-PDMS) and hydrophobic (untreated-PDMS) fractures. (i) air-water interfacial salt precipitation in hydrophilic fracture; (ii) detailed salt precipitation in hydrophilic fracture; (iii) bridged salt precipitation in hydrophobic fracture; (iv) detailed individual NaCl precipitation block in hydrophobic fracture. Number: 1 = air; 2 = NaCl solution saturated matrix; 3 = NaCl salt precipitates.

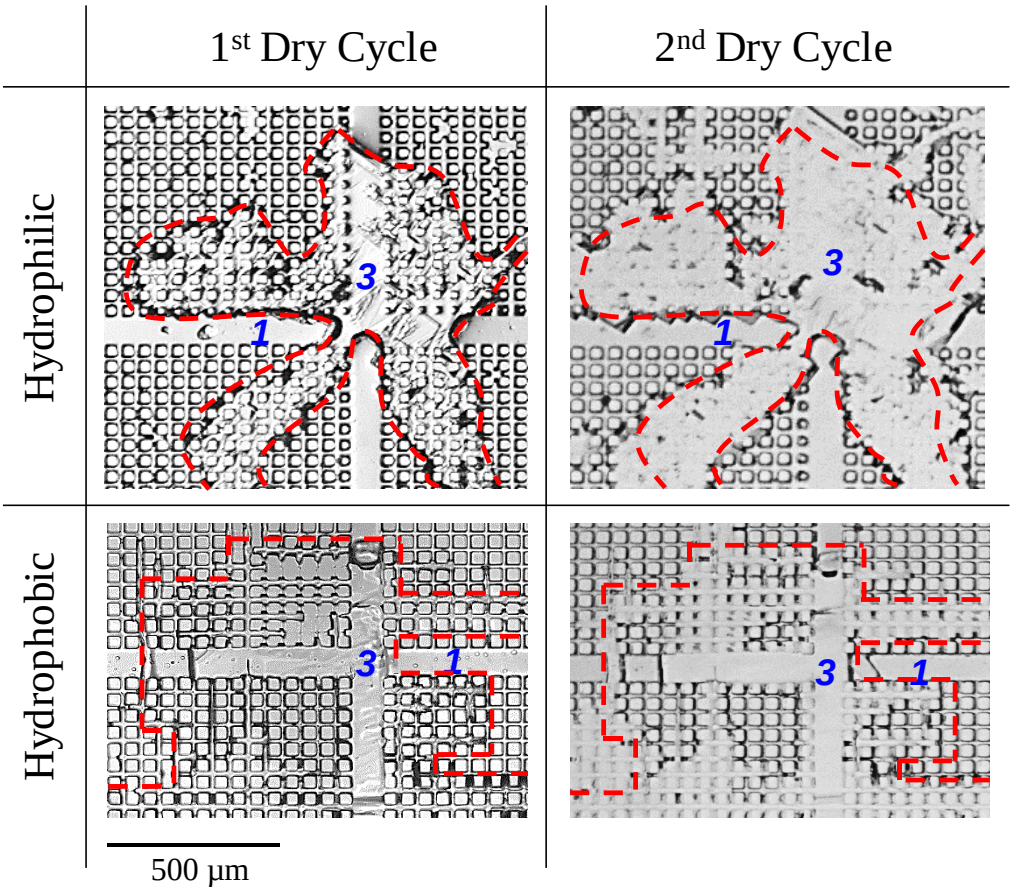

Figure 3.8. Re-precipitation (NaCl solution; *C* = 6M) patterns during wet-dry cycles. Top half: initial precipitation and re-precipitation in hydrophilic (treated-PDMS) chip; Bottom half: initial precipitation and re-precipitation in hydrophobic (untreated-PDMS) chip. Number: 1 = air; 2 = NaCl solution saturated matrix; 3 = NaCl salt precipitates.

CHAPTER 4. CHEMICAL CYCLES – k_0 CONDITION

4.1 Introduction

Fine-grained soils undergo repetitive and coupled thermo-hydro-chemo-mechanical processes in many engineering applications (Fredlund 1995; Mitchell 1991). Pore fluid chemistry impacts the behavior of fine-grained soils, in fact, their shear strength and compressibility are strongly dependent on pore fluid composition (Bolt and Miller 1955; Bolt 1956; Kenney 1967; Mesri and Olsen 1970; Mitchell 1973; Greenberg and Witherspoon 1973; Chattopadhyay 1972; Srideharan 1991; Moore 1991).

Chemical cycles repetitively alter the pore fluid compositions during engineering operations in many geosystems (Musso et al. 2003; Di Maio et al. 2004; Delage and Romero 2008; Thyagaraj and Rao 2013). Radioactive waste repositories, landfill clay liners, and the oil and gas industry often use compacted fine-grained geomaterials as isolating barriers and seals (Haug et al. 1988). These geosystems require construction materials with a low hydraulic conductivity, high exchange capacity, sufficient thermal conductivity, and adequate mechanical resistance. Fine-grained soils are susceptible to these pore fluid chemistry changes which result in substantial settlement, development of cracks, and changes in hydraulic conductivity (Shackelford et al. 1999; Mitchell 1993).

Natural systems experience changes in fluid chemistry as well, often related the infiltration of seawater and rainfall cycles which alternatively reduce and increase the concentration of the contained salt solutions.

This study explores the consequences of cyclic pore fluid changes in fine-grained soils through a set of carefully designed experiments complemented with detailed macro-scale and particle-scale analyses. A review of previous studies follows.

4.2 Soil Response to Repetitive Chemical Loads: Previous Studies

The analysis and discussion of soils subjected to repetitive chemical loads require terms and concepts that are not part of the standard geotechnical vocabulary. These concepts are briefly introduced next together with a review of previous studies.

4.2.1 Pore Fluid Chemistry

Fine-grained soils act as semipermeable membranes which inhibit the passage of electrolytes and generate concentration gradients (Staverman 1951; Kemper and Rollins 1966; Olsen et al. 1990; Keijzer et al. 1997). Particle-level electrical forces include the van der Waals attraction and double layer repulsion; both depend on the dissolved salt content and the permittivity of the pore fluid (Bulut et al. 2001; Rao and Shivananda 2005). Salt diffusion and concentration gradients alter the balance between electrical attraction and repulsion forces (Barbour and Fredlund 1989). Chemical-mechanical coupled consolidation reduces the diffused double layer thickness of the fine particles and leads to specimen compaction (Di Maio 1996; Fam and Santamarina 1995; Kaczmarek and Hueckel 1998; van Olphen 1977; Yong and Warkentin 1975; Mitchell and Soga 2005; Bolt 1956; Kenney 1967; Olson and Mesri 1970; Sridharan 1991). Repetitive physio-chemical cycles lead to the long-term sediment response (Di Maio et al. 2004; Musso et al. 2003).

4.2.2 Fabrics

Clay fabric formation primarily depends on the particle size and shape, clay mineralogy and pore fluid chemistry. Changes in the pore fluid chemistry induce cation exchange which changes the electrochemical forces and osmotic pressures (van Olphen 1977; Mitchell 1993; Palomino and Santamarina 2005; Sridharan and Prakasg 1999; Melton and Rand 1977; Chen and Anandarajah 1998; Ravisangar 2001; Pierre et al. 1995). The thickness of the double layer decreases with increases in ion concentration (Chapman 1913; Stern 1924). Then, cyclic fluid changes alter the double layer thickness, the equivalent effective stress, and fabric (Sridharan and Prakasg 1999; Fam and Dusseault 1998; Anandarajah 1997; Ravisangar 2001; Pierre et al. 1995).

4.2.3 Geophysical Monitoring

Electrical resistivity methods apply to a wide range of scales from the lab to field application. The electrical resistivity of saturated soils reflects the physicochemical properties of the mixture, i.e. the ionic concentration, porosity, and saturation (tortuosity, specific surface, and cation exchange capacity play a second role). Electrical monitoring and imaging can locate heterogeneities (Borsic et al. 2005) and monitor chemical diffusion in soils (Comina et al. 2005; Damasceno and Fratta 2006).

Seismic wave velocity provides important information about the mechanical response of the soil skeleton (Brignoli et al. 1996; Jovicic et al. 1996; Lee and Santamarina 2005). One-dimensional consolidation experiments can capture the mutual relationships among electrical, seismic, and mechanical properties of clayey soils undergoing chemical diffusion (Santamarina and Fam 1995).

4.2.4 Particle-Particle Interactions

The double layer repulsion decreases at high ionic concentrations, van der Waals forces dominate and favors face-to-face aggregation. This aggregation takes place at concentrations greater than 0.15M (Palomino and Santamarina 2005). Aggregates that form through edge-to-edge and edge-to-face interactions result in a high void ratio particle structure (van Olphen, 1977; Rand and Melton, 1977; Melton and Rand, 1977; O'Brien, 1971). By contrast, at low ionic concentrations, the double layer is thick and clay particles are deflocculated-dispersed.

4.2.5 Chemical-Mechanical Coupling

The diffusion of a high concentration ionic front tends to promote volumetric contraction. This implies the transfer of a skeletal load onto the pore fluid and the generation of a pore pressure front that may even propagate ahead of the ionic front that caused it (Santamarina et al. 2002). The amplitude of the pressure front in kaolinite can be of the order of the applied confinement. Modifications of Terzaghi's effective stress model for soil attempt to account for local, contact-level electrical forces and both series and parallel models have been assumed (see review in Hueckel, 1992):

$$\sigma' = \sigma - u = R_{DL} - Att \qquad \textit{Series Model} \tag{4.1}$$

$$\sigma' = \sigma_{total} - u - \left(R_{DL} - Att\right) \qquad \textit{Parallel Model} \tag{4.2}$$

In the series model, an increase in the repulsion force must oppose an applied stress to maintain equilibrium. This model is the most applicable to describe volumetric strains for

parallel particle packing (face-to-face aggregations) or for very fine soils, such as montmorillonite. The parallel model explains the changes in shear strength due to changes in pore fluid characteristics at a constant confinement. At the macroscale, the behavior of most clays appears to resemble some combination of both models.

4.2.6 Time Scales and Diffusion Fronts Arrival

Chemical diffusion and hydraulic conductivity control the rate of chemical-mechanical coupling. Both transport process may coexist; for example, hydraulic conduction along large interconnected pores is often complemented by diffusion into the smaller pores. The corresponding time scales are related to the length scale H as,

$$t = \frac{H^2}{D_{medium}} \qquad \text{Diffusion} \tag{4.3}$$

$$t = \frac{H}{ki} \qquad \text{Hydraulic Conduction} \tag{4.4}$$

where D_{medium} [m^2/s] is the diffusion coefficient of the geomaterial; k [m/s]; is the hydraulic conductivity of the geomaterial; and i [dimensionless] is the hydraulic gradient of the conduction flow path.

4.2.7 Volumetric Strain: Terminal State

The overall volume decreases during ionic diffusion and associated double layer contraction can open fissures and cracks and further increase hydraulic conductivity (Barbour 1987). Advective-diffusion ionic transport (and cycles) are time dependent. The

convergence rate towards the terminal state depends on the initial stress level, mineral composition, and cyclic concentration amplitudes.

4.3 Experimental Study: Devices and Test Procedure

This experimental program explores the evolution of the void ratio and the small strain stiffness of kaolinite specimens subjected to repetitive chemical loads under zero-lateral strain conditions.

4.3.1 Stress-Controlled Repetitive Loading System

The repetitive loading system consists of an instrumented fixed-ring oedometer cell and two reservoirs which alter the pore fluids of the specimen. (Figure 4.1). We use standard arm oedometers to ensure constant long-term mechanical load. The two reservoirs are filled NaCl solution (C = 0.1M; C = 0.2M; C = 1M) and with deionized water. A three-way valve alternates the flow from the two reservoirs: The main goal is to maintain a constant effective stress throughout the test. Gravity drives the fluid from the elevated reservoirs into the specimen from the bottom to the top.

The tall fixed-ring oedometer cell design compensates for the expected settlement (ID = 106mm, 10mm wall thickness, and 100mm high). We design thick top and bottom caps to incorporate fluid conduction throughout the system. The reservoir container collects overflow fluid and residual fluids from each exchange cycle.

4.3.2 Vertical Deformation Monitoring

The LVDT (TransTek DC 0242) clamped to the reaction frame tracks the vertical deformation of the specimen. A data logger (Keysight 34970A, Figure 4.1) saves the data from the LVDT readings.

4.3.3 Shear Waves: Bender Elements

The top and bottom caps include bender elements mounted with removable nylon screws. Grounded parallel-type bender elements for both source and receiver minimize crosstalk (Lee and Santamarina 2005). The bender elements are 12.7mm × 8mm × 0.7mm in size and mounted with a 5mm cantilevered length (7.7mm anchored length). The function generator sends a 10V step signal every 50ms (Keysight 33210A). Received signals go through a filter-amplifier (Krohn-Hite 3364 - 500 Hz high-pass and 200 kHz low-pass window) before averaging in the oscilloscope and stored in the data drive. (Keysight DSOX 2014A - 1024 stacked signals - See implications of signal stacking in Santamarina and Fratta 2005).

4.3.4 Electrical Conductivity: Electrodes

We measure eletrical conductivity using single wire copper cables as electrodes. The oedometer ring includes electrodes glued at the same elevation. Both electrodes connect with a known resistor in a series to measure the electrical current flowing through the specimens. The function generator sends a 1V step signal with frequency of 10kHz (Keysight 33210A). A datalogger records the voltage drop through the specimen and the

resistor. The soil resistivity is a function of measured resistance R and the geometric factor β,

$$\rho = \beta R[\Omega \cdot m] \qquad \textit{Electrical Resistivity} \qquad (4.5)$$

$$\sigma = \frac{1}{\rho}\ [S/m] \qquad \textit{Electrical Conductivity} \qquad (4.6)$$

We determine the geometric factor by filling the cell with electrolytes of known resistivity as shown in Figure 4.2.

4.3.5 Specimen and Solution Preparation

This experimental study uses Georgia Kaolinite RP-2 ($LL_{\text{deionized}}$ = 67%; LL_{brine} = 52%; LL_{kerosene} = 82%). NaCl solutions were prepared with different concentrations (C = 0.1M; C = 0.2M; C = 1M). Table 4.1 summarizes the salinity levels of the selected NaCl solutions in comparison to field conditions. Table 4.2 presents the physical and engineering properties of the kaolinite RP-2 used for this experimental study.

4.3.6 Test Procedure

We missed kaolinite with deionized water to a w = 1.5LL to form a saturated soft paste. Then, we filled the oedometer cells leering no trapper air. The loading procedure for all specimens consists of three stages: (1) static loading to σ_0; (2) cycles of advective flow with low-and-high concentration, N = 5; (3) unloading. Three measurements take place every three days during each brine and deionized cycle: (1) shear waves velocity; (2) electrical resistance; (3) overflow collection. We record the overflow weight differences

from the reservoir containers for hydraulic conductivity estimation. Repetitive fluid cycles (brine to deionized water) have an average period of 80 days. Three parallel tests are subjected to different salt concentration in pore fluid exchanges. Increase in salt concentrations agrees well with experimental results. Figure 4.3 summarizes the test sequence.

4.4 Experimental Results

Low concentration cyclic tests exhibit a similar trend to the high concentration cyclic tests. Chemical-mechanical coupled consolidation results in higher volumetric contraction in earlier cycles ($N = 1$ and $N = 2$) than later cycles. Pore fluid changes induce irrecoverable strains in the system in early cycles. Soil responses under repetitive chemistry cycles tend to evolve towards elastic behavior. This section presents detailed experimental results for kaolinite subjected to two target concentrations (C = 0.1M; C = 0.2M; C = 1M). The following section contains a complete analysis of the dataset.

4.4.1 Void Ratio, e vs. Time

Figure 4.4 presents the evolution of the void ratio of kaolinite subjected to the static-repetitive loading history. The static loading stage contains three steps (i) σ_0 = 3kPa (seating pressure); (ii) σ_0 = 20kPa; (iii) σ_0 = 40kPa. The following repetitive loading stage consists of three different pore fluid conditions (C = 0.1M; C = 0.2M; C = 1M). The void ratio of kaolinite from all three tests decreases monotonically during the initial static loading stage as indicated by the gray curves. The red curves show the void ratio response subjected to brine cycles; the blue curves indicate the void ratio response subjected to deionized water cycles. Deformations induced by mechanical static loading are much more pronounced

than chemical-mechanical coupled repetitive loading. The specimen continues to consolidate as the cycle proceeds because the deionized water cycles that follow cannot fully recover the volumetric contraction induced by brine cycles.

4.4.2 Electrical Conductivity

Figure 4.5 presents the electrical conductivity evolution during repetitive pore fluid changes. Electrodes embedded inside the specimen record the electrical conductivity measurements of the pore fluids along with every shear wave measurement. Overflow from the top of the specimen measures the electrical conductivity of free fluids that flow through the specimen. The electrical conductivity of the overflow pore fluids is higher than the electrical conductivity inside the specimen. The delayed response between the two measurements is the time difference that the diffusion fronts reaches half of the specimen and the top of the specimen.

4.4.3 Shear Wave Signals

Figure 4.6 shows the shear wave signal cascades recorded from the static-repetitive loading history. The travel time decreases during the first quasi-static loading stage. A significant first arrival delay induced by pore fluid changes during the first cycle result in the influence on fabrics. Changes in the first arrival are not as pronounced as the first cycle during the following cycles. The time-stretched cross-correlation method in CODA wave analysis assesses these minor changes in travel time (Snieder 2006; Dai et al. 2013). The stretching factor θ allows the determination of minute changes in the shear wave velocity during repetitive loading cycles.

4.5 Analyses and Discussion – Complete Dataset

In this section, we report and analyze the complete dataset produced with the tests performed in this study.

4.5.1 Volumetric Strain, ε vs. Time

Figure 4.7 presents the volumetric strain evolution of the chemical-mechanical coupled repetitive loading stage for all three tests. The clay specimen contracts when subjected to brine solutions (red curves) and swells under deionized water (blue curves). Higher concentration gradients result in more significant chemical-mechanical coupled consolidation and swelling. The recoverable and irrecoverable strains are identified at earlier pore fluid change cycles. The plastic strain accumulation becomes negligible as the number of cycles increases and remains hysteretic, i.e., a plastic shakedown.

4.5.2 Void Ratio, e vs. Effective Stress, σ'

Figure 4.8 summarizes the void ratio response with different effective stress during the static loading stage for all three tests. The void ratio response is a function of the consolidation coefficient and effective stress.

$$\Delta e = C_c \log\left(\frac{\sigma_0 + \sigma_c}{\sigma_0}\right) \tag{4.7}$$

Inter-particle electrical forces contribute to the chemical-mechanical coupling in addition to the initial static loading. An extended one-dimensional consolidation equation connects the void ratios at the end of the first brine cycles for all three different concentrations (C = 0.1M; C = 0.2M; C = 1M). The equivalent effective stress increases

when the concentration of the subjected pore fluids increases. Void ratio differences indicate how particle-level electrical forces influence the soil fabrics during chemical-mechanical coupled consolidation. The increment in the concentration gradient results in a logarithmic relationship with the void ratio response because the particle-level electrical force is proportional to concentration.

4.5.3 Void Ratio, e vs. Concentration

Figure 4.9a presents the comparison of the volumetric strain with corresponding pore fluid concentrations between experimental results and analytical solutions. Let's assume that particles are circular discs, parallel to each other at a separation *t* (Santamarina et al. 2002).

Attraction $$F_{Att} = \frac{1}{24}\frac{A}{t^3}d^3 \tag{4.8}$$

Repulsion $$F_{DL} = 16\pi \mathrm{RT} c_0 d^2 e^{-\frac{t}{\vartheta}} \quad \text{large } t \tag{4.9}$$

$$F_{DL} = \frac{1}{2}\pi \mathrm{RT} c_0 d^2 \left(\frac{2\pi^2 \vartheta^2}{t^2} - 1 \right) \quad \text{small } t \tag{4.10}$$

Weight of disk $$\mathrm{W} = \frac{\pi}{4}\frac{\gamma_s}{\alpha g}d^3 \tag{4.11}$$

Then consider platy particles stacked parallel to each other with adsorbed layers in between, and in equilibrium with an applied constant normal stress σ_0. The strain experienced by the stack of discs due to the change in chemical concentration ΔC_0 reflects the change in the pore fluid thickness. The following simplified expression is obtained for

a small concentration change ΔC_0 (second order Taylor expansion) and only considers the repulsion force,

$$\varepsilon = \frac{t_f - t_0}{L_s + t_0} \approx \frac{\pi T^2 R^2 \gamma_s \sqrt{\varepsilon/2}}{gFz} \frac{S_a \Delta c}{\left(\sigma + 2RTc_0\right)^{3/2}} \tag{4.12}$$

As discussed in the fabric map, the pH and ionic concentration define both the particle association and fabric formation. Fabric formation contributes to the deviation between experimental results and analytical solutions.

Figure 4.9b presents the comparison between the equivalent effective stress from analytical solutions and a fitting consolidation equation. This study adapts the true effective stress model to explain changes in clay properties with changes in the pore fluid chemistry (Sridharan and Sivapullaiah 1987). The true effective stress in the parallel model is more suitable to describe the experimental results with kaolinite due to considerations of fabric formation and particle size. The equation below transfers the inter-particle electric forces into equivalent effective stress coupled with static mechanical loading, where *k* is a coefficient as a function of packing and fabric formation.

$$\sigma' = \sigma_{total} - u - k\left(R_{DL} - A_{tt}\right) \tag{4.13}$$

Based on the fitting results, a parallel model with the effective particle to particle association parameter, *k* represents the validity of the model and physically-inspired prediction.

4.5.4 Hydraulic Conductivity

Figure 4.10 presents the evolution of the hydraulic conductivity measured at the end of every pore fluid cycle. The eight differences from the overflow reservoir provide an accurate estimate of the number of pore fluids exchanged during each cycle. Pore fluid changes per unit time determine the hydraulic conductivity. As the number of cycles proceeds, the hydraulic conductivity for both brine and deionized water decreases. The delay displayed in the electrical conductivity measurements also confirms the decrease in hydraulic conductivity trends inside the specimen through the pore fluid cycles. Measurements from the electrodes embedded in the middle of the specimen and measurements from the top overflow reservoir result in a delayed response. When the pore fluid arriving front reaches the electrodes, it takes more time to conduct through the upper layer of the specimen to reach the overflow reservoir. The gap time in electrical conductivity measurements is a result of the delayed chemical conduction time between the electrodes and overflow reservoir.

4.5.5 Shear Wave Velocity during Static Loading

The shear wave velocity is a power function of the vertical σ'_z and horizontal σ'_x effective stresses (Roesler 1979; Yu and Richard 1984; Santamarina et al. 2001):

$$V_s = \alpha\left(\frac{\sigma_z^{'}+\sigma_x^{'}}{2\,kPa}\right)^{\beta} = \alpha\left(\frac{\sigma_z^{'}}{1kPa}\right)^{\beta}\left(\frac{1+K_0}{2}\right)^{\beta} \tag{4.14}$$

Where the where the α-factor is the shear wave velocity at effective stress σ'_{mean} = 1kPa, and the β-exponent represents the stress sensitivity of the shear wave velocity. The shear wave velocity-stress relation captures both contact behavior and fabric changes (Cha et al. 2014).

Figure 4.11 summarizes the evolution of the shear wave velocities during the static and end of brine cycle for different concentration gradients (C = 0.1M; C = 0.2M; C = 1M). Figure 4.12 presents the α-factors and β-factors computed by fitting Equation 4.10 to the static load stages before and after repetitive loading for all tests. The data trend is consistent with the relationship between α and β values reported by Cha *et al.* 2014. Overall, the kaolinite becomes stiffer (lower C_c) as the α-factor increases and the β-exponent decreases. The soil fabric becomes less sensitive to stress changes after repetitive loading.

4.5.6 Shear Wave Velocity during Repetitive Loading

Figure 4.11 presents the shear wave velocity against the number of loading cycles for all three tests. The shear wave velocity increases as the number of repetitive loading cycle progresses. Higher concentration gradients result in stiffer fabrics after the pore fluid cycles. Previous chemical induced fabric changes did not recover in the following cycles. The hysteresis present in the shear wave responses indicates that the residual fabric change remained in the soils during repetitive pore fluid cycles. The rate of increase in small-strain stiffness during repetitive loading is more pronounced in kaolinite in the earlier cycles than later cycles.

4.6 Conclusion

The void ratio, electrical conductivity, and the small strain stiffness of Georgia Kaolinite RP-2 during quasi-static repetitive pore fluid chemistry loads under zero-lateral strain conditions lead to the following notable conclusions.

- The void ratio evolves towards the terminal void ratio e_T as the number of pore fluid chemistry cycles $i \rightarrow \infty$. The terminal void ratio e_T is a function of the initial void ratio e_0 when repetitive loads take place under k_0-condition. In other words, the soil retains memory of its initial fabric.

- Salt concentration levels lead to changes in particle level electrical forces and influence the particle-particle association. Evolution of kaolinite fabrics result in macroscopic chemical-mechanical coupled response in soil behavior.

- Pore fluid chemistry exchange gradually reduces the hydraulic conductivity of kaolinite as the number of chemistry cycles $i \rightarrow \infty$.

- The changes in void ratio and small strain stiffness during repetitive loading reveal that repetitive k_0-loading results in denser, stiffer, and less attenuating kaolinite fabrics.

- Shear wave velocity-stress trends $V_s = \alpha(\sigma'_{mean}/\text{kPa})^{\beta}$ capture both contact behavior and fabric changes. Data show that kaolinite become stiffer (lower C_c), the α-factor increases, the β-exponent decreases and the soil fabric becomes less sensitive to stress changes after repetitive loading.

- The increase in shear wave velocity indicates a gradual increase in horizontal stress during repetitive loading under zero lateral strains.

- Data gathered in this experimental program suggest a simple calculation to estimate the equivalent effective stress experienced in geomaterials subjected to pore fluid

chemistry cycles. Parallel model and iso-strain analysis can also predict the chemical-mechanical coupled soil response.

Table 4.1. NaCl solution salinity level.

Salinity Levels	
Deionized Water	<0.0001M
Fresh Water	< 0.008M
Cell 1	0.1M
Cell 2	0.2M
Saline Water	0.5M – 0.8M
Brine	> 0.8M
Cell 3	1.0M

Table 4.2. Kaolinite RP-2 soil properties.
(Palomino et al. 2008; Klein and Santamarina 2003; Jang and Santamarina 2015)

Kaolinite Properties RP-2	
Specific Gravity	2.6
GE Brightness, % Average	78
pH (28% solids), Average	5.2
Oil absorption, [g/100g] clay	40
minimum dispersed viscosity, 62% solids	4000+ cps
raw color	cream
specific surface, S_a [m^2/g]	21.9
d_{50} [µm]	0.36
thickness, nm	45
liquid limit, deionized water %	67
liquid limit, brine %	52
liquid limit, kerosene %	82

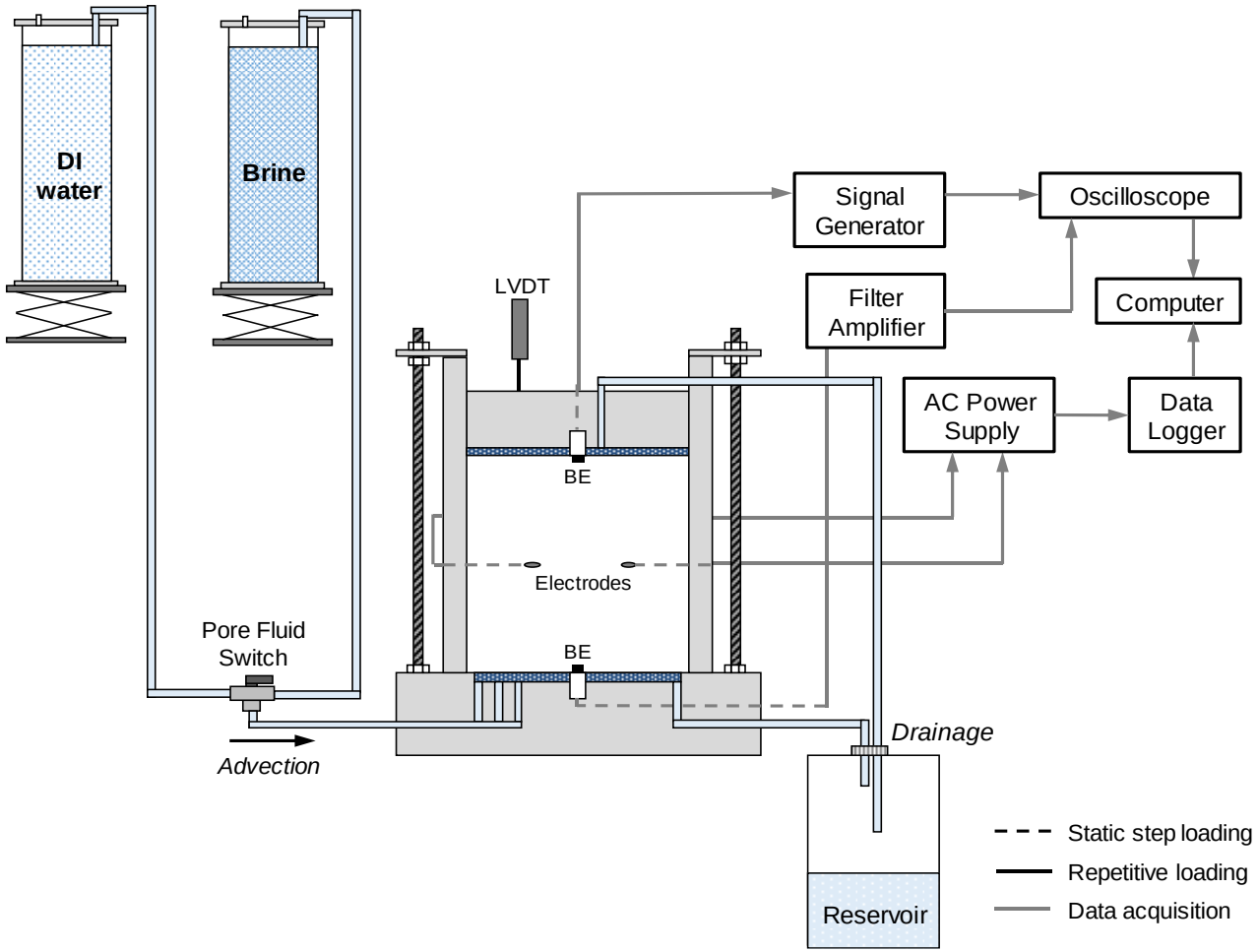

Figure 4.1. Device. Schematic diagram of the pore fluid circulation system used for static and repetitive loading. The loadings system conducts the experiment with two reservoirs gravitationally circulates deionized water and NaCl salt solutions into the specimens. The peripheral electronics installed in the modified oedometer are used to measure deformation, electrical conductivity, and shear waves. The oedometer cell consists of a fixed ring with electrodes, top and bottom caps with bender elements, and clamped LVDT. Top and bottom cap dimensions: 100mm diameter and 50mm height. Fixed ring dimensions: *ID* = 100.5mm, *OD* = 120.5mm, and 80mm height.

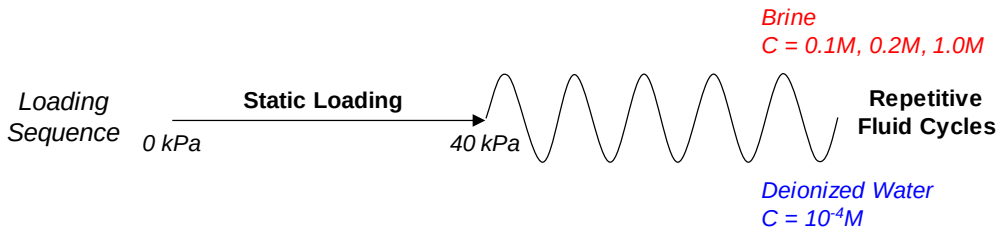

Figure 4.3. Static loading and repetitive fluid cycles test conditions.

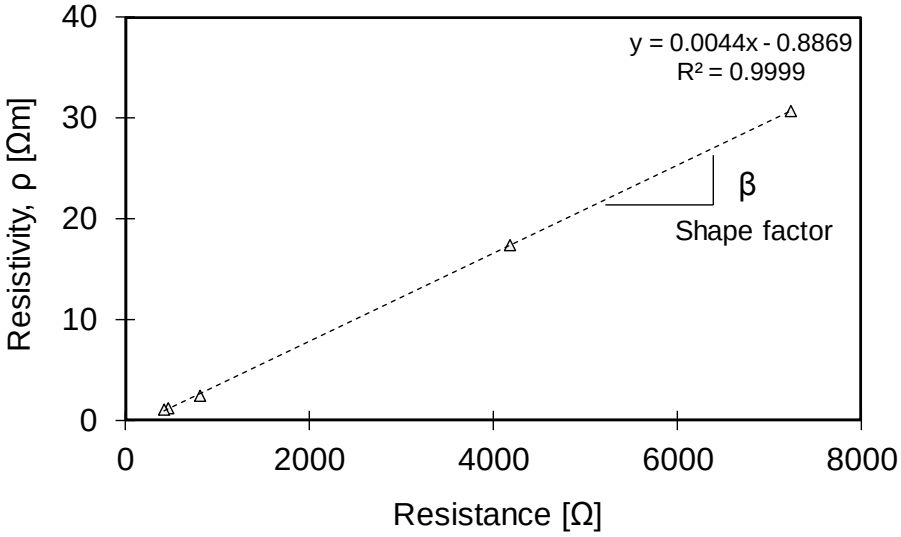

Figure 4.2. Resistivity calibration (shape factor β determination).

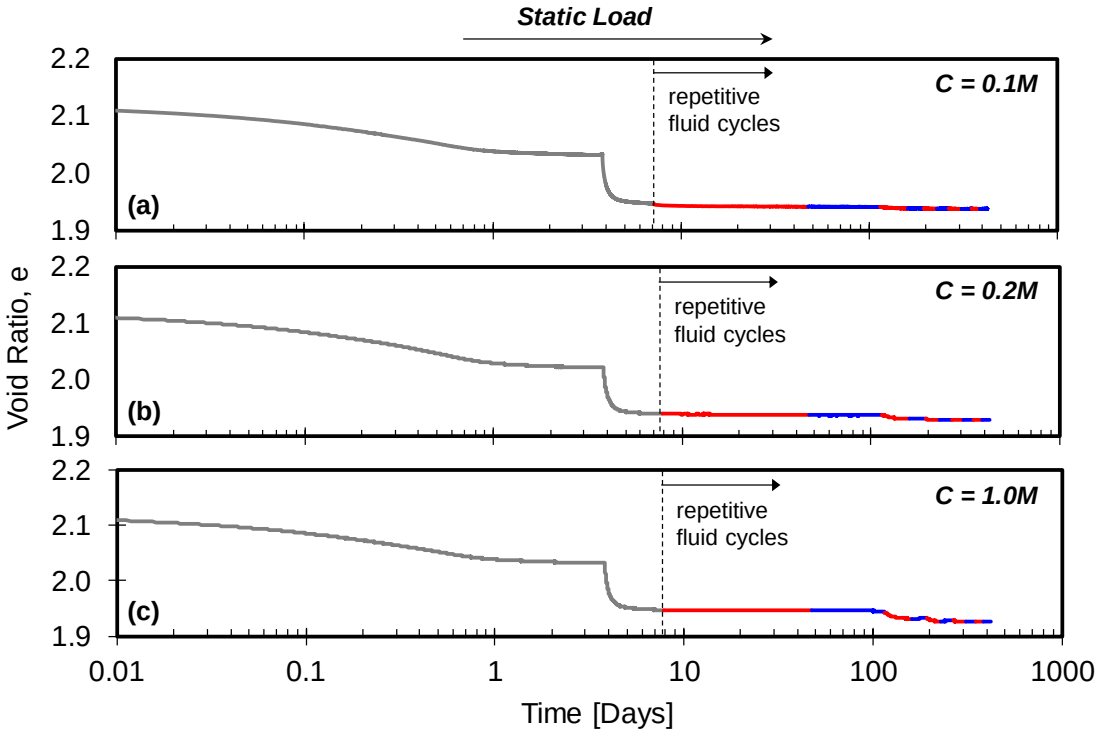

Figure 4.4. The change in void ratio during static loading and repetitive fluid cycles history. Test conditions: σ_0 = 40kPa. NaCl salt solution conditions: (a) C = 0.1M; (b) C = 0.2M; (c) C = 1.0M.

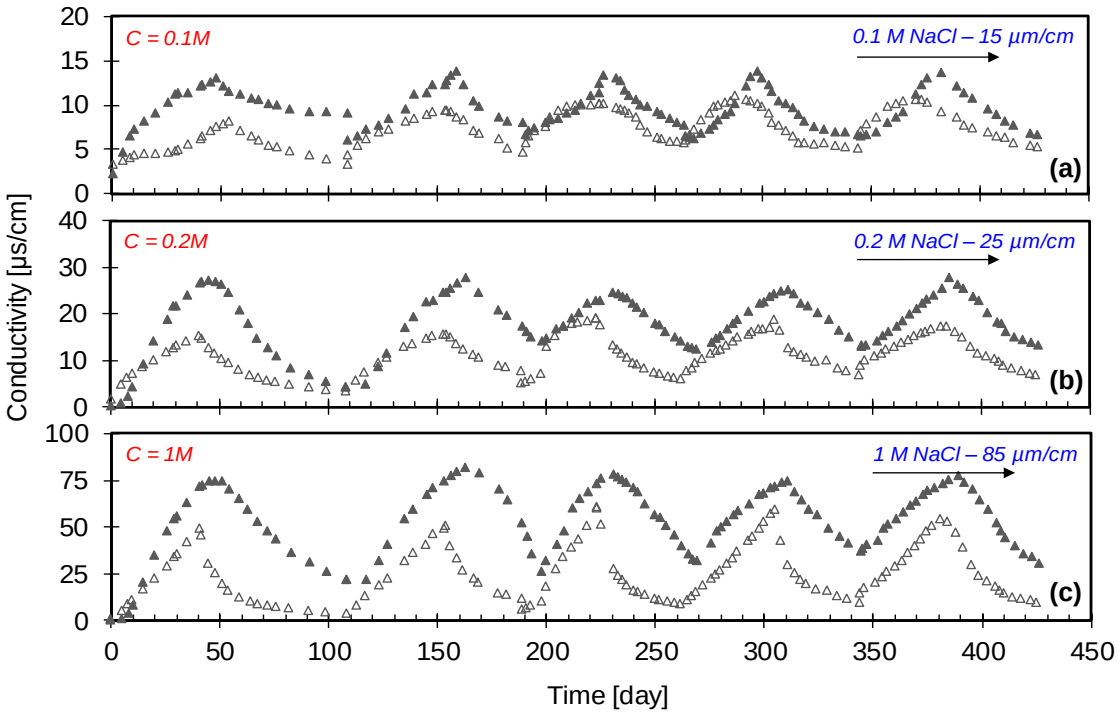

Figure 4.5. Evolution of electrical conductivities during repetitive loading history. Test conditions: σ_0 = 40kPa. NaCl salt solution conditions: (a) C = 0.1M; (b) C = 0.2M; (c) C = 1.0M.

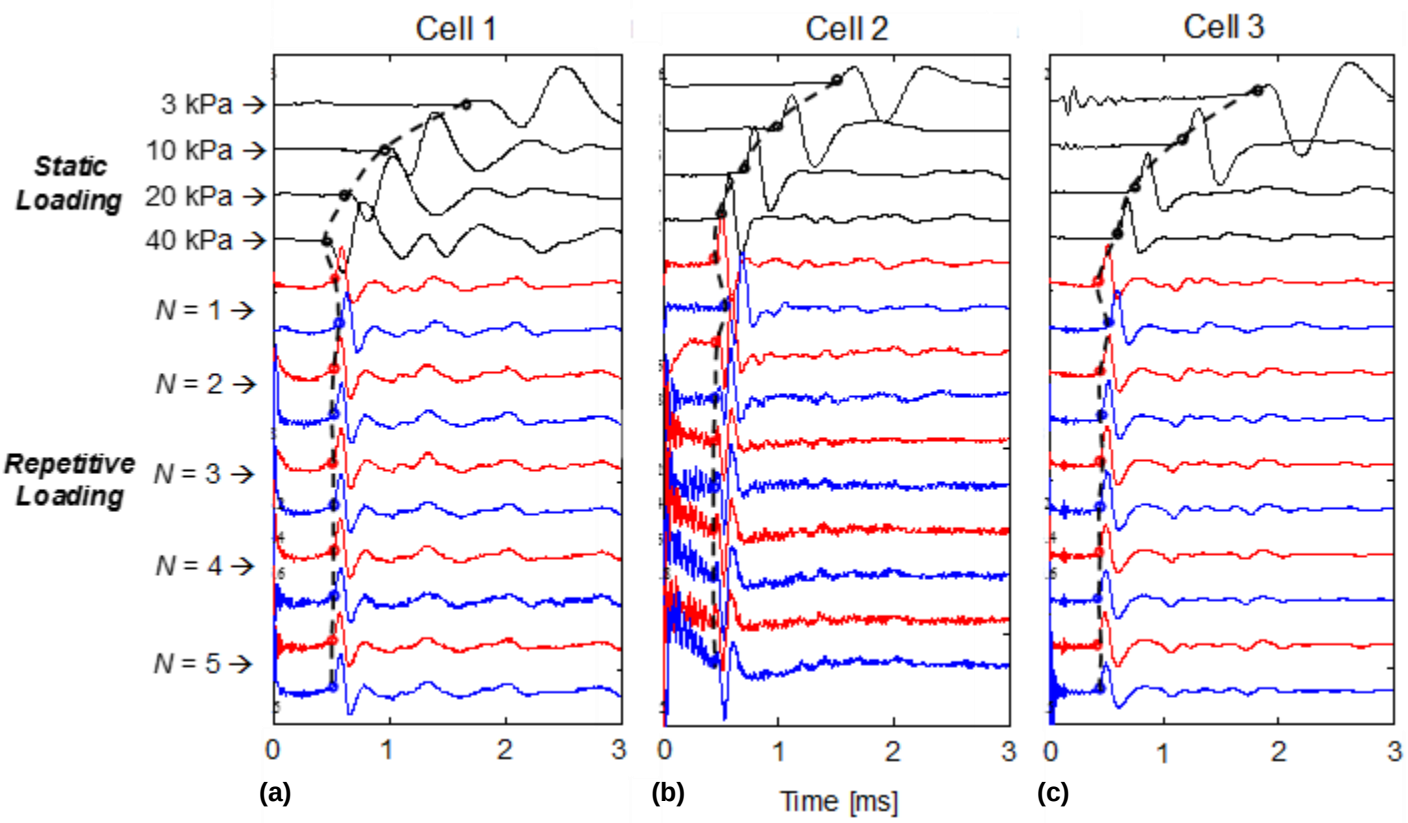

Figure 4.6. Cascades of shear wave signals captured during the static-repetitive loading history. Test conditions: σ_0 = 40kPa. NaCl salt solution conditions: (a) C = 0.1M; (b) C = 0.2M; (c) C = 1.0M.

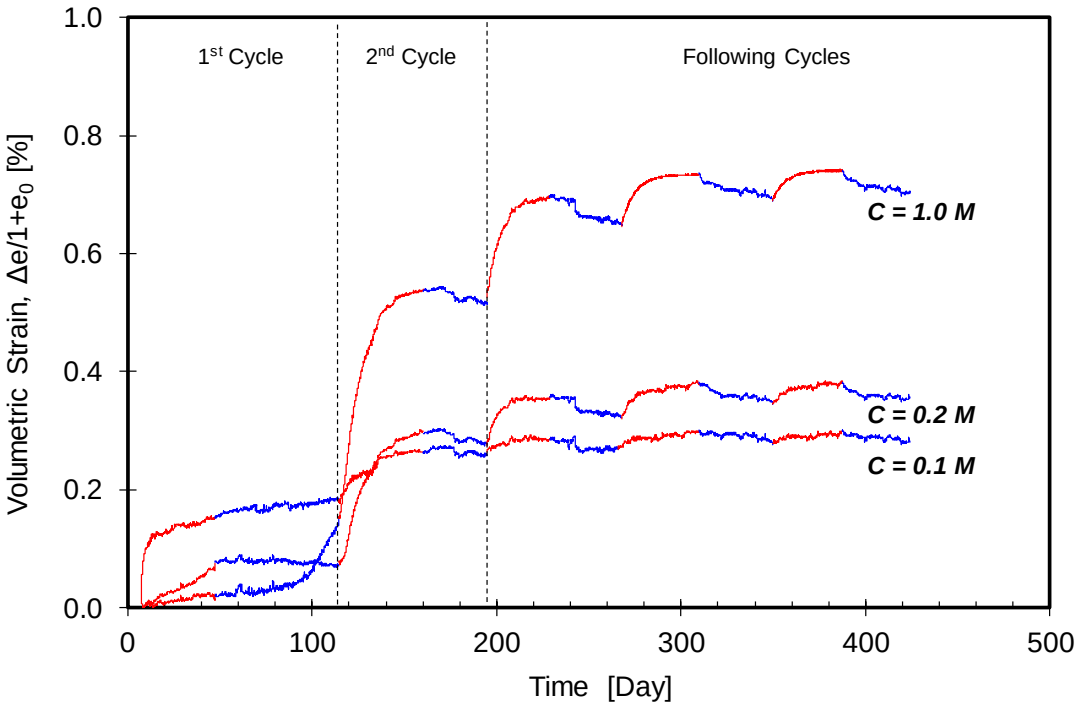

Figure 4.7. Changes in volumetric strains with time during repetitive loading history. Test conditions: σ_0 = 40kPa. NaCl salt solution conditions: (a) C = 0.1M; (b) C = 0.2M; (c) C = 1.0M.

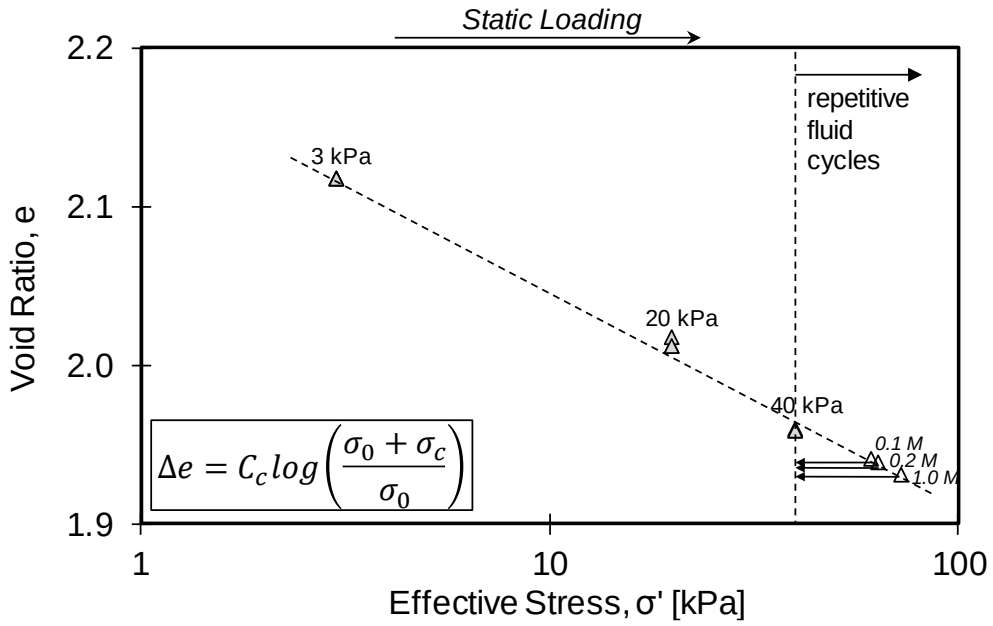

Figure 4.8. Change in void ratio with effective stress during static-repetitive loading history. Consolidation coefficient calculates the equivalent chemical-mechanical coupled effective stress. Test conditions: σ_0 = 40kPa. NaCl salt solution conditions: (a) C = 0.1M; (b) C = 0.2M; (c) C = 1.0M.

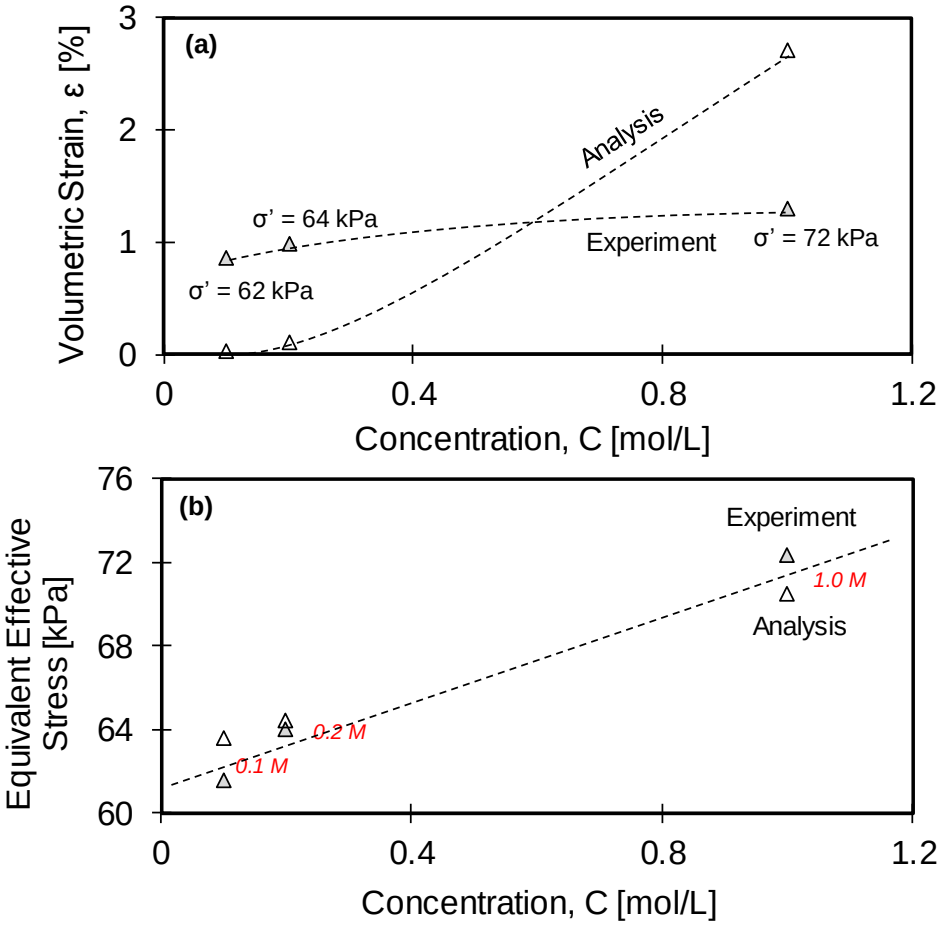

Figure 4.9. Analytical model predications versus experimental results. (a) inter-particle iso-strain analysis; (b) parallel effective stress model. Test conditions: σ_0 = 40kPa. NaCl salt solution conditions: (a) C = 0.1M; (b) C = 0.2M; (c) C = 1.0M.

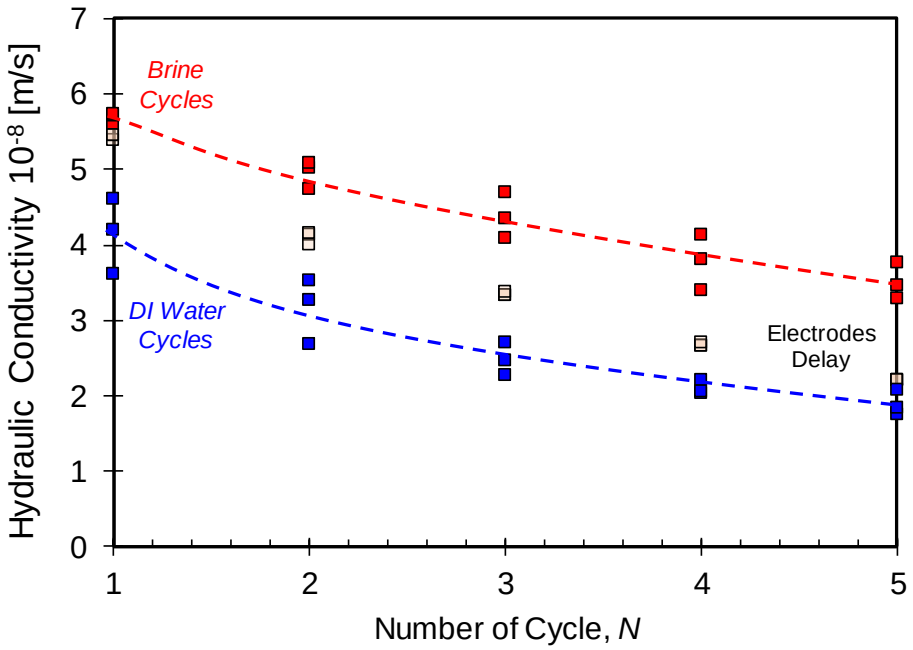

Figure 4.10. Evolution in hydraulic conductivity with number of cycles. Test conditions: σ_0 = 40kPa. NaCl salt solution conditions: (a) C = 0.1M; (b) C = 0.2M; (c) C = 1.0M.

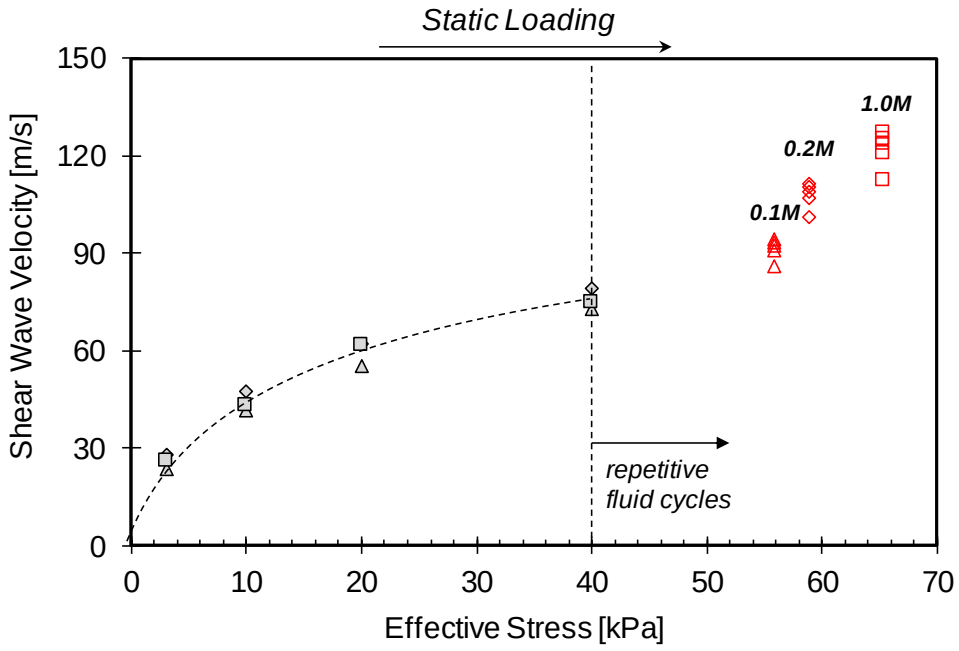

Figure 4.11. The evolution of shear wave velocity during static and repetitive loading stages - Particle contact and fabric change. Shear wave velocity versus stress in test conditions: σ_0 = 40kPa. NaCl salt solution conditions: (a) C = 0.1M; (b) C = 0.2M; (c) C = 1.0M.

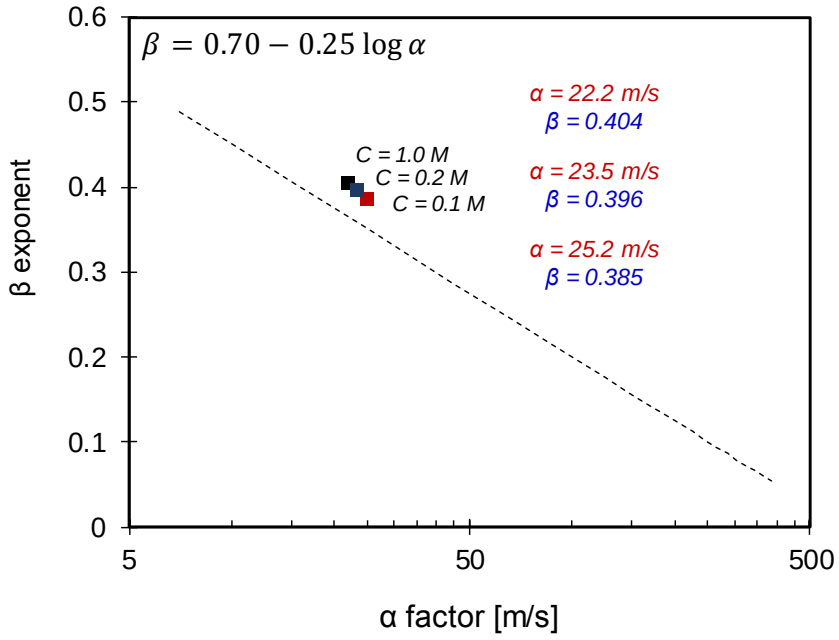

Figure 4.12. The α-factor and β-exponent before repetitive loading. Test conditions: σ_0 = 40kPa. NaCl salt solution conditions: (a) C = 0.1M; (b) C = 0.2M; (c) C = 1.0M.

CHAPTER 5. BAROMETRIC PRESSURE CYCLES

5.1 Introduction

Natural atmospheric pressure fluctuations associated with climatic changes transmit through the unsaturated subsurface (vadose zone). The atmospheric pressure at the surface and the soil gas pressure in the subsurface are different and result in damped and delayed pressure waves known as barometric pumping (SNRL, 2006). This process allows the permeable subsurface to breathe in response to pressure changes at the surface (Auer et al. 1996; DOE 2000).

Animal studies indicate that oscillatory flow reduces the total amount of available volume for ventilation (Slutsky et al. 1980). Both human medical research and geotechnical studies (in the form of gas transport in soils) continue to use this theory (Coghill et al., 1991). Experimental and theoretical work confirm the process of gas transport due to pressure fluctuations near the soil-atmospheric interface (Watson 1983; Joshi et al. 1983). These studies explore the oscillatory transport of heat, chemical vapors, and oxygen in the pore gas of soils (Kurzweg 1985; Scotter et al. 1967).

Barometric pressure cycles significantly accelerate the gas flow in the unsaturated zone (Baehr and Hult 1991; Shan at al. 1992; Shan 1995; Yeung et al. 2002), and consequently facilitate contaminant transport (Massmann and Farrier 1992; Auer et al. 1996). Field data presents enhanced exchange and distribution of various gases across the atmosphere-soil interface and within the vadose zone (Schery and Gaeddert 1982; Harries and Ritchie 1985). Cyclic atmospheric pressure cycles in the dual-porosity system are more

effective in gas transport compared with the single-porosity system (Nilson et al. 1991). The effective rate of diffusion in a porous medium increases due to the amount of gas oscillatory flow induced by barometric pumping pressure cycles.

This study applies barometric pressure cycles to accelerate the drying process in geomaterials. Experimental techniques use an NMR to monitor a closed chamber that contains desiccants, moist air, and unsaturated sand. Pressure cycles induced by a syringe pumping system enhance the pore water diffusion into the vapor phase and accelerates drying in unsaturated sands. We also propose a mathematical model which effectively predicts the evolution of pore water diffusion in unsaturated sands as a result of barometric pressure cycles.

5.2 Barometric Pumping Cycles

5.2.1 Mechanism of Airflow

The absolute pressure of the air phase governs the flow of pore air in unsaturated soil. The ideal gas law captures changes in the total air potential in pores. Pressure and temperature variations contribute to the prevailing air potential changes. The major mechanisms responsible for airflow in unsaturated soils include: 1) Daily, weekly, and seasonal barometric pressure and temperature variations (Stallman 1967; Stallman and Weeks, 1969; Weeks 1978, 1979); 2) Fluctuations in wind conditions (Weeks 1979); 3) Temperature gradients due to topographic relief (Ross et al. 1992); 4) Heat sources such as pyrite oxidation and radioactive materials (Lu and Zhang 1997).

5.2.2 Regimes for Pore Water and Pore Airflow

The flow of pore water in unsaturated soils (with the exception of the vapor phase) only occurs through the pore space occupied by a continuous liquid phase. By contrast, the flow of pore air requires the presence of a continuous gas phase. Water and air flow primarily depend on the soil type and the degree of saturation.

The three distinct pore flow regimes in unsaturated soils are air flow, water flow, and concurrent air and water flow. Each regime is delineated as a function of the water content and pore size by boundaries that establish a residual water content regime, an occluded-air-bubble water content regime, and a saturated water content regime. The magnitude of water content which separates each regime decreases with rises in pore size.

A series of disconnected menisci among soil particles contains the pore water in the air flow regime. The pore water content in this condition is less than or equal to the residual condition. There is no continuous liquid phase, and pore water diffusion occurs primarily by vapor transport mechanisms. On the other hand, the total air potential gradients drives the flow of pore air.

5.2.3 Steady Vapor Flow

The fundamental driving mechanism for vapor transport in unsaturated soil is the chemical potential of water vapor. Fick's first law captures a quantitative description of steady vapor flux q_v (de Vries 1958; Cass et al. 1984)

$$q_v = -D_v \nabla \rho_v \tag{5.1}$$

where D_v [m^2/s] is the diffusion coefficient for water vapor transport in unsaturated soil, and ρ_v [kg/m^3] is the vapor density or the absolute relative humidity of the pore water vapor.

Calculations of the vapor diffusion coefficient use the free air diffusion coefficient D_0 and the air-filled porosity n_a of the soil (Penman 1941):

$$D_v = \tau \eta n_a D_0 \tag{5.2}$$

Where the free air diffusion coefficient D_0 depends on both the temperature and pressure, and ranges from approximately 10^{-9} to 10^{-6} [m^2/s], τ is a dimensionless tortuosity factor and is typically 0.66 (Penman 1940), and η is an enhancement factor that varies from 3 at a low water content to 16 at saturation (Philip and de Vries 1957; Cass et al. 1984).

Gradients in temperature and vapor pressure are the two major driving mechanisms for vapor transport in unsaturated soils. Vapor transport often becomes the primary mechanism for pore water transport in relatively dry unsaturated soils. Temperature and vapor pressure can vary significantly in time or space within the atmosphere and to a significant depth in the subsurface. Natural variations in vapor pressure occur in similar daily and seasonal cycles. The ideal gas law can quantitatively assess the impact of these changes in temperature and vapor pressure on the corresponding vapor density:

$$\rho_v = \frac{\omega_w}{RT} u_v \tag{5.3}$$

The empirical equation below predicts the dependence of vapor pressure on temperature (Teten 1930). This relates vapor pressure to temperature T, saturated vapor pressure uv,sat, and relative humidity RH,

$$u_v = u_{v,sat} RH = 0.611 \exp\left(17.27 \frac{T - 273.2}{T - 36}\right) RH \tag{5.4}$$

In addition, the equation below provides the vapor density gradient which results from both the temperature and vapor pressure gradients,

$$\nabla \rho_v = \frac{\omega_w u_{v,sat}}{RT} \nabla RH - \frac{\omega_w RH}{R} \left(u_{v,sat} \frac{\nabla T}{T^2} - \frac{\nabla u_{v,sat}}{T} \right) \tag{5.5}$$

The diffusive vapor flux can be derived as,

$$q_v = -D_v \rho_{v,sat} \left(\frac{\nabla RH}{RH} - \frac{\nabla T}{T} + \frac{\lambda \omega_w \nabla T}{RT^2} \right) \tag{5.6}$$

where λ is the latent heat of water vaportization. Vapor flows from relatively high to low humidity and temperatures. Low temperatures cause air contraction, and result in a higher vapor density; whereas high temperatures cause air expansion, and lead to a low vapor density.

5.2.4 Oscillatory Transport

Dynamic mechanical stress during walking initiates fluid flow in bone, which results in external mechanical signals to bone cells and enhances in cellular metabolism. The local solute displacement due to convection is three orders of magnitude larger than the diffusion which occurs during the same period and depends on the size of the solute (Wang et al. 2000).

Accelerated solute transport in soil adapts the cyclic phenomena observed in bones. Cyclic flow with zero time-average velocity takes place in porous networks subjected to

periodic excitation. The porous network in a geomaterial microstructure consists of pores interconnected by channels. This geometry and non-uniform flow condition cause a relatively high rate of mixing within pores (Goldsztein and Santamarina 2004). Consequently, solute transportation occurs at a much faster rate than diffusion despite the fact that effective advection is null in cyclic flow (Claria et al. 2010).

Nature also induces similar oscillations on near surface unsaturated soils. An analysis of gas penetration into the vadose zone due to changes in atmospheric pressure (Buckingham 1904) concludes that one-dimensional transport governs the depth of penetration. Atmospheric pumping influences both the subsurface gas distribution and flow across the atmosphere-soil interface (Clements and Wilkening, 1974).

5.2.5 Mathematical Development

Pressure variations due to barometric pumping at the water table boundary are the major components of both gas flow and contaminant transport models in the vadose zone (Baehr and Hult 1991; Shan at al. 1992; Shan 1995; Yeung et al. 2002; Massmann and Farrier 1992; Auer et al. 1996). Simple Fourier components in the form of equations can capture these fluctuations in gas pressure without the complexity of real atmospheric pressure patterns (Auer, 1996). The sinusoidal atmospheric pressure pattern can also help to predict the effects of atmospheric pressure on gas transport in the vadose zone (Massmann and Farrier 1992; Choi et al. 2005). Linear equations can analyze the atmospheric pressure fluctuations as these variations are much smaller than the average pressure (Fukuda, 1955; Auer et al., 1996; Neeper, 2002; Massman, 2006). The one-

dimensional propagation of small gas pressure variations in a porous medium is described by the diffusion equation of pressure:

$$\frac{\partial P}{\partial t} = D_a \frac{\partial^2 P}{\partial z^2} \tag{5.7}$$

where P is the mean pressure [kPa], D_a is the diffusion coefficient [m^2/s].

Soil vapor extraction and bio-venting studies frequently use both analytical and numerical groundwater flow models to simulate gas flow. These models provide useful approximations of gas flow under certain circumstances. Most studies investigate aspects of sub-surface migration of hydrocarbon contamination in the unsaturated zone (Sleep and Sykes, 1989), e.g. the removal of contaminants by vapor extraction (Baehr et al., 1989; Rathfelder et al., 1991; Mohr and Merz, 1995). Atmospheric pressure fluctuations can cause a horizontal flow of atmospheric air in an unsaturated zone connected to the atmosphere.

5.2.6 Dynamics of Near-Surface Zone Evaporative Drying in Soil

The importance of evaporation from the soil can hardly be overemphasized when one considers the vast arid regions on earth. Atmospheric conditions primarily control the rate of evaporation provided that the soil surface is moist (Wiegand and Taylor 1961; Covey 1965). The evaporation rate sharply decreases and does not relate to atmospheric conditions as soon as the surface is dry.

Evaporation from soil involves an intricate soil matrix which consists of an air-dry layer and a capillary rise layer. Vapor diffusion controls the evaporation in the air-dry layer

below the surface with both the capillary rise and vapor diffusion processes contributing towards evaporation at the capillary rise layer (Or et al. 2013). The thickness of the air-dry layer does not monotonically increase. Water vapor moves up to the soil surface and redistributes into a new equilibrium. This process results in a distinct diurnal pattern due to the presence of hysteresis in the evaporation process (Jackson 1973; Jackson et al. 1973; Idso et al. 1979). Field observations indicate that the majority of evaporation takes place near the top of the capillary rise zone with a small amount below the soil surface (Heitman et al. 2008; Yamanaka et al. 1998).

Theoretical studies evaluate the role of vapor transport (Philip and deVries 1957) and hysteresis in evaporation (Milly 1984a, 1984b). These studies conclude that vapor transport has a minimal effect on evaporation from soils. The capillary rise process induces liquid water flow and is rate-limited in soil evaporation (Saravanapavan and Salvucci 2000). The water flow from the capillary rise layer controls the dynamics in the air-dry layer. Therefore, the flux towards the soil surface is insensitive to the water vapor diffusivity. The transfer in the air-dry layer is significantly larger and less resistive than the diffusion expected from theoretical studies (Cahill and Parlange 1998; Parlange et al. 1998). Atmospheric turbulence greatly enhances water transport in soils (Scotter and Raats 1969; Kimball and Lemon 1971). This effectively increases the molecular vapor diffusivity in the vadose zone. Thermal gradients due to radiation at the soil surface can also influence daily fluxes (Fritton et al. 1970; Hanks et al. 1967; Milly 1984a, 1984b)

5.3 Experimental Study: Devices and Test Procedure

This experimental program explores accelerated water transport from a nearly saturated boundary (*RH* = 100%) to a completely dry boundary (*RH* = 0%) induced by pressure cycles in a closed system. The repetitive pressure loading system consists of a peristaltic pump, glass syringe, precision pressure transducer, and an NMR testing tube (*ID* = 106mm, 10mm wall thickness, and 100mm high) which contains the unsaturated sand specimens and desiccants (Figure 5.1).

5.3.1 Flow Rate-Controlled Repetitive Pressure Loading System

The loading system consists of a modified peristaltic pump, glass syringe, and a steel lever that connects between the spinning panel of the pump and the glass syringe.

5.3.2 Pressure Oscillation Monitoring

The precision pressure transducer mounted between the syringe and the NMR testing tube continuously records the pressure oscillations inside the closed system during the experiment. A standard DC voltage supply (Keysight E3630A, Figure 5.1) powers the precision pressure transducer. A data logger (Keysight 34970A, Figure 5.1) saves the pressure transducer readings.

5.3.3 Low-Frequency NMR

A 12MHz NMR spectrometer (GeoSpec, Oxford Instruments) measures the moisture content in soil specimens. The signal intensity is proportional to the moisture content. The magnetic gradient enables the calculation of the moisture content at a specified depth. The

Carr-Purcell-Meiboom-Gill (CPMG) echo sequence records the transverse signal relaxation.

5.3.4 Specimen Preparation

This experimental study uses Jeddah sand (particle size = 0.42mm – 0.71mm). Sand particles were prepared with deionized water (w = 10%) in an unsaturated state. The bottom section of the NMR test tube contains well-mixed sand specimens due to the fixed effective electromagnetic detection range (approximately 7cm). We punched holes through a sealed plastic bag that contains desiccants (Drierite, adsorption rate ~ 10%) as the drying agent in the closed system (RH = 0%, Figure 5.2). Pressure cycles flow dry air into the unsaturated sand specimens and adsorb the moist air through these desiccants.

5.3.5 Test Procedure

The repetitive pressure loading procedure consists of a wide range of flow rates induced by a peristaltic pump. Each flow rate corresponds to a specific frequency that the pressure cycle applies to the closed system. The loading procedure consists of three stages: (1) Cyclic pressure pumping, (2) NMR scanning, (3) Pause (Figure 5.2). Each testing frequency rate (f = 0.1Hz, 0.25Hz, 0.5Hz, 1Hz, 2Hz, 3Hz, 4Hz, and 5Hz) applies the same loading procedure with a different testing period (t = 1h, 2h, 6h, 12h, and 24h). During each loading procedure, two NMR scans compare the differences between the reference and pressure cycles saturation profiles in the same experimental period. Experimental results discuss several representative datasets with selected frequency range. Large number of parallel experiments with different testing periods conducted under each selected frequency support the consistency of the results.

5.4 Experimental Results

Repetitive pressure loading cycles accelerate the water diffusion and vapor exchange process in the drying process of geomaterials. The drying efficiency in the closed system has an inverse relationship with the test frequency. Saturated profiles during the pressure loading cycles determine the homogenized drying process in the sand specimens. The pressure oscillation history confirms the pressure consistency of the closed system. This section presents detailed experimental results for the Jeddah sand subjected to a series of frequencies and testing periods.

5.4.1 NMR Saturation Profile Evolution

Figure 5.3 presents the saturation profile history calculated from NMR scans. Each curve consists of pointed calculation per mm of the unsaturated Jeddah sand specimens. Capillary force brings water that initially placed at the bottom of the sand specimen to the top and distribute it within the pores. Consequently, there is less moisture content at the top of the sand specimen and the moisture content gradually increases with depth. The 24h time interval between each NMR scanning curve ensures that consistency of moisture content calculation inside the closed system. Parallel aligned scanning curves indicate that the drying process takes place homogeneously within the unsaturated sand specimen. This further confirms validity of the mathematical model in the analysis section.

5.4.2 Water Loss Due to Cycles vs. Frequency

Figure 5.4 presents the water loss due to pressure cycles with a wide range of tested frequencies. (a) Total water loss in time interval of 1h. Two NMR scans (one reference;

one with pressure cycles) generate one point of the water loss measurement. Each point requires a new test inside the closed cell with identical experimental parameters and compositions to ensure the exact same initial conditions. Effective range of flow rates generated from the peristaltic pump enables a wide selection of frequencies in experiments (ΔP = 3kPa, f = 0.1 Hz ~ 4.5 Hz). Total water loss per 1h time interval from the unsaturated Jeddah sand specimen gradually increases with the rise in tested frequency. (b) Water loss per cycle analysis. Tested frequency with fixed time interval allows the calculation of number of pressure cycles experienced inside the sand specimens. Total water loss divided by cycle numbers can calculate the water loss in each individual pressure cycle with different tested frequencies. On the contrary to the trend presented in Figure 5.4a, the water loss per cycle decreases with the rise in frequency.

5.5 Analysis and Discussion

5.5.1 Pressurization Model Formulation

The closed cylindrical test tube contains the unsaturated sand specimen placed at the bottom as shown in Figure 5.1. The hanging desiccants above the sand specimens generate a dry boundary for the air flow exchange between the moist pore air and the dry air in the area above the sand specimen. Dry air has a relative humidity of RH_{dry} and the sand specimen has a relative humidity of RH_{soil}.

The unsaturated sand specimen consists of a solid phase V_s, a pore water phase V_w and a pore air phase V_a. The total volume of the sand specimen V_{soil} is the volume summation of these three individual components. The volume of the voids V_v is the volume summation of the pore water phase and pore air phase.

$$V_{soil} = V_s + V_w + V_a \tag{5.8}$$

$$V_v = V_w + V_a \tag{5.9}$$

The pore air phase and the dry air phase follows the ideal gas law. The pressure variation induced by pressure cycles promotes the air exchange between the pore air and dry air above the unsaturated sand specimen.

$$\Delta P = P_H - P_0 \tag{5.10}$$

$$V_{inv} = \delta V = V_a \left(1 - \frac{P_0}{P_H} \right) \tag{5.11}$$

Where P_{H} is the higher pressure when the closed system is pressurized due to the presence of pumping, P_0 is the atmospheric pressure when the closed system is at a static state. The air volume which invades into the pore space V_{inv} equals the volume change induced by the pressurization of the system δV. The equation below generalizes the pore volume that invades into the sand specimen under pressure cycles,

$$V_{inv}^i = V_a^i \left(1 - \frac{P_0}{P_H} \right) = \left(V_v^i - V_w^i \right) \left(1 - \frac{P_0}{P_H} \right) \tag{5.12}$$

Let's assume that the closed system instantaneously exchanges dry air with moist pore air. The pore water that remains in the soil specimen simultaneously homogenizes with the dry air which invades into the pores. The water that diffuses into the water vapor equals the water loss from the sand specimen. Therefore, the mass conservation in the closed system is:

$$\left(V_w^{i-1} - V_w^i\right)\rho_w = V_{inv}^i \rho_{sat}\left(RH_{soil} - RH_{dry}\right) \tag{5.13}$$

$$\frac{dV_w}{dN} = \frac{\rho_{sat}\left(RH_{soil} - RH_{dry}\right)\left(V_v^i - V_w^i\right)\left(1 - \frac{P_0}{P_H}\right)}{\rho_w} \tag{5.14}$$

$$\frac{dV_w}{dN} + \left(1 - \frac{P_0}{P_H}\right)\frac{\rho_{sat}\left(RH_{soil} - RH_{dry}\right)}{\rho_w}V_w^i - \left(1 - \frac{P_0}{P_H}\right)\frac{\rho_{sat}\left(RH_{soil} - RH_{dry}\right)}{\rho_w}V_v^i = 0 \tag{5.15}$$

$$V_w^i = Ce^{\left(1-\frac{P_0}{P_H}\right)\frac{\rho_{sat}\left(RH_{soil}-RH_{dry}\right)}{\rho_w}i} + V_v^i \tag{5.16}$$

5.5.2 Contacting Sphere Model

Sand is a system of spherical particles arranged in various packing geometries. The relationship between the matric suction $u_a - u_w$, surface tension T_s, and two radii r_1 and r_2 describes the geometry of the water menisci between two spherical particles. The Laplace capillary equation captures the matric suction within the particles that have an identical radius R,

$$u_a - u_w = T_s\left(\frac{1}{r_1} - \frac{1}{r_2}\right) \tag{5.17}$$

The filling angle θ describes the changes in the size, geometry, and volume of the water lens. Figure x shows the geometric relationship between small radii r_1 and r_2, radius R with the filling angle θ. The equations below present the mathematical formulation,

$$r_1 = R\left(\frac{1}{\cos\theta} - 1\right) \tag{5.18}$$

$$r_2 = R\tan\theta - r_1 \tag{5.19}$$

$$u_a - u_w = \frac{T_s}{R}\frac{\cos\theta\left(\sin\theta + 2\cos\theta - 2\right)}{R\left(1-\cos\theta\right)\left(\sin\theta + \cos\theta - 1\right)} \tag{5.20}$$

Equation 5.21 provides an estimate of the water lens volume V_l in one orthogonal plane for spherical particles coordinated in a simple cubic packing order:

$$V_l = 2\pi R^3\left(\frac{1}{\cos\theta} - 1\right)^2\left[1 - \left(\frac{\pi}{2} - \theta\right)\tan\theta\right] \tag{5.21}$$

$$V_s = \frac{4}{3}\pi R^3 \tag{5.22}$$

The number of water lenses both among one spherical particle and all adjacent particles in a cubical unit volume with a simple cubic packing order is three. The equation below expresses the gravimetric water content w for a unit volume in three orthogonal planes:

$$w = \frac{3V_l\rho_w}{V_s\rho_s} = \frac{3V_l}{V_sG_s} \tag{5.23}$$

$$w = \frac{9}{2G_s}\left(\frac{1}{\cos\theta} - 1\right)^2\left[1 - \left(\frac{\pi}{2} - \theta\right)\tan\theta\right] \tag{5.24}$$

Figure 5.5a presents the relationship between the matric suction ranges in the Jeddah sand specimen with the gravimetric water content,

$$\psi = -\frac{\rho_w RT}{M_w}\ln\left(\frac{RH\%}{100}\right) \tag{5.25}$$

$$RH = e^{-\frac{\psi M_w}{\rho_w RT}} \times 100\% \tag{5.26}$$

Figure 5.5b presents the relative humidity for the sand specimen and includes the full range of matric suctions from different gravimetric water contents. Therefore, RH_{soil} is nearly 100%.

5.5.3 Accelerated Water Transport Induced by Pressure Cycles

Water mass loss ML_{total} from the sand specimen in the closed system during drying has two separate components. The static component of water mass loss $ML_{\Delta P=0}$ describes the evaporative diffusion of the water from the unsaturated sand specimen into the water vapor in dry air. The pressurized component of water mass loss ML_{pres} illustrates the accelerated water transport induced by pressure cycles presented in the pressurization model.

$$ML_{total} = ML_{\Delta P=0} + ML_{pres} \tag{5.27}$$

$$ML_{\Delta P=0}(t) = S_e \cdot t \tag{5.28}$$

$$ML_{pres}(N, \varepsilon) = \left(V_w^0 - V_w^i\right) \varepsilon \rho_w \tag{5.29}$$

where S_e is the evaporative-diffusion rate at the static state in the closed system measured from the NMR experiments. This also represents the static component of water mass loss from the sand specimen during the drying process. The frequency-dependent efficiency ε describes the efficiency of the cyclic pressurized system and is the ratio of the experimental

results compared with the instantaneous homogenized pressurized model. Both parts of the water mass loss are a function of experimental period *t*.

$$ML_{total} = WL_{\Delta P=0}(t) + WL_{pres}(N \cdot f) \tag{5.30}$$

$$ML_{total}(t) = S_e \cdot t + \int_0^N \left(V_v^i - V_w^i\right)\left(1 - \frac{P_0}{P_H}\right)\varepsilon\rho_{sat}\left(RH_{soil} - RH_{dry}\right) \tag{5.31}$$

5.5.4 Model Prediction vs. Experimental Results

Figure 5.6 presents the comparison between model prediction and experimental results of the total water loss in 1h with number of cycles. Table 5.1 summarizes the unsaturated Jeddah sand specimen properties and test parameters adapted into the mathematical model. Contour lines indicate the model prediction of total water loss in 1h with corresponding number of cycles in different drying efficiency regimes (ε = 10%, 25%, 50%, and 100%/cycle). Experimental results fall into the contour line regimes and represent the water loss efficiency with number of pressure cycles. The comparison between model prediction and the dataset provides the similar trend observed in the water loss per individual cycle with frequency. The fewer number of pressure cycles within a fixed time interval lead to a higher water loss efficiency inside the closed system.

5.5.5 Frequency Dependent Efficiency

Figure 5.7 presents the frequency dependent water loss efficiency per cycle with tested frequency range (f = 0.1Hz ~ 4.5Hz). Analysis of model prediction with experimental results determines a frequency dependent water loss efficiency of unsaturated Jeddah sand specimen subjected to pressure cycles. The water loss efficiency gradually

decreases with the rise in frequency. The efficiency reaches close to 100% with the tested frequency of 0.1Hz. By contrast, the efficiency reduces to less than 20% with the tested frequency of 4.5Hz. High frequency pressure cycles induce low water loss efficiency due to insufficient water transport from the liquid phase to vapor phase. Consequently, high frequency pressure cycles produce insufficient exchange between the dry air from desiccants and the pore moist air. Low frequency pressure cycles enable a more effective homogenization within the closed system and significantly increases the water loss efficiency.

5.6 Conclusions

- NMR is an advanced non-invasive and non-disturbing technique to measure soil water content. The NMR technique provides precision readings to 10^{-4} order of magnitude and can capture variation in depth with saturation profile analysis.

- Soil water content in unsaturated Jeddah sand specimen forms an uneven distribution due to sample preparation method. Capillary rise brings the water from bottom of the specimen to the top and results in a gradient ($w_{top} < w_{bottom}$, water content gradually increases from the top to a characteristic depth and remains constant).

- Atmospheric pressure cycles effectively accelerate the soil water transport inside the closed NMR cell. Experimental results illustrate water loss increment due to pressure cycles is in proportion to test period and frequency changes.

- Mathematical model can capture both the static component of water mass loss $ML_{\Delta P=0}$ due to evaporative diffusion and the accelerated component of water mass loss ML_{pres} induced by pressure cycles presented in the pressurization model.

- Frequency dependent efficiency determines the water loss acceleration of the unsaturated sand specimen inside the closed cell. High frequency pressure cycles lead to low drying efficiency due to insufficient air exchange and vapor diffusion. Characteristic low frequency significantly promotes mixing and homogenization which maximize the water loss acceleration as a result of pressure cycles.

Table 5.1. Unsaturated Jeddah sand specimen properties and test condition parameters.

Tested Specimen Parameters	
Atmospheric Pressure, P_0 [kPa]	*101.3*
High Pressure, P_H [kPa]	*104.3*
Sand Solid Volume, V_s [cm^3]	*11.3*
Sand Air Volume, V_a [cm^3]	*7.8*
Sand Water Volume, V_w [cm^3]	*3.5*
Water Density, ρ_w [kg/m^3]	*1000*
Water Content, θ [%]	*10*
Vapor Density, ρ_d [g/m^3]	*22.99*

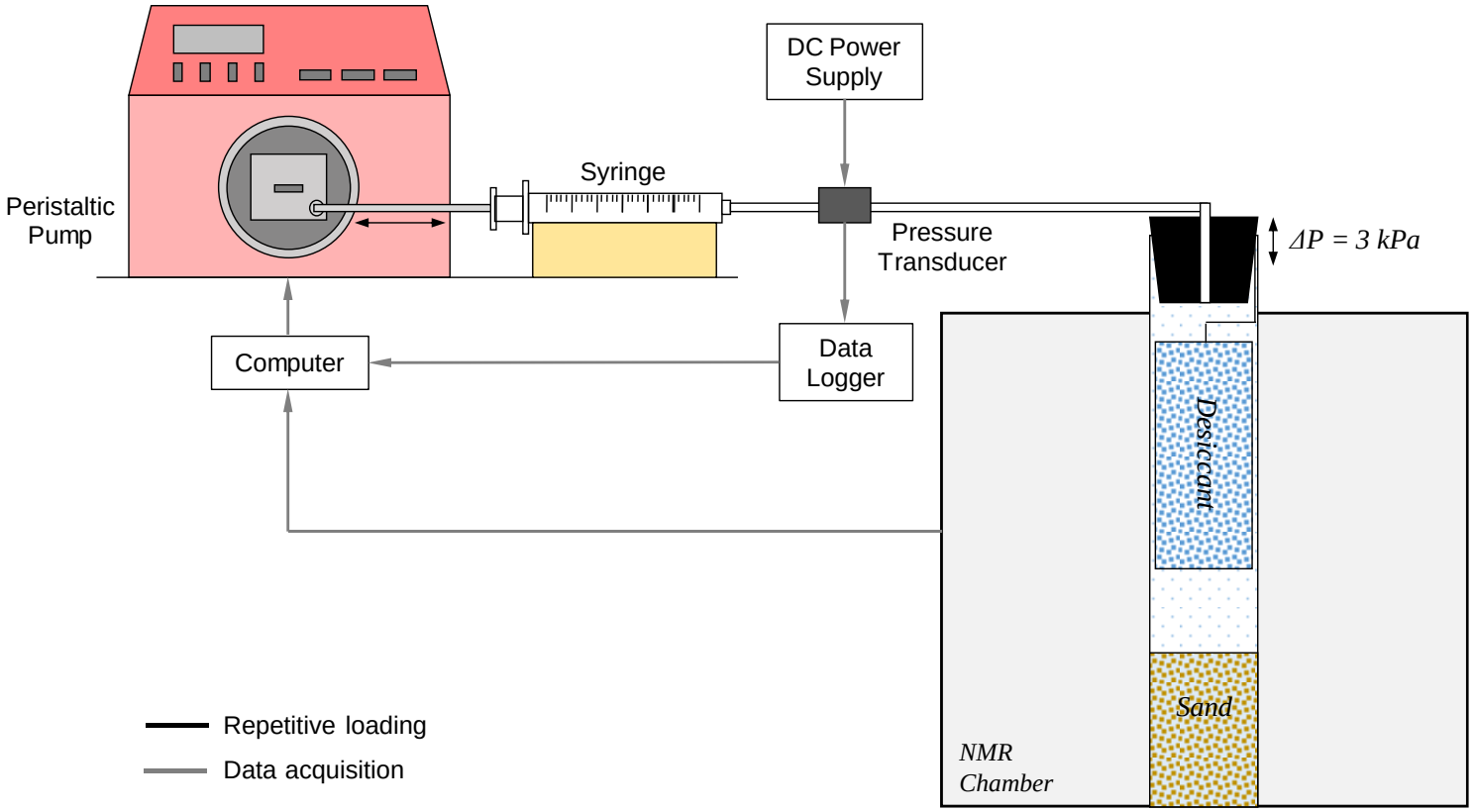

Figure 5.1. Device. Schematic diagram of the cyclic pressure system. The loadings system conducts the experiment inside an NMR which continuously scans and measures the moisture content inside the sand specimens. The precision pressure transducer records the pressure oscillation inside the closed cell. The cyclic pressure system contains a peristaltic pump that connects with a glass syringe (V = 10mL). A rubber top with an inlet (d = 1/8") seals the closed cell. The cell consists of a floating ring with bender elements and electrodes and top and bottom caps with a thermocouple. The closed cell dimensions: 25mm diameter and 250mm height. Effective NMR detection range: 70mm from the cell bottom.

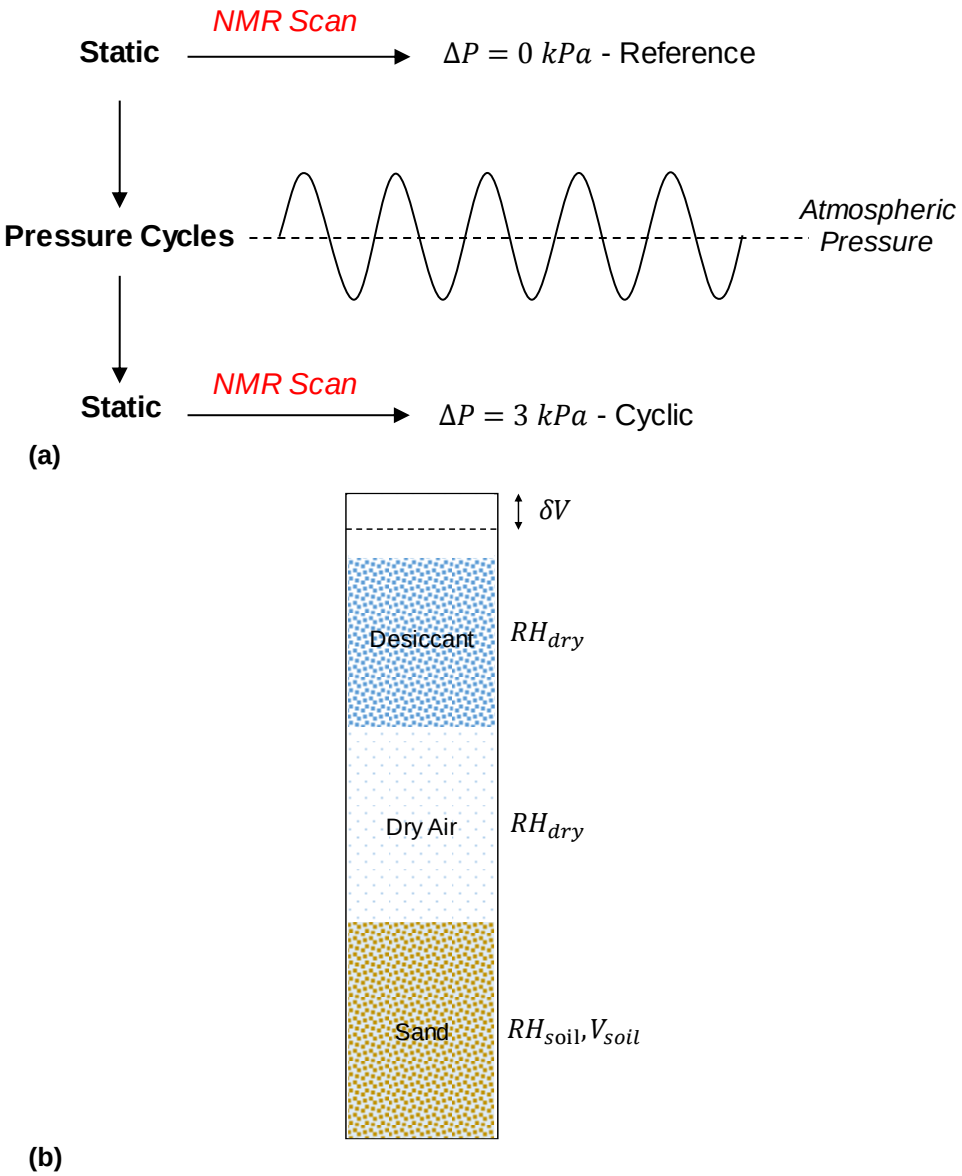

Figure 5.2. Test conditions and closed cell compositions. (a) Pressure cycle loading sequence with NMR scans; (b) Sketch of components inside the closed cell: desiccant, dry air, and unsaturated Jeddah sand specimen.

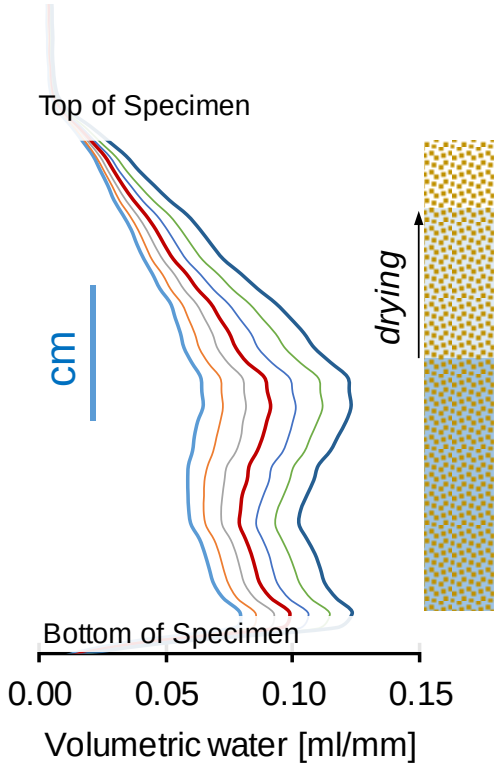

Figure 5.3. Changes in saturation profiles of the Jeddah unsaturated sand specimens with time interval of 24h. Test conditions: ΔP = 3kPa. Frequency f = 0.1 Hz ~ 4.5 Hz.

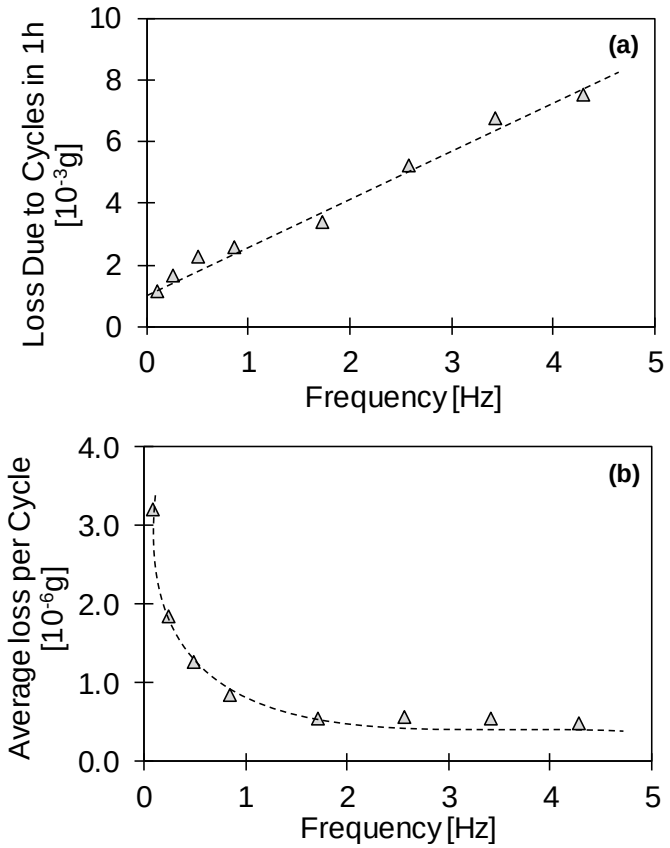

Figure 5.4. Water loss due to pressure cycles. (a) Total water loss in time interval of 1h with tested frequency range; (b) Water loss per cycle with tested frequency range. Test conditions: ΔP = 3kPa. Frequency f = 0.1 Hz ~ 4.5 Hz.

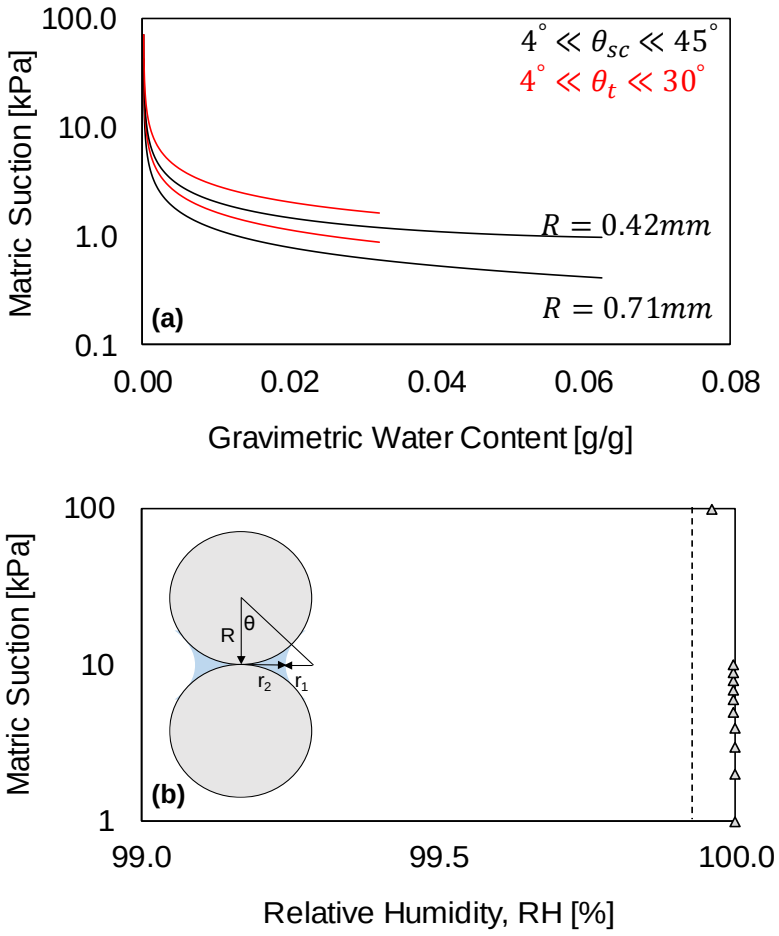

Figure 5.5. Contacting sphere model analysis. (a) Matric suction range with corresponding gravimetric water contents in Jeddah sand specimen; (b) Relative humidity with the matric suction in Jeddah sand specimen.

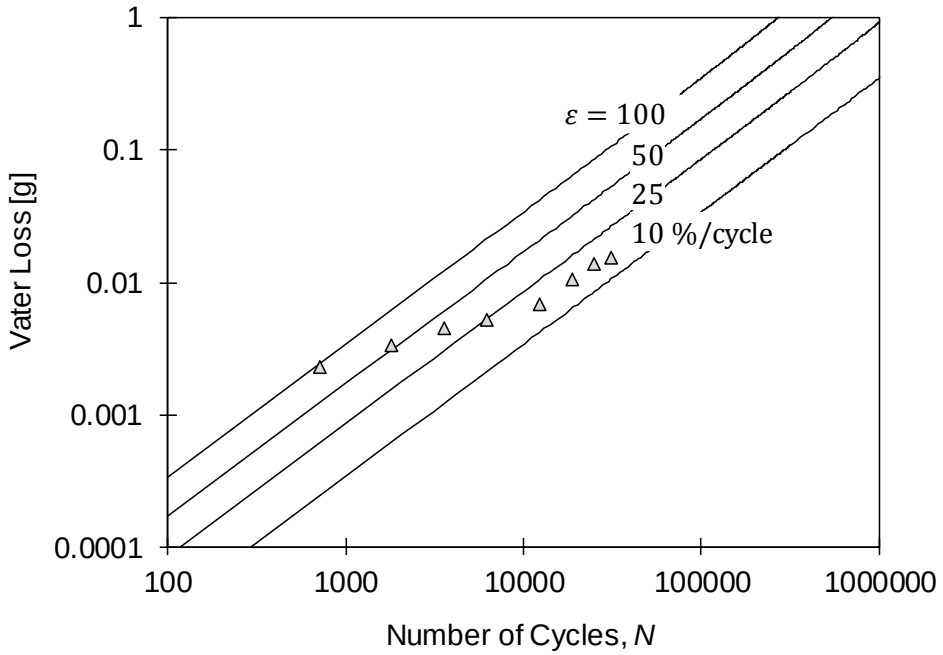

Figure 5.6. Total water loss in 1h with number of cycles, model prediction versus experimental results. Test conditions: ΔP = 3kPa. Frequency f = 0.1 Hz ~ 4.5 Hz.

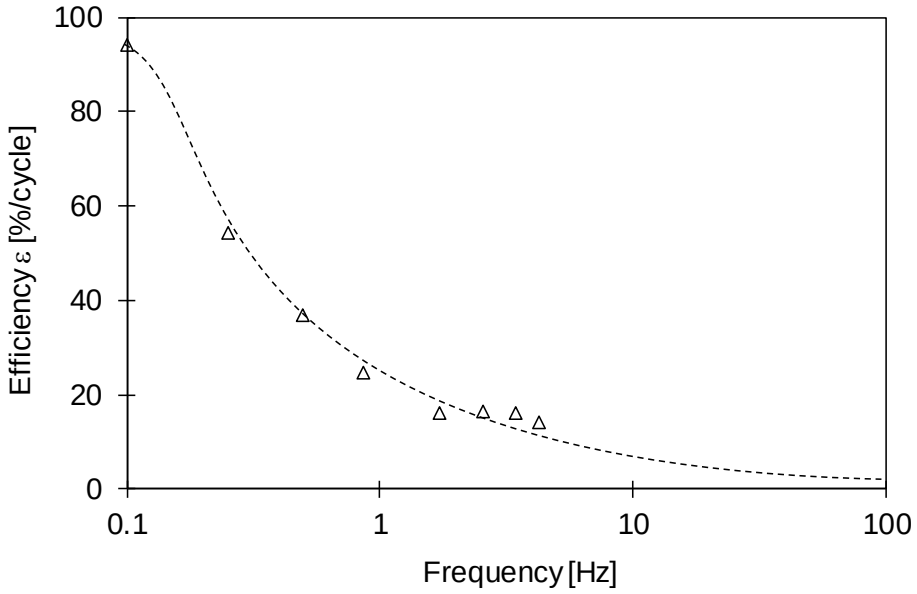

Figure 5.7. Frequency dependent water loss efficiency per cycle with tested frequency range. Test conditions: ΔP = 3kPa. Frequency f = 0.1 Hz ~ 4.5 Hz.

CHAPTER 6. CONCLUSIONS

The long-term performance of geotechnical systems depends on the soil response to repetitive loads in transportation, wind turbines, rainfall, diffusive flow, condensation, solar radiation, winds and diagenesis mechanisms. This thesis focuses on the impact from repetitive geo-environmental loadings and contains the study of suction cycles, pore fluid chemistry cycles, wet-dry induced precipitation cycles, and atmospheric pressure cycles. Repetitive loads induce the accumulation of irreversible permanent strain and result in associated changes in engineering properties (n, k, V_s, C_c, and ϕ).

6.1 Conclusions

The purpose of this research is to enhance the fundamental understanding of the long-term response of soils subjected to repetitive geo-environmental loads and to address the engineering implications. The section below summarizes the main conclusions from this study.

Fine-grained Soil Response to Wet-Dry Cycles under k_0 conditions

- The void ratio evolves towards the terminal void ratio e_T as the number of load cycles increases. The changes in void ratio and small strain stiffness during repetitive loading reveal that repetitive k_0-loading results in denser, stiffer, and less attenuating kaolinite fabrics.

- Evolution in electrical conductivity response captures the hysteresis soil water characteristics and converging fabric evolution. Changes in soil water

characteristics indicate the kaolinite fabric evolve towards an equilibrium condition under sufficient number of wet-dry cycles.

- The soil subjected to wet-dry cycles reaches volumetric terminal state where contraction and expansion is equally balanced (i.e., constant volume). Shakedown prevails with the small stress amplitude and low stress levels.

Wet-Dry Cycles Induced Mineral Precipitation

- Droplet precipitation curls on hydrophobic surfaces but spreads out on hydrophilic surfaces during evaporation. NaCl precipitation and re-precipitation experiments in microfluidic chip can capture insight of potential salt precipitation phenomena in geomaterials.

- Deformation in PDMS microfluidic chip originates from both the capillary forces (air invasion forms "desiccation crack") and crystal forces (crystallization pressure distorts the individual pores and induces swelling).

- Crystal growth in hydrophilic chip favors at air-liquid interface, but nucleates inside the matrix due to local supersaturation and forms crossed crystals in hydrophobic chip. Formation of new crystals prefers the initial precipitated sites. Precipitation in fractures develops at the expense of the crystals inside the matrices.

Fine-grained Soil Response to Pore Fluid Chemistry Cycles under k_0 conditions

- Salt concentration levels governs particle level electrical forces and determines the particle-particle association. Converged evolution of kaolinite fabrics result in

macroscopic recoverable volumetric strains under pore chemistry cycles. The void ratio evolves towards the terminal void ratio e_T as the number of load cycles increases.

- Parallel model and iso-strain analysis can capture the chemical-mechanical coupled soil response. Fine-grained soil subjected to pore fluid chemistry cycles reaches volumetric terminal state where the equivalent effective stress (van der Waals attraction and double layer repulsion) balances out.

Accelerated Water Transport under Barometric Pumping Pressure Cycles

- NMR is an advanced technique which measures soil water content and captures variation in depth with saturation profile analysis.

- Atmospheric pressure cycles accelerate water transport in unsaturated soil inside the closed system. Mathematical model can capture both the evaporative diffusion and the accelerated water mass loss induced by pressure cycles.

- Frequency dependent efficiency determines the effect of water loss acceleration in unsaturated sand specimen. It is in reverse proportion to rise of pressure cycle frequencies.

6.2 Recommendations for Future Work

This thesis contains studies that relate to soil response subjected to repetitive geo-environmental loads. The suggestions below describe the important sections that require further exploration and investigation.

- The equivalent stress concept may not properly capture effective stress that soil experienced under cyclic loading. Numerical simulations can help to enhance the understanding of soil behavior under repetitive loading condition.

- The indirect interpretation of soil fabric evolution under repetitive loads requires the implementation of sophisticated experimental method. Imaging analysis and advanced computer tools can address the missing puzzle.

- The development of mathematical model that can incorporate the repetitive load-deformation behavior caused by cyclic changes in both mechanical loads and non-mechanical loads (geo-environmental loads) is critical.

- Digital signal processing is a computer-aided tool that can identify and delineate the boundaries of soil features based on difference in form and color. Imaging results can apply such technique in order to obtain soil properties in mineralogical composition, pore size, and spatial distribution.

- Quantitative analysis on phenomena concentrated experimental studies help to improve understanding in cyclic soil behavior. Dimensionless number technique allows to address the study in depth conceptually.

References

Abrol, I. P., Yadav, J. S. P., and Massoud, F. I. (1988). "Salt-affected soils and their management." *FAO Soils Bulletin*, 39, 93 pp.

Al Mukhtar, M., Robinet, J. C., Liu, C. W., and Plas, F. (1993). "Hydromechanical behaviour of partially saturated low porosity clays." *International Conference on Engineering Fills*, 87-98.

Albrecht, B. A. and Benson, C. H. (2001). "Effect of desiccation on compacted natural clays." *Journal of Geotechnical and Geoenvironmental Engineering*, 127(1), 67-75.

Al-Homoud, A. S., Basma, A. A., Husein Malkavi and Al-Bashabshah, M. A. (1995). "Cyclic swelling behaviour of clays." *Journal of Geotechnical Engineering*, 121, 582-565.

Allam, M. and Sridharan, A. (1981). "Effect of wetting and drying on shear strength." *Journal of Geotechnical Engineering Division*, 107, 421-438.

Alonso, E. E., and Olivella, S. (2008). "Modelling Tunnel Performance in Expansive Gypsum Claystone." *12th International Conference on Computer Methods and Advances in Geomechanics*, 2.

Alonso, E. E., Lloret, A., Gens, A., and Yang, D. Q. (1995). "Experimental behaviour of highly expansive double-structure clay." *In Proceedings of 1st International Conference on Unsaturated Soils*, 1, 11-16.

Alonso, E. E., Romero, E., Hoffmann, C., and García-Escudero, E. (2005). "Expansive bentonite-sand mixtures in cyclic controlled-suction drying and wetting." *Engineering Geology*, 81(3), 213-226.

Alonso-Marroquin, F., and Herrmann, H. J. (2004). "Ratcheting of granular materials." *Physical Review Letters*, 92(5), 054301.

Anandarajah, A. (1997). "Structure of sediments of kaolinite." *Engineering Geology*, 47, 313-323.

Andersen, K. H. (2009). "Bearing capacity under cyclic loading-offshore, along the coast, and on land." *Canadian Geotechnical Journal*, 46(5), 513-535.

Andre, L., Audigane, P., Azaroual, M., and Menjoz, A. (2007). "Numerical modeling of fluid–rock chemical interactions at the supercritical CO2-liquid interface during CO2 injection into a carbonate reservoir, the Dogger aquifer (Paris Basin, France)." *Energy Convers. Manag.*, 48, 1782-1797.

Aquilano, D., Pastero, L., Bruno, M., and Rubbo, M. (2009). "{100} and {111} forms of the NaCl crystals coexisting in growth from pure aqueous solution." *Journal of Crystal Growth*, 311(2), 399-403.

Auer, L. H., Rosenberg, N. D., Birdsell, K. H. and Whitny, E. M. (1996). "The Effects of Barometric Pumping on Contaminant Transport." *J. Cont. Hydrol.*, 24, 145-166.

Baehr, A. L., and Hult, M. F. (1991). "Evaluation of unsaturated zone air permeability through pneumatic tests." *Water Resour. Res.*, 27(10), 2605-2617.

Baehr, A. L., Hoag, G. E., and Marley, M. C. (1989). "Removing volatile contaminants from the unsaturated zone by inducing advective air-phase transport." *J. Contam. Hydrol.*, 4, 1-26.

Barbour, S. L., and Fredlund, D. G. (1989). "Mechanisms of osmotic flow and volume change in clay soils." *Can. Geotech. J.*, 26(4), 551-562.

Barbour, S.L. (1998). “Nineteenth Canadian Geotechnical Colloquium: The soil-water characteristic curve: a historical perspective.” *Canadian Geotechnical Journal*, 35, 873-894.

Basma, A.A., Al-Homoud, A.S., Malkavi, A.I.H., and Al- Bashabshah, M.A. (1996). “Swelling-shrinkage behaviour of natural expansive clays.” *Applied Clay Science*, 11, 211-227.

Benavente, D., and Martinez-Martinez, J., Mendoza, N. C., and del-Cura, M. A. G. (2007). “Salt weathering in dual-porosity building dolostones.” *Engineering Geology*, 94, 215-226.

Berejnov, V., Djilali, N., and Sinton, D. (2008). “Lab-on-chip methodologies for the study of transport in porous media: Energy applications.” *Lab on a Chip*, 8, 689-93.

Bernier, F., Volckaert, G., Alonso, E. E., and Villar, M. (1997). “Suction-controlled experiments on Boom clay.” *Engineering Geology*, 47(4), 325-338.

Bishop, A. W. (1959). ‘‘The principle of effective stress.’’ *Teknisk Ukeblad I Samarbeide Med Teknikk*, 106(39), 859-863.

Bolt, G. H. (1956). “Physico-chemical analysis of the compressibility of pure clays.” *Geotechnique*, 6(2), 86-93.

Bolt, G. H., and Miller, R. D. (1955). “Compression studies of illite suspensions.” *Proc. Am. Soc. Soil Sci.*, 19, 285-288.

Borsic, A., Comina, C., Lancellotta, R., Foti, S., and Musso, G. (2005). “Imaging Heterogeneities in Sand Samples with ERT: Laboratory Results.” *Geotechnique*, 50(7), 539-547.

Brand, E. W. (1984). “Landslides in Southeast Asia: a state-of-the-art report.” *Proceedings of the Fourth International Symposium on Landslides*, Toronto, 1, 17-59 (Addendum, 3, 105-6).

Brignoli, E. G. M., Gotti, M., and Stokoe, K. H. (1996). “Measurements of Shear Waves in Laboratory Specimens by Means of Piezoelectric Transducers.” *Geotech. Test. J.*, 19, 384-397.

Brooks, R.H., and Corey, A.T. (1966). “Properties of porous media affecting fluid flow.” *Journal of the Irrigation and Drainage Division*, 92(2), 61-88.

Buckingham, E. (1904). “Contributions to our knowledge of the aeration of soils.” *Bull. 25, Soils Bur.*, U.S. Dep. of Agric.

Buil, M. (1983). “Thermodynamic and experimental study of the crystallization pressure of water-soluble salts.” *Materials Science and Restoration*.

Bulut, R., Lytton, R. L., Wray, W. K. (2001). “Suction measurements by filter paper.” ASCE Geotechnical Publication, 243-261.

Cahill, A. T., and Parlange, M. B. (1998). “On water vapor transport in field soils.” *Water Resour. Res.*, 34, 731-739.

Campbell, G.S., Smith, D.M., and Teare, B.L. (2007). “Application of a dew point method to obtain the soil water characteristic.” *Experimental Unsaturated Soil Mechanics*, 71-77.

Cardell, C., Delalieux, F., Roumpopoulos, K., Moropoulou, A., Auger, F., and Van Grieken, R. (2003). “Salt-induced decay in calcareous stone monuments and buildings in a marine environment in SW France.” *Construction Building Materials*, 17, 165-179.

Cardiano, P., Ponterio, R. C., Sergi, S., Lo Schiavo, S., and Piraino, P. (2005). “Epoxy-silica polymers as stone conservation materials.” Polymer, 46(6), 1857-1864.

Cass, A., Campbell, G.S., and Jones, T.L. (1984). "Enhancement of thermal water vapor diffusion in soil." *Soil Sci. Soc. Am. J.*, 48, 25-32.

Cha, M., Santamarina, J. C., Kim, H. S. and Cho, G. C. (2014). "Small-strain stiffness, shear-wave velocity, and soil compressibility." *Journal of Geotechnical and Geoenvironmental Engineering*, 140(10), p.06014011.

Chamberlain, E. J., Iskandar, I. and Hunsicker, S. E. (1990). "Effect of freeze-thaw cycles on the permeability and macrostructure of soils." *Cold Region Research and Engineering Laboratory*, 90(1), 145-155.

Chapman, D. L. (1913). "A contribution to the theory of electro- capillarity." *Philosophical Magazine*, 25(6), 475-481.

Chatterji, S., and Jensen, A. D. (1989). "Efflorescence and breakdown of building materials." *Nordic Concrete Research*, 8, 56-61.

Chatterji, S., and Thaulow, N. (1997). *Cem. Concr. Res.*, 27, 811.

Chattopadhyay, P. K. (1972). "Residual shear strength of some pure clay minerals." PhD thesis, *University of Alberta*, Edmonton.

Chauvet, F., Duru, P., Geoffroy, S., and Prat, M. (2009). "Three periods of drying of a single square capillary tube." *Phys. Rev. Lett.*, 103, 124502.

Chen, F.H. (1965). "The use of piers to prevent uplifting of lightly loaded structures founded on expansive soils." *Proceedings of International Engineering Conference on Expansive Clay Soils*.

Chen, F.H., and Ma, G.S. (1987). "Swelling and shrinkage behavior of expansive clays." *6th International Conference on Expansive Soils*, 1, 127-129.

Chen, J. and Anandarajah, A. (1998) "Influence of pore fluid composition on volume of sediments in kaolinite suspensions." *Clays and Clay Minerals*, 46, 145-152.

Choi, J. W. and Smith, J. A. (2005). "Geoenvironmental Factors Affecting Organic Vapor Advection and Diffusion Fluxes from the Unsaturated Zone to the Atmosphere under Natural Conditions." *Environmental Engineering Science*, 22 (1), 95-108.

Chong, S. H. and Santamarina, J. C. (2016). "Sands subjected to vertical repetitive loading under zero lateral strain: Accumulation models, terminal densities, and settlement." *Canadian Geotechnical Journal*, 53(22), 2039-2046.

Chu, T.Y., and Mou, C.H. (1973). "Volume change characteristics of expansive soils determined by controlled suction tests." *Proceedings of 3rd International Conference on Expansive Soils*, 2, 177-185.

Claria, J. J., Goldsztein, G. H., and Santamarina, J. C. (2012). "AC Diffusion: Transport in Porous Networks Subjected to Zero-Time-Average Advective Flow." *Transport in Porous Media*, 93(1), 51-61.

Clements W. E. and M.H. Wilkening, M. H. (1974). "Atmospheric pressure effects on ^{222}Rn transport across the earth-air interface." *J. Geophys. Res.*, 79, 5025-5029.

Coghill III, C. H., Haywood, J. L., Chatburn, R. L., and Carlo, W. A. (1991). "Neonatal and pediatric high-frequency ventilation principles and practice." *Respir. Care*, 36, 596-609.

Collins, I. F., Wang, A. P. and Saunders, L. R. (1993). "Shakedown theory and the design of unbound pavements." *Road and Transport Research*, 2(4), 28-39.

Comina, C., Foti, S., Lancellotta, R., Musso, G., and Borsic, A. (2005). "Imaging Heterogeneities and Diffusion in Sand Samples." *Proceedings of the 11th*

International Conference of the International Association of Computer Methods and Advances in Geomechanics, 2, 27-34.
Cook, R. U., and Smalley, I. J. (1968). "Salt weathering in deserts." *Nature*, 220, 1226-1227.
Correns, C.W., and Steinborn, W. (1939). "Experimente zur Messung und Erklarung der sogenannten Kristallisationskraft." *Zeitschrift fur Kristallographie*, 101(Heft 1/2), 117-133.
Coussot, P. (2000). "Scaling approach of the convective drying of a porous medium." *Eur. Phys. J. B*, 15, 557-566.
Coussot, P. (2000). "Scaling approach of the convective drying of a porous medium." *The European Physical Journal B - Condensed Matter and Complex Systems*, 15, 557-566.
Covey, W. G. (1965). "Studies on the Drying of Bare Ground." Thesis, *Agr. Mech. Coll*.
Cui, Y. J. and Delage, P. (1996). "Yielding and behaviour of an unsaturated compacted silt." *Geotechnique*, 46(2), 291-311.
D'Appolonia, D. J., and D'Appolonia, E. E. (1967). "Determination of the maximum density of cohesionless soils." *Proceedings of 3rd Asian Regional Conference on Soil Mechanical Foundation Engineering*, 1, 266-268.
Dai, S., Wuttke, F., and Santamarina, J. C. (2013). "Coda wave analysis to monitor processes in soils." *Journal of Geotechnical and Geoenvironmental Engineering*, 139(9), 1504-1511.
Damasceno, V. M., and Fratta, D. (2006). "Chemical Diffusion Detection in a Porous Media Using Electrical Resistance Tomography." *ASCE Geotechnical Special Publication (GSP) 149: Site and Geomaterial Characterization 2006 GeoShanghai International Conference*, 174-181.
Day, R. W. (1994). "Swell-shrink behavior of compacted clay." *Journal of Geotechnical Engineering*, 120(3), 618-623.
De Vries, D.A. (1958). "Simultaneous transfer of heat and moisture in porous media." *Trans. Am. Geophys*. Union, 39, 909-916.
De Yoreo, J. J., and Vekilov, P. (2003). "Principles of crystal nucleation and growth." *Mineral. Soc. Am.*, 54, 57-93.
Deegan, R. D., Bakajin, O., Dupont, T. F., Huber, G., Nagel, S. R., and Witten, T. A. (1997). "Capillary flow as the cause of ring stains from dried liquid drops." *Nature*, 389(6653), 827-829.
Deegan, R. D., Bakajin, O., Dupont, T. F., Huber, G., Nagel, S. R., and Witten, T. A. (2000). "Contact line deposits in an evaporating drop." *Phys. Rev. E*, 62, 756-762.
Delage, P. and Lefebvre, G. (1984). "Study of the structure of a sensitive Champlain clay and of its evolution during consolidation." *Canadian Geotechnical Journal*, 21, 21-35.
Delage, P., and Romero, E. (2008). "Geoenvironmental testing." *Geotech Geol Eng*, 26, 729-749.
Delage, P., Suraj Da Silva, G.P.R., and De Laure, E. (1992). "Suction controlled testing of non- saturated soils with an osmotic consolidometer." *Proceedings of the 7th International Conference on Expansive Soils*, 206-211.
Desarnaud, J., and Shahidzadeh-Bonn, N. (2011). "Salt crystal purification by deliquescence/crystallization cycling." *Europhys. Lett.*, 95, 48002.

Di Donna, A., and Laloui, L. (2015). “Response of soil subjected to thermal cyclic loading: Experimental and constitutive study.” *Engineering Geology*, 190, 65-76.
Di Maio, C. (1996). “Exposure of bentonite to salt solution: osmotic and mechanical effects.” *Geotechnique*, 46(4), 695-707.
Di Maio, C., Santoli, L., and Schiavone, P. (2004). “Volume change behaviour of clays: the influence of mineral composition, pore fluid composition and stress state.” *Mech Mater*, 36, 435-451.
Dif, A. E. and Bluemel, W. F. (1991). "Expansive soils under cyclic drying and wetting," *Geotechnical Testing Journal*, 14(1), 96-102.
DOE. (2000). “Innovative Technology Summary Report, Barometrically Enhanced Remediation Technology.” *Department of Energy*.
Doherty, R. D., Hughes, D. A., Humphreys, F. J., Jonas, J. J., Jensen, D. J., Kassner, M. E., King, W. E., McNelley, T. R., McQueen, H. J., and Rollett, A. D. (1997). *Materials Science and Engineering*, 238, 219-274.
Escario, V. (1980). “Suction controlled penetration and shear tests.” *Proceedings of 4th International Conference on Expansive Soils*, 2, 781-797.
Escario, V. and Saez, J. (1986). “The shear strength of partly saturated soils.” *Geotechnique*, 36(3), 453-456.
Evans, I. S. (1969). “Revue de Geomorphologie.” *Dynamique*, 19(4), 153.
Everett, D. H. (1961). “The thermodynamics of frost damage to porous solids.” *Trans. Faraday Soc.*, 57, 1541-1551.
Fam, M. and Dusseault, M. (1998). “Evaluation of surface related phenomena using sedimentation tests.” *Geotechnical Testing Journal*, 21, 180-184.
Fisher, R. A. (1923). “Some factors affecting the evaporation of water from soil.” *J. Agron. Sci.*, 13(2), 121-143.
Flatt, R. J. (2002). “Salt damage in porous materials: how high supersaturations are generated.” *J. Cryst. Growth*, 242, 435-454.
Fourie, A. B. (1996). “Predicting rainfall-induced slop instability.” *Proceedings of the Institution of Civil Engineers: Geotechnical Engineering*, 119(4), 211-218.
Fredlund, D. G., Gan, JK-M, and Gallen, P. (1995). “Suction measurements on compacted till specimens and indirect filter paper calibration technique.” *Transp Res Board Transp Res Rec*, 1481, 3-9.
Fredlund, D.G. (1998). “Bringing unsaturated soil mechanics into engineering practice.” *In Proceedings of the 2nd International Conference on Unsaturated Soils*, 2, 1-36.
Fredlund, D.G., Xing, A., and Huang, S. (1994). “Predicting the permeability function for unsaturated soils using the soil-water characteristic curve.” *Canadian Geotechnical Journal*, 31, 533-546.
Fritton, D. D., Kirkham, D., and Shaw, R. H. (1970). “Soil water evaporation, isothermal diffusion, and heat and water transfer.” *Soil Sci. Soc. Am. Proc.*, 34, 183-189.
Fujimaki, H., Shimano, T., Inoue, M., and Nakane, K. (2006). “Effect of a salt crust on evaporation from a bare saline soil.” *Vadose Zone J.*, 5(4), 1246-1256.
Fukuda, H. 1955. “Air and Vapor Movement in Soil Due to Wind Gustiness.” *Soil Sci.*, 79, 249-256.
Fukuoka, M. (1980). “Landslides associated with rainfall.” *Geotechnical Engineering*, 11, 1-29.

Fuller, R. C., Prevost, J. H., and Piri, M. (2006). “Three-phase equilibrium and partitioning calculations for CO2 sequestration in saline aquifers.” *J. Geophys. Res*., 111, B06207.

Gallipoli, D., Wheeler, S. J., and Karstunen, M. (2003). “Modelling the variation of degree of saturation in a deformable unsaturated soil.” *Geotechnique*, 53(1), 105-112.

Gardner, W. R., and Fireman, M. (1958). “Laboratory studies of evaporation from soil columns in the presence of a water table.” *Soil Science*, 85(5), 244-249.

Gauri, K. L., and Bandyopadhyay, J. K. (1999). “Carbonate stone: chemical behavior.” *Durability and conservation*, Wiley.

Ghassemi, F., Jakeman, A.J., and Nix, H.A. (1995). “Salinization of land and water resources. Human causes, extent, management and case studies.” *Sydney: University of New South Wales Press Ltd*.

Giorgis, T., Carpita, M., and Battistelli, A. (2007). “2D modeling of salt precipitation during the injection of dry CO2 in a depleted gas reservoir.” *Energy Convers. Manag.*, 48, 1816-1826.

Goldsztein, G. H., and Santamarina, J. C. (2004). “Solute transport during cyclic flow in saturated porous media.” *Appl. Phys. Lett*., 85, 2432-2434.

Goudie, A., and Viles, H. (1997). “Salt Weathering Hazards.” *Wiley*.

Goudie, A.S. (1997). “Weathering Processes. In Arid zone geomorphology (2nd Edition).” *Wiley*, 25-39.

Greenberg, J. A., Mitchell, J. K., and Witherspoon, P. A. (1973). “Coupled salt and water flows in a groundwater basin.” *J. Geophys. Res*., 78(27), 6341-6353.

Griffiths, F. J. and Ramesh, C. J. (1990). “Discussion: Change in pore size distribution due to consolidation of clays.” *Geotechnique*, 40(2), 303-309.

Hanks, R. J., Gardner, H. R., and Fairbourn, M. L. (1967). “Evaporation of water from soils as influenced by drying with wind or radiation.” *Soil Sci. Soc. Am. Proc*., 31, 593-598.

Harries, J. R., and Ritchie, A. I. M. (1985). “Pore gas composition in waste rock dumps undergoing pyritic oxidation.” *Soil Science*, 140, 143-152.

Harrison, D. J., Fluri, K., Seiler, K., Fan, Z., Effenhauser, C. S., and Manz, A. (1993). “Micromachining a miniaturized capillary electrophoresis-based chemical analysis system on a chip.” *Science*, 261, 895-897.

Haug M. D., Barbour, S. L., LOngval, P. (1988) “Design and construction of a pre-hydrated sand-bentonite liner to contain brine.” *Can. J. Civ. Eng*., 15, 955-963.

Heitman, J. L., Xiao, X., Horton, R., and Sauer, T. J. (2008). “Sensible heat measurements indicating depth and magnitude of subsurface soil water evaporation.” *Water Resour. Res*., 44.

Hillel, D. (1998). “Environmental Soil Physics: Fundamentals, Applications, and Environmental Considerations.” *Academic Press*, Waltham.

Huang, A. W. (2016). “The seventh James. K. Mitchell lecture: Characterization of silty/sand soils.” *Australian Geomechanics Journal*, 51(4), 1-23.

Hueckel, T. A. (1992). "On the Effective Stress Concepts and Deformation in Clays Subjected to Environmental Loads: Discussion." *Canadian Geotechnical Journal*, 29, 1120-1125.

Idso, S. B., Reginato, R. J., and Jackson, R. D. (1979). “Calculation of evaporation during three stages of soil drying.” *Water Resour. Res*., 15, 487-488.

Jackson, R. D. (1973). "Diurnal changes in soil water content during drying, in Field Soil Water Regime." *Soil Sci. Soc. Am.*, 37-55.

Jackson, R. D., Kimball, B. A., Reginato, R. J., and Nakayama, F. S. (1973). "Diurnal soil-water evaporation: Time-depth-flux patterns." *Soil Sci. Soc. Am. Proc.*, 37, 505-509.

Joshi, C. H., Kamm, R. D., Drazen, J. M., and Slutsky, A. S. (1983). "An experimental study of gas exchange in laminar oscillatory flow." *J. Fluid Mech.*, 133, 245-254.

Jovicic, V., Coop, M. R., and Simic, M. (1996). "Objective Criteria for Determining Gmax from Bender Elements Tests." *Geotechnique*, 46, 357-362.

Kaczmarek, M., and Hueckel, T. (1998). "Chemo-mechanical consolidation of clays: analytical solutions for a linearized one-dimensional problem." *Transport in Porous Media*, 32, 49-74.

Kassiff, G. and Ben Shalom, A. (1971). "Experimental Relationship Between Swell Pressure and Suction." *Geotechnique*, 21(3), 245-255.

Keijzer, Th. J. S., Kleingeld, P. J., and Loch, J. P. G. (1997). "Chemical Osmosis in Compacted Clayey Material and the Prediction of Water Transport." *Geoenvironmental Engineering Contaminated Ground: Fate of Pollutants and Remediation*, 199-204.

Kemper, W. D. and Rollins, J. B. (1966). "Osmotic Efficiency Coefficients across Compacted Clays." *Soil Science Society of America Proceedings*, 30, 529-534.

Kenney, T. C. (1967). "The influence of mineralogical composition on the residual strength of natural soils." *Proceedings of the geotechnical conference on the shear strength properties of natural soils and rocks*, 1, 123-129.

Khandurina, J., Mcknight, T. E., Jacobson, S. C., Waters, L. C., Foote, R. S., and Ramsey, J. M. (2000). "Integrated system for rapid PCR-based DNA analysis in microfluidic devices." *Anal. Chem.*, 72, 2995-3000.

Kim, K. Y., Han, W. S., Oh, J., Kim, T., and Kim, J. C. (2012). "Characteristics of salt-precipitation and the associated pressure build-up during CO2 storage in saline aquifers." *Transp. Porous Media*, 92, 397-418.

Kimball, B. A., and Lemon, E. R. (1971). "Air turbulence effects upon soil gas exchange." *Soil Sci. Soc. Am. J.*, 35, 16-21.

Kopp, M. U., de Mello, A. J., and Manz, A. (1998). "Chemical amplification: continuous-flow PCR on a chip." *Science*, 280, 1046-1048.

Kurzweg, U. H. (1985). "Enhanced heat conduction in fluids subjected to sinusoidal oscillations." *J. Heat Transfer*, 107, 459-462.

Kurzweg, U. H. (1985). "Enhanced heat conduction in oscillating viscous flows within parallel plate channels." *J. Fluid Mech.*, 156, 291-300.

Lapierre, C., Leroueil, S., and Locat, J. (1990). "Mercury intrusion and permeability of Louiseville clay." *Canadian Geotechnical Journal*, 27, 761-773.

Lee, J. S., and Santamarina, J. C. (2005). "Bender elements: performance and signal interpretation." *Journal of Geotechnical and Geoenvironmental Engineering*, 131(9), 1063-1070.

Lehmann, P., and Or, D. (2009). "Evaporation and capillary coupling across vertical textural contrasts in porous media." *Physical Review E*, 80, 046318.

Lehmann, P., Assouline, S., and Or, D. (2008). "Characteristic lengths affecting evaporative drying of porous media." *Phys. Rev. E*, 77(5), 056309.

Lenormand, R. (1990). *J. Phys.: Condens. Matter*, 2, 79-88.
Lenormand, R., Touboul, E., and Zarcone, C. (1988). *J. Fluid Mech*., 189, 165-87.
Leong, E. C. and Rahardjo, H. (1997). "Review of soil-water characteristic curve equations." *Journal of Geotechnical and Geoenvironmental Engineering*, 123(12), 1106-1117.
Lewin, S. (1982). "Conservation of historic buildings and monuments." *National Academy Press*, p120.
Lim, T. T., Rahardjo, H., Chang, M. F. and Fredlund, D. G. (1996). "Effect of rainfall on matric suctions in a residual soil slope." *Canadian Geotechnical Journal*, 33(3), 618-628.
Lin, L. C., and Benson, C. H. (2000). "Effect of wet-dry cycling on swelling and hydraulic conductivity of GCLs". *Journal of Geotechnical and Geoenvironmental Engineering*, 126(1), 40-49.
Linnow, K. (2013). "In situ Raman observation of the crystallization in $NaNO_3$–Na_2SO_4–H_2O solution droplets." *Environ Earth Sci*., 69, 1609-1620.
Lloret, A. and Alonso, E. E. (1980). "Consolidation of unsaturated soil including swelling and collapse behaviour." *Geotechnique*, 30(4), 449-477.
Long, J. H., and Vanneste, G. (1994). "Effects of cyclic lateral loads on piles in sand." *Journal of Geotechnical Engineering*, 120(1), 225-244.
Lu, Q., Wen, J., and Zhang, H. (2007). "Effect of chronic heat exposure on fat deposition and meat quality in two genetic types of chicken." *Poult. Sci*., 86, 1059-1064.
Lumb, P. (1962). "The properties of decomposed granite." *Geotechnique*, 12(3), 226-243.
Massmann, J. and Farrier, D. F. (1992). "Effects of Atmospheric Pressures on Gas Transport in the Vadose Zone." *Water Resour. Res*., 28 (3), 777-791.
Mata, C., Romero, E., Ledesma, A. (2002). "Hydro-chemical effects on water retention in bentonite-sand mixtures." *Proceedings of Third International Conference on Unsaturated Soils*, 283-288.
Mazutis, L., Gilbert, J., Ung, W. L., Weitz, D. A., Griffiths, A. D., and Heyman, J. A. (2013). "Single-cell analysis and sorting using droplet-based microfluidics." *Nature protocols*, 8(5), 870-891.
Melton, I. E., and Rand, B. (1977). "Particle Interactions in Aqueous Kaolinite Suspensions III. Sedimentation Volume." *Journal of Colloid and Interface Science*, 60(2), 331-336.
Mesri, G., and Olsen, R. E. (1971). "Consolidation characteristics of montmorillonite." *Geotechnique*, 21(4), 341-352.
Mesri, G., and Olson, R. E. (1970). "Shear strength of montmorillonite." *Geotechnique*, 20(3), 261-270.
Milly, P. C. D. (1984a). "A linear analysis of thermal effects on evaporation from soil." *Water Resour. Res*., 20, 1075-1085.
Milly, P. C. D. (1984b). "A simulation analysis of thermal effects on evaporation from soil." *Water Resour. Res*., 20, 1087-1098.
Mitchell, J. K. (1991). "Conduction Phenomena: from the theory to geotechnical practice." *Geotechnique*, 41(3), 299-340.
Mitchell, J. K. (1993). "Fundamentals of soil behavior, 2nd Ed." *Wiley*, New York.
Mitchell, J. K., and Soga, K. (2005). "Fundamentals of soil behaviour, 3rd edn." *Wiley*.

Mitchell, J. K., Greenberg, J. A., and Witherspoon, P. A. (1973). "Chemico-osmotic effects in fine-grained soils." *J. Soil Mech. Fdn Div. Am. Soc. Civ. Engrs*., 99(4), 307-322.
Mohr, D. H. and Merz, P. H. (1995). "Application of a 2D Air Flow Model to Soil Vapor Extraction and Bioventing Case Studies." *Groundwater*, 33, 433-444.
Mokni, N., Olivella, S., and Alonso, E. E. (2010). "Swelling in clayey soils induced by the presence of salt crystals." *Applied Clay Science*, 47, 105-112.
Moore, R. (1991). "The chemical and mineralogical controls upon the residual strength of pure and natural clays." *Geotechnique*, 41(1), 35-47.
Mualem, Y. (1976). "A new model for predicting the hydraulic conductivity of unsaturated porous media." *Water Resources Research*, 12(3), 513-522.
Muller, N., Qi, R., Mackie, E., Pruess, K., and Blunt, M.J. (2009). "CO_2 injection impairment due to halite precipitation." *Energy Procedia*, 1, 3507-3514.
Mullin, J. W. (2001). "Crystallization, 4th edition." *Butterworths-Heinemann*.
Musso, G., Morales, E. R., Gens, A., and Castellanos, E. (2003). "The role of structure in the chemically induced deformations of FEBEX bentonite." *Applied Clay Science*, 23(1), 229-237.
Musso, G., Romero, M. E., Gens, A., and Castellanos, E. (2003). "The role of structure in the chemically induced deformations of FEBEX bentonite." *Applied Clay Science*, 23, 229–237.
Nachshon, U., Weisbrod, N., Dragila, M. I., and Grader, A. (2011). "Combined evaporation and salt precipitation in homogeneous and heterogeneous porous media." *Water Resources Research*, 47.
Naillon, A., Duru, P., Marcoux, M., and Prat, M. (2015). "Evaporation with sodium chloride crystallization in a capillary tube." *J. Cryst. Growth*, 422, 52-61.
Nakata, Y., Kajiwara, T., and Yoshimoto, N. (2013). "Collapse behavior of slope due to change in pore water pressure." *Proc., 18th Int. Conf. Soil Mechanics and Geotechnical Engineering*, Paris, 2225-2228.
Narsilio, A. and Santamarina, J. C. (2008). "Terminal densities." *Geotechnique*, 58(8), 669-674.
Nassar, I. N., and Horton, R. (1999). "Salinity and compaction effects on soil water evaporation and water and solute distributions." *Soil Sci. Soc. Am. J.*, 63(3), 752-758.
Neeper, D.A. 2002. "Investigation of the vadose zone Using Barometric Pressure Cycles." *J. Cont. Hydrol*., 54, 59-80.
Netterberg, F., and Loudon, P. A. (1980). "Simulation of salt damage to roads with laboratory experiments." *In Proceedings of 7th Regional Conference for Africa on Soil Mechanics and Foundation Engineering*, 355-361.
Ng, C. W. W. and Pang, Y. W. (2000). "Influence of stress state on soil- water characteristics and slope stability." *Journal of Geotechnical and Geoenvironmental Engineering*, 126(2), 157-166.
Ng, C. W. W. and Shi, Q. (1998). "A numerical investigation of the stability of unsaturated soil slopes subjected to transient seepage." *Computers and Geotechnics*, 22(1), 1-28.
Nilson, R. H., Peterson, E. W., Lie, K. H., Burkhard, N. R., and Hearst, J. R. (1991). "Atmospheric pumping: a mechanism causing vertical transport of contaminated gases through fractured permeable media." *J. Geophys. Res*., 96, 21933-21948.

Norbert, R. (2012). "Electrospray crystallization for nanosized pharmaceuticals with improved properties." *Cryst. Growth Des.*, 12, 3514-3520.

Nowamooz, H., and Masrouri, F. (2008). "Hydromechanical behaviour of an expansive bentonite/silt mixture in cyclic suction-controlled drying and wetting tests." *Engineering Geology*, 101(3-4), 154-164.

O'Brien, N. R. (1971). "Fabric of Kaolinite and Illite Floccules." *Clays and Clay Minerals*, 19, 353-359.

Obika, B., Freer-Hewish, R. J., and Fookes, P. G. (1989). "Soluble salt damage to thin bituminous road and runway surfaces." *Quarterly Journal of Engineering Geology*, 22, 59-73.

Olsen, H. W., Yearsley, E. N., and Nelson, K. R. (1990). "Chemico-Osmosis versus Diffusion-Osmosis." *Transportation Research Record*, 1288, 15-22.

Or, D., Lehmann, P., Shahraeeni, E., and Skokri, N. (2013). "Advances in soil evaporation physics—a review." *Vadose Zone J.*, 12(4).

Orense, R., Farooq, K. and Towhata, I. (2004). "Deformation behavior of sandy slopes during rainwater infiltration." *Soils and Foundation*, 44(2), 15-30.

Osipov, V.I., Nguen, N.B., and Rumjantseva, N.A. (1987). "Cyclic swelling of clays." *Applied Clay Science*, 2, 363-374.

Oteo-Mazo, C., Saez-Aunon, J., and Esteban, F. (1995). "Laboratory tests and equipment with suction control." *Proceedings of the 1st International Conference on Unsaturated soils*, 3, 1509-1515.

Ott, H., Berg, S., and Oedai, S. (2011). "Displacement and mass transfer of CO_2/brine in sandstone." *Society of Core Analysis Conference Paper*, SCA2011-05.

Ott, H., de Kloe, K., Marcelis, F., and Makurat, A. (2011). "Injection of supercritical CO_2 in brine saturated sandstone: pattern formation during salt precipitation." *Energy Procedia*, 4, 4425-4432.

Ott, H., Snippe, J., de Kloe, K., Husain, H., and Abri, A. (2013). "Salt precipitation due to SC-gas injection: single versus multi-porosity rocks." *Energy Procedia*, 37, 3319-3330.

Oxtoby, D. W. (1998). "Nucleation of first-order phase transitions." *Acc. Chem. Res.*, 31, 91-97.

Palomino, A. M. and Santamarina, J. C. (2005). "Fabric map for kaolinite: Effects of pH and ionic concentration on behavior." *Clays and Clay Minerals*, 53, 209-222.

Parlange M. B., Cahill, A. T., Nielsen, D. R., Hopmans, J. W., and Wendroth, O. (1998). "Review of heat and water movement in field soils." *Soil Tillage Res.*, 47, 5-10.

Pasten, C., and Santamarina, J. C. (2014). "Thermally induced long-term displacement of thermoactive piles." *Journal of Geotechnical and Geoenvironmental Engineering*, 140(5), p.06014003.

Paute, J. L., Hornych, P., and Beraben, J. P. (1993). "Repeated load triaxial testing of granular materials on the French network of Laboratoires des Ponts et ChausseÂes." *Flexible Roads*, Balkema, 53-64.

Peng, J., Clarke, B. G., and Rouainia, M. (2006). "A device to cyclic lateral loaded model piles." *Geotechnical Testing Journal*, 29(4), 341-347.

Penman, H.L. (1941). "Laboratory experiments on evaporation from fallow soil." *J. Agric. Sci.*, 31, 454-465.

Perera, Y. Y., Zapata, C. E., Houston, W. N., and Houston, S. L. (2005). "Prediction of the soil-water characteristic curve based on grain-size-distribution and index properties." *ASCE Geotechnical Special Publication*, 130, 49-60.

Peters, G. P., and Smith, D. W. (2004). "The influence of advective transport on coupled chemical and mechanical consolidation of clays." *Mech Mater*, 36, 467-486.

Peysson, Y. (2012). "Permeability alteration induced by drying of brines in porous media." *Eur. Phys. J. Appl. Phys*, 60, 24206.

Philip, J.R., and De Vries, D.A. (1957). "Moisture movement in porous materials under temperature gradients." *Trans. Am. Geophys. Union*, 38, 222-232.

Pierre, A. C. and Ma, K. (1999). "DLVO theory and clay aggregate architechtures formed with AlCl3." *Journal of the European Ceramic Society*, 19, 1615-1622.

Pierre, A. C., Ma, K. and Barker, C. (1995). "Structure of kaolinite flocs formed in an aqueous medium." *Journal of Materials Science*, 30, 2176-2181.

Pruess, K., and García, J. (2002). "Multiphase flow dynamics during CO2 injection into saline aquifers." *Environ. Geol*., 42, 282-295.

Qi, J., Ma, W., and Song, C. (2008). "Influence of freeze–thaw on engineering properties of a silty soil." *Cold Regions Science and Technology*, 53(3), 397-404.

Qin, D., Xia, Y. N., and Whitesides, G. M. (2010). "Soft lithography for micro- and nanoscale patterning." *Nat Protoc*, 5(3), 491-502.

Rand, B. and Melton, I. E. (1977). "Particle interactions in aqueous kaolinite suspensions I. Effect of pH and electrolyte upon the mode of particle interaction in homoionic sodium kaolinite suspensions." *Journal of Colloid and Interface Science*, 60, 308-320.

Rao, S. M., and Shivananda, P. (2005). "Role of osmotic suction in swelling of salt-amended clays." *Canadian Geotechnical Journal*, 42(1), 307-315.

Rathfelder, K. M., Lang, J. R., and Abriola, L. M. (2000). "A numerical model MISER for the simulation of coupled physical, chemical and biological processes in soil vapor extraction and bioventing systems." *J. Contam. Hydrol*., 43, 239-270.

Ravisangar, V. (2001). "The role of sediment chemistry instability and resuspension characteristics of cohesive sediments." PhD thesis, *Georgia Institute of Technology*, Atlanta, Georgia, USA, 297 pp.

Rengasamy, P. (2002). "Transient salinity and subsoil constraints to dryland farming in Australian sodic soils." *Australian Journal of Experimental Agriculture*, 42, 351-361.

Ristenpart, W. D., Kim, P. G., Domingues, C., Wan, J., and Stone, H. A. (2007). "Influence of substrate conductivity on circulation reversal in evaporating drops." *Phys. Rev. Lett.*, 99, 234502.

Roels, S. M., Ott, H., and Zitha, P. L. J. (2014). "Micro-CT analysis and numerical simulation of drying effects of CO_2 injection into brine-saturated porous media." *Int. J. Greenhouse Gas Control*, 27, 146-154.

Roesler, S. K. (1979). "Anisotropic shear modulus due to stress anisotropy." *Journal of the Geotechnical Engineering Division*, 105(7), 871-880.

Ross, D. and Locascio, L. E. (2002). "Microfluidic temperature gradient focusing." *Anal. Chem*., 74(11), 2556-2564.

Santamarina, J. C., and Fam, M. (1995). "Changes in dielectric permittivity and shear wave velocity during concentration diffusion." *Can. Geotech. J*., 32, 647-659.

Santamarina, J. C., and Fratta, D. (2005). "Discrete signals and inverse problems: an introduction for engineers and scientists." *John Wiley & Sons*.

Santamarina, J. C., Klein, K. A., and Fam, M. A. (2001). "Soils and waves: Particulate materials behavior, characterization and process monitoring." *Wiley*, Chichester, U.K.

Santamarina, J. C., Klein, K. A., Wang, Y. H., and Prencke, E. (2002). "Specific surface: determination and relevance." *Canadian Geotechnical Journal*, 39, 233-241.

Saravanapavan, T., and Salvucci, G. D. (2000). "Analysis of rate-limiting processes in soil evaporation with implications for soil resistance models." *Adv. Water Resour*., 23, 493-502.

Sayward, J. M. (1984). "Salt Action on Concrete, US Army Corps of Engineers, Special Report 84±25." *Cold Region Research and Engineering Laboratory*, 69 pp.

Scherer, G. W. (2004). "Stress from crystallization of salt." *Cement and Concrete Research*, 34(9), 1613-1624.

Scherer, G. W., Flatt, R., and Wheeler, G. (2001). "Materials science research for the conservation of sculpture and monuments." *MRS Bull*, 26(1), 44-50.

Schery, S. D., Gaeddert, D. H., and Wilkening, M. H. (1982). "Transport of radon from fractured rock." *J. Geophys. Res*., 87, 2969-2976.

Scotter, D. R., and Raats, P. A. C. (1969). "Dispersion of water vapor in soil due to air turbulence." *Soil Sci*., 108, 170-176.

Scotter, D. R., Thurtell, G. W., and Raats, P. A. C. (1967). "Dispersion resulting from sinusoidal gas flow in porous materials." *Soil Sci.*, 104, 306-308.

Shackelford, C. D., Malusis, M. A., Majeski, M. J., and Stern, R. T. (1999). "Electrical conductivity breakthrough curves." *J. Geotech. Geoenviron. Eng*., 125(4), 260-270.

Shahidzadeh-Bonn, N., Rafai, S., Bonn, D., and Wegdam, G. (2008). "Salt crystallization during evaporation: Impact of interfacial properties." *Langmuir*, 24, 8599-8605.

Shan, C. (1995). "Analytical Solutions for Determining Vertical Air Permeability in Unsaturated Soils." *Water Resour. Res*., 31 (9), 2193-2200.

Shan, C., Falta, R. W., and Javandel, I. (1992). "Analytical solutions for steady state gas flow to a soil vapor extraction well." *Water Resour. Res*., 28(4), 1105-1120.

Sharma, D. R., and Prihar, S. S. (1973). "Effect of depth and salinity of groundwater on evaporation and soil salinization." *Indian Journal Agricultural Science*, 43(6), 582-586.

Sharma, P.V. (1997). "Environmental and Engineering Geophysics." *Cambridge University Press*.

Sharp, R. W., and Booker, J. R. (1984). "Shakedown of pavements under moving surface loads." *Journal of Transportation Engineering*, 110(1), 1-14.

Shokri, N. (2014). "Pore-scale dynamics of salt transport and distribution in drying porous media." *Phys. Fluids*, 26, 012-016.

Shokri, N., Lehmann, P., and Or, D. (2010). "Liquid-phase continuity and solute concentration dynamics during evaporation from porous media: Pore-scale processes near vaporization surface." *Physical Review E*, 81(4).

Sivapullaiah, P. V., and Sridharan, A. (1987). "Effect of polluted water on the physico-chemical properties of clayey soils." *Environmental Geotechnics and Problematic Soils and Rocks*, 179-190.

Skipper, N. T. (2001). "Influence of Pore-Liquid Composition on Clay Behaviour: Molecular Dynamics Simulations of Nano-Structure." *Proc. Workshop on Clay Behaviour: Chemo-Mechanical Coupling,* Edts., C. Di Maio, T. Hueckel, and B. Loret, Maratea, Italy. 18p.

Sleep, B. E. and Sykes, J. F. (1989). "Modellng the transport of volatile organics in variably saturated media." *Water Resour. Res.*, 25(1), 81-92.

Slutsky, A. S., Drazen, J. M., Ingram Jr., R. H., Kamm, R. D., Shapiro, A. H., Fredberg, J. J., Loring, S. H., and Lehr, J. (1980). "Effective pulmonary ventilation with small-volume oscillations at high frequency." *Science*, 209, 609-611.

Snieder, R. (2006). "The theory of coda wave interferometry." *Pure and Applied geophysics*, 163(2-3), 455-473.

Sridharan, A. (1991). "Engineering behaviour of fine grained soils." *Indian Geotech. J.*, 21(1), 1-136.

Sridharan, A., and Prakash, K. (1999). "Mechanisms controlling the undrained shear strength behaviour of clays." *Canadian Geotechnical Journal*, 36(6), 1030-1038.

SRNL. (2006). "Enhanced Attenuation: A Reference Guide on Approaches to Increase the Natural Treatment Capacity of a System." *Savannah River National Laboratory*.

Stallman, R. W. (1967). "Flow in the zone of aeration." *Advances in Hydroscience*, 115-195.

Stallman, R. W., and Weeks, E. P. (1969). "The use of atmospherically induced gas-pressure fluctuations for computing hydraulic conductivity of the unsaturated zone." *Geol. Soc. America. Abs. with Programs*, 7-213.

Staverman, A. J. (1951). "Non-Equilibrium Thermodynamics of Membrane Processes." *Transactions of the Faraday Society*, 48(2), 176-185.

Steiger, M. (2005). "Crystal growth in porous materials - I: The crystallization pressure of large crystals." *Journal of Crystal Growth*, 282(3-4), 455-469.

Steiger, M. (2005). "Crystal growth in porous materials - II: Influence of crystal size on the crystallization pressure." *Journal of Crystal Growth*, 282(3-4), 470-481.

Stern, O. (1924). "Zur Theorie der elektrolytischen Doppelschriht." *Zeitschrift fiir Elektrochemie*, 30, 508-516.

Subba Rao, K.S. and Satyadas, G.G. (1987). "Swelling potential with cycles of swelling and partial shrinkage." *6th International Conference on Expansive Soils*, 1, 137-142.

Subra, S. (2006). "Colloids model for atoms." *Nat. Mater.*, 5, 253-254.

Sunagawa, I. "Growth and morphology of crystals." *Forma*, 14, 147-166.

Takhistov, P., and Chang, H. (2002). "Complex stains morphology." *Ind. Eng. Chem. Res.*, 41, 6256–6269.

Terzaghi, K., and Peck, R. B. (1948). "Soil mechanics in engineering practice." *Wiley*.

Teten O. (1930). "Über einige meteorologische Begriffe." *Z. Geophys.*, 6, 297-309.

Thyagaraj, T., and Rao, S. M. (2013). "Osmotic Swelling and Osmotic Consolidation Behaviour of Compacted Expansive Clay." *Geotechnical and Geological Engineering*, 31(2), 435-445.

Topp, G. C., and E. E. Miller. (1966). "Hysteretic Moisture Characteristics and Hydraulic Conductivities for Glass-Bead Media." *Soil Science Society of America*, 30(2), 156-162.

Trantidou, T., Elani, Y., Parsons, E., and Oscar Ces, O. (2017). "Hydrophilic surface modification of PDMS for droplet microfluidics using a simple, quick, and robust method via PVA deposition." *Microsystems and Nanoengineering*, 3, 16091.

Van Genuchten, M. T. (1980). "A closed-from equation for predicting the hydraulic conductivity of unstructured soil." *Soil Science Society of America*, 44, 892–898.

Van Hameren, R. (2006). "Macroscopic hierarchical surface patterning of porphyrin trimers via self-assembly and dewetting." *Science*, 314, 1433-1436.

Van Olphen, H. (1977). "An Introduction to Clay Colloid Chemistry: For Clay Technologists, Geologists, and Soil Scientists." *Wiley*.

Vanapalli, S.K., Fredlund, D.G., and Pufahl, D.E. (1999). "The influence of soil structure and stress history on the soil–water characteristics of a compacted till." *Geotechnique*, 49 (2), 143-159.

Viklander, P. (1998). "Permeability and volume changes in till due to cyclic freeze/thaw." *Canadian Geotechnical Journal*. 35(3), 471-477.

Wang, L., Cowin, S. C., Weinbaum, S., and Fritton, S. P. (2000). "Modeling tracer transport in an osteon under cyclic loading." *Ann. Biomed. Eng*., 28, 1200-1209.

Watson, E. J. (1983). "Diffusion in oscillatory pipe flow." *J. Fluid Mech*., 133, 233-244.

Weeks, E. P. (1979). "Barometric Fluctuations in Wells Tapping Deep Unconfined Aquifers." *Water Resources Research*, 15, 1167-1176.

Weeks. E. P. (1978). "Field determination or vertical permeability to air in the unsaturated zone." *U.S. Geol. Surv. Prof Pap*, 1051, 41 pp.

Werkmeister, S., Dawson, A.R. and Wellner, F. (2005). "Permanent deformation behaviour of granular materials." *Road materials and pavement design*, 6(1), 31-51.

Wheeler, S.J., and Karube, D. (1996). "Constitutive modelling." *In Proceedings of the 1st International Conference on Unsaturated Soils*, 3, 1323–1356.

Wichtmann, T., Rondón, H. A., Niemunis, A., Triantafyllidis, T., and Lizcano, A. (2010). "Prediction of permanent deformations in pavements using a high-cycle accumulation model." *Journal of Geotechnical and Geoenvironmental Engineering*, 136(5), 728-740.

Wiegand, C. L. and Taylor, S. A. (1961). "Evaporation drying of porous media." *Agr. Expt. Sta., Spec. Rept*., 15, 28pp.

Winkler, E. M. (1997). "Stone in architecture, properties, durability, 3rd edition." *Springer*.

Wolle, C.M. and Hachich, W. (1989). "Rain-induced landslides in Southern Brazil." *Proceedings of the 12th International Conference on Soil Mechanics and Foundation Engineering*, Rio de Janeiro.

Wu, M. H., Huang, S. B., and Lee, G. B. (2010). "Microfluidic cell culture systems for drug research." *Lab on a Chip*, 10(8), 939-956.

Yamanaka T., Takeda, A., and Shimada, J. (1998). "Evaporation beneath the soil surface: some observational evidence and numerical experiments." *Hydrol. Process*., 12, 2193-2203.

Yeung, A. T. and Hsu, H. T. (2002). "Semianalytical Simulation of Soil Vapor Extraction." *Practice Perio. of Haz. Toxic and Rad. Waste Mang.*, 6(1), 14-22.

Yong, R. N., and Warkentin, B. P. (1975). "Soil properties and behaviour." *Elsevier*.

Young, T. (1805). "An Essay on the Cohesion of Fluids." *Philosophical Transactions of the Royal Society of London*, 95, 65-87.

Yu, P. and Richart Jr, F. E. (1984). “Stress ratio effects on shear modulus of dry sands.” *Journal of Geotechnical Engineering*, 110(3), 331-345.